UNIVERSITÀ DI PISA

Scuola di Dottorato in Ingegneria "Leonardo da Vinci"

Corso di Dottorato di Ricerca in

APPLIED ELECTROMAGNETISM IN ELECTRICAL AND BIOMEDICAL ENGINEERING, ELECTRONICS, SMART SENSORS, NANO-TECHNOLOGIES

Tesi di Dottorato di Ricerca

CIRCUIT MODELS FOR NEXT GENERATION FUSION DEVICES

Autore:

Marco Bigi

Relatore:

Prof. Alessandra Fanni

Correlatore:

Ing. Vanni Toigo

Anno 2008

A vos, mi corazón

A Clara, Pietro e Dede

LIST OF CONTENTS

CONSTANTS

c	Speed of light in vacuum	$3 \cdot 10^{8}$ m/s
ε_0	Dielectric permeability of vacuum	$8.85 \cdot 10^{-12}$ F/m
μ_0	Magnetic permeability of vacuum	$4\pi \cdot 10^{-7}$ H/m

ACRONYMS

CS1	**C**ore **S**nubber 1
CS1	**C**ore **S**nubber 2
dc	**d**irect **c**urrent
EGPS	**E**xtraction **G**rid **P**ower **S**upply
e.m.f.	**e**lectro**m**otive **f**orce
FFT	**F**ast **F**ourier **T**ransform
HV	**H**igh **V**oltage
HVD1	**H**igh **V**oltage **D**eck **1**
HVD2	**H**igh **V**oltage **D**eck **2**
HVDC	**H**igh **V**oltage **D**irect **C**urrent
HVPS	**H**igh **V**oltage **P**ower **S**upply
ISPS	**I**on **S**ource **P**ower **S**upplies
ITER	**I**nternational **T**hermonuclear **E**xperimental **R**eactor
JET	**J**oint **E**uropean **T**orus
MAMuG	**M**ulti **A**perture **Mu**lti **G**rid
NBI	**N**eutral **B**eam **I**njector
NPC	**N**eutral **P**oint **C**lamped
PS	**P**ower **S**upply
PWM	**P**ulse **W**idth **M**odulation
TL	**T**ransmission **L**ine
RF	**R**adio **F**requency
SINGAP	**SING**le **AP**erture **SIN**gle **GAP**

SOMMARIO

Questo lavoro propone modelli circuitali di tipo innovativo per gli iniettori di particelle neutre delle macchine da fusione, con tensione di accelerazione ben al di là di quelle attualmente in uso. Si tratta di un campo che ha attirato sinora scarsa attenzione in letteratura, benché il salto tecnologico richiesto dall'ambizioso progetto ITER richieda un pari sviluppo degli strumenti di modellistica. Delle soluzioni proposte viene presentata una validazione per confronto con misure sperimentali, assieme a simulazioni di sistema per l'ottimizzazione tanto del funzionamento normale quanto dei dispositivi passivi di protezione.

ABSTRACT

This work proposes novel circuit modelling for neutral beam injectors of fusion machines, at an acceleration voltage well beyond present devices. So far this field has attracted little attention in literature, although the technological jump implied by the ITER project calls for a similar development of modelling techniques. Of the proposed solutions is offered validation against experimental measurements, along with simulations at system level for optimising normal operation and additional protection components.

INTRODUCTION

Research on controlled thermonuclear fusion of Deuterium and Tritium has been the object of intense efforts for more than half a century. In the 1990s, toroidal machines for magnetic confinement of plasma achieved promising fusion performances, though still distant from the efficiency required for exploitation on an industrial scale. The International Thermonuclear Experimental Reactor (ITER) constitutes the next step in fusion devices of the magnetic confinement family, with the ambition to demonstrate the viability of fusion as a source of energy. The ITER project, about ten times bigger than the largest existing experiments, is currently in the design phase and scheduled to become operational in 2016.

Plasma temperature is one of the physical parameters key to the achievement of reactor relevant conditions and the injection of high energy beams of neutral atoms is one of the techniques employed to heat fusion plasmas. Neutral beam injection, involving electrostatic acceleration of an ion beam and subsequent neutralisation by charge exchange collisions, requires a complex power supply system. Energy is transferred to the ion beam by a High Voltage Power Supply (HVPS), through an array of metallic grids at different potentials. The breakdown between acceleration grids represents a normal operating condition, in response to which the HVPS must be capable of switching off within tens of microseconds.

Existing neutral beam injectors cover a voltage range from several tens of kilovolts to few hundreds kilovolts, the highest acceleration voltage achieved to date being 400 kV. For the ITER neutral beam heating system an acceleration voltage of 1 MV dc is specified, implying a noticeable scientific and technological jump. Issues arise in relation to dc insulation at the unprecedented level of 1 MV, 600 kV being at present the highest industrial dc voltage in long distance transmission of energy. Additionally, since demanding limits must be met to ensure the integrity of the load in a breakdown, careful integration of the components and study of suitable additional protections are required. In literature there exist few circuit models for system analysis of neutral beam power supplies; most of these contributions date back to the early 1980s and were intended to simulate the operation of converters. Progress in the design of ITER neutral beam circuit will need adequate simulation tools, yet to be developed.

This work presents a novel approach to circuit modelling, with specific application to the issues arising in neutral beam injectors. A typical example is the major role of stray capacitance and associated stored energy, both during extraction of the ion beam and during breakdowns between acceleration grids. A first aspect covered in the thesis is the ripple of the HVPS dc voltage, which is reviewed proposing a model that takes into account the distributed nature of stray capacitance. Employing the distributed model, the issue is investigated of the switching patterns for groups of series connected rectifiers, as present in the HVPS design. This will lead to a recipe for the minimisation of the ripple that differs from the indications of low voltage converter theory.

Another area of work is represented by the crucial analysis of the behaviour of the circuit following a breakdown between acceleration grids. The resulting transient waveforms must not damage the injector and for this purpose additional protections might have to be foreseen. In general, predicted breakdown voltages and currents will affect deeply the design, e.g. in defining the structure of electrical insulation. A specific aspect considered here, with important practical implications, concerns the transient voltage distribution in the grounded conductor of the circuit, at some distance from the grounding point. Neutral beam systems are typically grounded at a single location, represented by the injector itself. A first model of ITER neutral beam injector will be proposed, including stray capacitance of the various components. At this stage the ground will be treated as an ideal reference at constant voltage, all over the spatial distribution of the circuit. The limits in respect of breakdown analysis of such a traditional approach will be highlighted and a novel model, featuring capacitive and inductive coupling with the ground conductor, introduced.

The performance of the new technique in predicting the grounded conductor voltage transient will be put to the test on a real injector, for which a dedicated breakdown model is developed. The validation of the model against experimental results will be illustrated, with positive results that encourage its application to ITER injector. Breakdown simulations with an enhanced ITER model will be presented. In particular, the anticipated voltage peaks of the grounded conductor at a distance from the grounding point will be discussed, underlining the sharp contrast with the prediction of traditional models. The use of the newly developed tool in assessing different schemes for protection of the injector will also be demonstrated.

1. CONTROLLED THERMONUCLEAR FUSION AND THE TOKAMAK

1.1 Controlled thermonuclear fusion

Fusion is the combination of two atomic nuclei to form a single heavier one. For light nuclei, this is accompanied by release of energy, corresponding to the difference in rest mass between products and reagents. The expression "controlled fusion" refers to the release of fusion energy in a controlled fashion. The term "thermonuclear" indicates that fusion reactions occur in a fully ionised gas of ions and electrons ("plasma"), at high temperature and with close to thermal particle distribution functions [1].
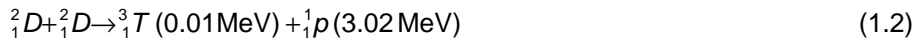
For a fusion reaction to take place, the distance between positively charged nuclei needs to be brought within the range of nuclear forces, i.e. around 10^{-15} m. Overcoming the mutual repulsion of electric charges of the same sign ("Coulomb barrier") requires, with the help of the tunnel effect, energies of the order of some tens of kiloelectronvolts. Controlled thermonuclear fusion implies therefore production and control of high temperature plasmas.

At a temperature of about 10 keV, the most accessible of the fusion reactions and the one over which research has focused for the past decades, is the following:

$$_1^2D + {_1^3}T \rightarrow {_2^4}He\,(3.5\,\mathrm{MeV}) + {_0^1}n\,(14.1\mathrm{MeV}) \tag{1.1}$$
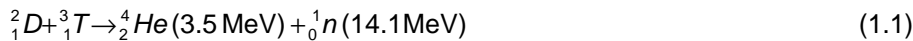
Deuterium is present in water with a concentration of one atom every 10^4 atoms. Tritium does not exist in nature and can be obtained from Lithium through neutron bombardment.

At temperatures between 30 and 40 keV, the following reactions could be exploited:

$$_1^2D + {_1^2}D \rightarrow {_1^3}T\,(0.01\mathrm{MeV}) + {_1^1}p\,(3.02\,\mathrm{MeV}) \tag{1.2}$$

$$_1^2D + {_1^2}D \rightarrow {_2^3}He\,(0.82\,\mathrm{MeV}) + {_0^1}n\,(2.45\,\mathrm{MeV}) \tag{1.3}$$

These are more difficult to achieve than D-T reactions and do not have immediate prospects.

For a fusion reactor, one needs to consider the conditions under which fusion reactions burn in a self-sustained fashion ("ignition"), i.e. without externally applied heating. In the plasma energy balance, the source term is represented by the fraction of fusion power associated with charged particles (the α-particle in the case of the D-T reaction). This energy may be transferred, in part or in total depending on plasma conditions, to the plasma itself. The plasma power loss is characterised by a parameter known as the energy confinement time τ_E; the longer the energy confinement time, the lower the rate of plasma energy loss. The power balance of a burning plasma requires that α-particle heating be at least equal to the plasma power loss, leading to a constraint on the minimum value of the triple product of particle density n, particle temperature T and energy confinement time τ_E. For a Deuterium-Tritium plasma with flat density and temperature profiles the condition to be met is [1]:

$$n \cdot T \cdot \tau_E > 3 \cdot 10^{21} \ \mathrm{m^{-3} \cdot keV \cdot s} \tag{1.4}$$

Based on present fusion experiments, target values of these parameters for ignition are $n \sim 10^{20}$ m^{-3}, $T \sim 10$ keV and $\tau_E \sim 1$ s. At the dawn of research on controlled fusion in the early 1950s, the value of the triple product in the experiments of the time was around 10^{14} m$^{-3} \cdot$keV$\cdot$s. Since then progress has been enormous and nowadays the triple product has reached 10^{21} m$^{-3} \cdot$keV$\cdot$s [2]. Of the various fusion experimental devices, the *tokamak* (see §1.2 below) has achieved the best performance and represents the most promising configuration for the construction of a future fusion reactor.

1.2 The tokamak

Thermonuclear plasmas have low density and are produced inside vessels with good vacuum properties, the pressure of the background gas typically not exceeding 10^{-7} mbar. Magnetic fields are used to confine the plasma, thus avoiding contact with the walls of the vacuum vessel that would result in a quick loss of energy and contamination of the plasma. The term of Russian origin "tokamak" indicates an axisymmetric device for magnetic confinement of plasma, with the structure shown in fig. 1.1.
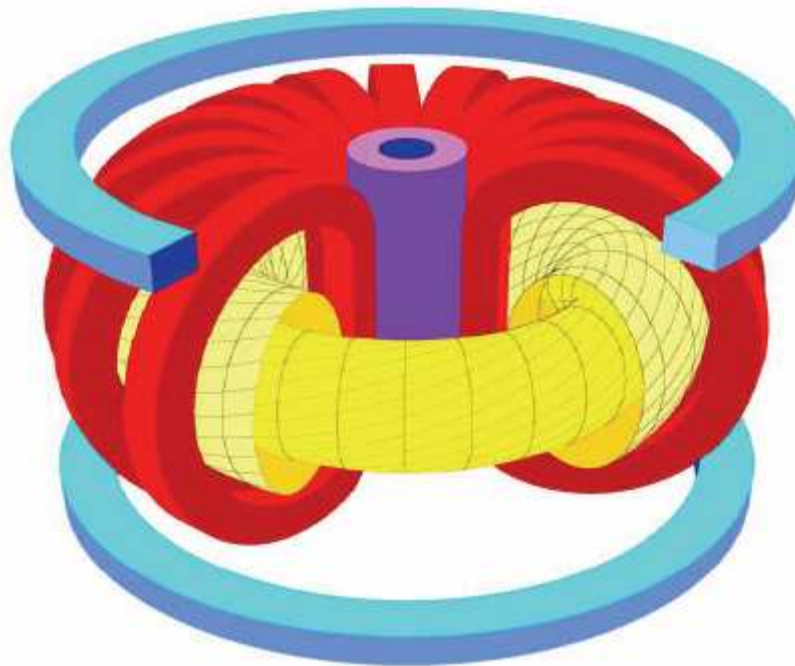
FIG. 1.1 – GEOMETRY OF A TOKAMAK [3]

In a toroidal device, stable equilibrium between plasma kinetic pressure and magnetic forces requires the combination of a magnetic field along the axis of the torus ("toroidal field") with a magnetic field in the plane perpendicular to the axis of the torus ("poloidal field"). The toroidal field is generated by coils (shown in fig. 1.1 as red D-shaped rings) external to the vacuum vessel. The poloidal field of a tokamak is generated by a toroidal current flowing in the plasma. The toroidal field is the main magnetic field, the poloidal magnetic field being an order of magnitude smaller. Additional magnetic fields, produced by toroidal coils (shown as light blue rings in fig. 1.1), are necessary for plasma vertical stabilisation.

In the majority of the existing tokamaks the plasma current is driven by a flux swing in a magnetic circuit linked to the plasma column, which behaves like the secondary winding of a transformer. This, known as "inductive current drive", is unable to sustain steady state operation, due to the physical limit on the current of the primary winding (shown as a purple hollow cylinder in fig. 1.1). Alternative methods for steady state current drive have been an important subject of tokamak experimental investigation and represent a key issue for future experiments [4].

Plasma current also provides the basic heating mechanism of tokamaks. However, since plasma electrical resistivity decreases with increasing electron temperature, ohmic heating becomes increasingly less effective at higher temperatures. In a tokamak the maximum temperature reachable with purely ohmic heating is around 1 keV. Additional heating methods are therefore required to take the plasma to ignition [1]. At the same time, any mechanism capable of delivering energy to the plasma particles also delivers momentum and may in principle drive an electric current.

The additional heating techniques used in tokamaks and other toroidal fusion devices include electromagnetic waves and high energy beams of neutral particles. Electromagnetic wave heating exploits suitable resonances between plasma particles and radio-frequency fields. Neutral beam heating consists in injecting a beam of highly energetic neutral atoms, which in the plasma become ionised by charge-exchange collisions.

1.3 Joint European Torus and International Thermonuclear Experimental Reactor

At present the largest tokamak is the Joint Europen Torus (JET) [5], located in Culham (United Kingdom). JET, a cooperative effort of several European nations, achieved its first plasma in June 1983 and established the record fusion power of 16 MW in 1997 [6]. Currently JET is the only tokamak that can operate with Tritium fuel. The main design parameters of the JET tokamak are listed in table 1.1. A noticeable feature pioneered by JET (fig. 1.2) is the D-shaped, rather than circular, cross section. The favourable physics properties of D-shaped plasmas lead to similar designs in subsequent tokamaks.

TABLE 1.1 – JET MAIN DESIGN PARAMETERS

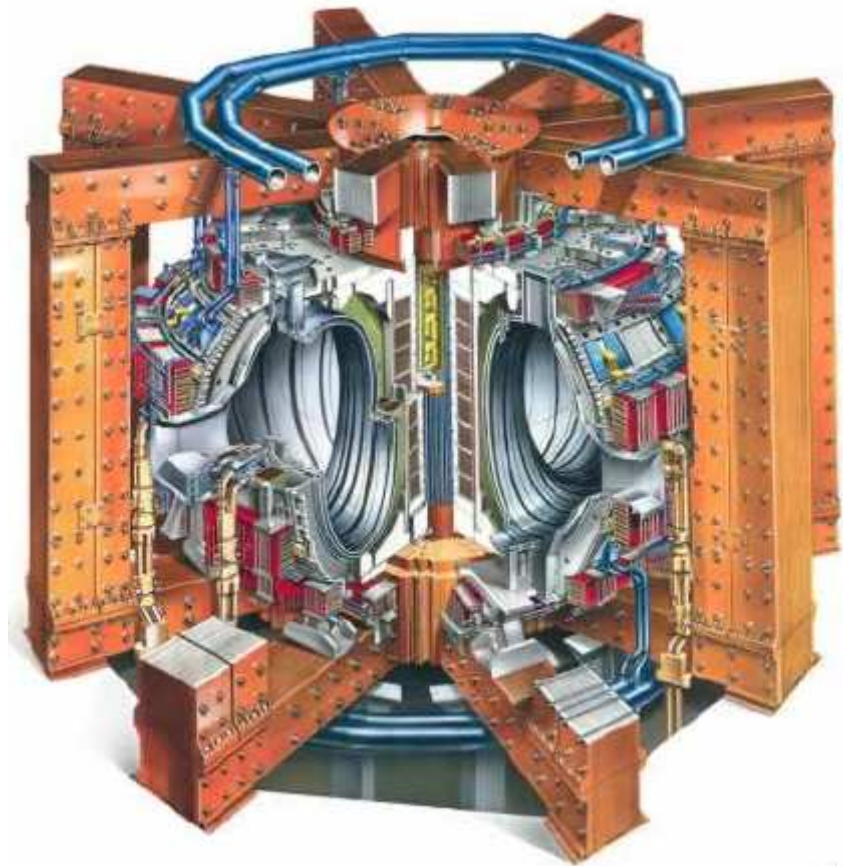| *Parameter*	*Value*
Plasma major radius [m]	2.96
Plasma horizontal minor radius [m]	1.25
Plasma current [MA]	4.8
Toroidal magnetic field on axis [T]	3.45
Flattop pulse length [s]	20

FIG. 1.2 – THE JOINT EUROPEAN TORUS

The "International Thermonuclear Experimental Reactor" (ITER) is the proposed tokamak of next generation [7]. The objective of ITER is the production of 500 MW of fusion power, with a power gain of ten in respect of the input power required to ignite the deuterium-tritium fusion reactions. ITER is sketched in fig. 1.3 and the main design parameters are listed in table 1.2 [8].

ITER will be about ten times larger in plasma volume than JET, with unprecedented thermal and 14 MeV neutron loads. Although the overall design parameters have been agreed, progress in design and construction of ITER will pose significant scientific and technological challenges for many years to come. Work at the chosen site in Southern France has commenced in 2007 and ITER is scheduled to become operational by 2016.

TABLE 1.2 – ITER MAIN DESIGN PARAMETERS

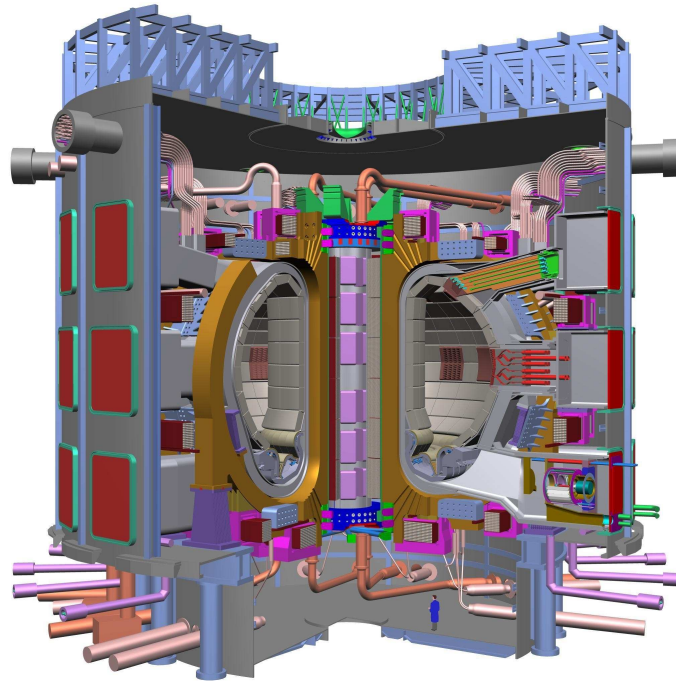| *Parameter*	*Value*
Plasma major radius [m]	6.2
Plasma horizontal minor radius [m]	2.0
Plasma volume [m^3]	840
Plasma current [MA]	15
Toroidal magnetic field on axis [T]	5.3
Flattop pulse length [s]	400
Fusion power [MW]	500
Power amplification	> 10

FIG. 1.3 – THE INTERNATIONAL THERMONUCLEAR EXPERIMENTAL REACTOR

2. NEUTRAL BEAM INJECTION IN FUSION DEVICES

2.1 Basic concepts

The plasma current of a tokamak constitutes the first mechanism for raising the temperature of the plasma itself. However this alone is insufficient to reach the temperature required by fusion reactions and additional heating techniques are used, including high energy beams of neutral particles and electromagnetic waves [1].

Neutral beam heating consists in injecting a beam of highly energetic neutral atoms, which in the plasma become ionised by charge-exchange collisions. The injection of neutral beams is a process involving four distinct stages (fig. 2.1): production of ions, electrostatic acceleration of the ion beam, neutralisation and deflection of residual ions. Neutralisation allows the beam to go through the strong magnetic field of the machine undeflected, thus reaching the plasma [9].
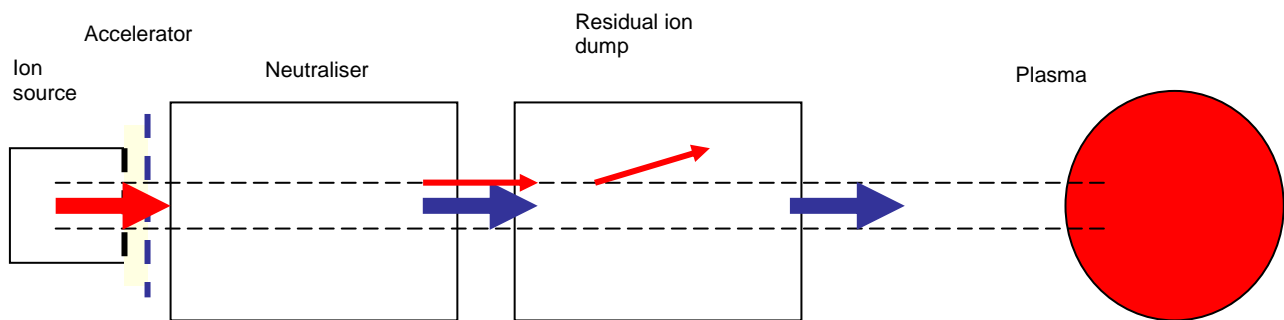

FIG. 2.1 – PRINCIPLE OF NEUTRAL BEAM INJECTION

The ion source is a chamber where the ions of the selected gas (in fusion machines often Hydrogen or Deuterium) are produced. Ion sources are designed and operated to maximise the extraction of a specific ion, either positive or negative. In general, production of positive ions relies on volume phenomena and is simpler than that of negative ions, enhanced by surface phenomena involving some additional atomic species like Caesium [10]. Optimisation of the performance of an ion source is complex and involves several aspects of construction and physical parameters [11]. The layout of the magnetic fields is especially important in maximising the fraction of desired ions in the resulting beam. The pressure in the ion source is constrained by the need to keep sufficiently low the pressure of the background gas in the downstream accelerator.

Ion sources exploit two distinct phenomena to produce ions, either arc or inductive coupling of radio-frequency power. In ion sources of the arc type, a thermal arc is established between the body of the ion source (anode) and hot tungsten filaments (cathode) emitting thermionic electrons [12]. The discharge is run in the emission limited regime, therefore control of filament heating enables to regulate the ion beam current. Historically arc ion sources were the first used in neutral beam injectors, however the need of periodic replacement of the filaments constitutes a major drawback. This will be especially true for ITER and subsequent reactor-class machines, where the radiation environment will prevent personnel access to the equipment. RF ion sources have been employed on neutral beam injectors in more recent times [13] and offer the advantage of a filament replacement free solution. In this case the amount of radio-frequency power represents the knob by which the ion beam current is adjusted.

The ions are extracted from the source and accelerated by an array of metallic grids at different potential. The voltage of the accelerator, the number and position of intermediate grids and the number and size of the apertures of the grids (fig. 2.2) determine the characteristics of the ion beam. The grid closest to the ion source, known as "plasma grid", is offset by a dc voltage of few tens or hundreds of volts ("bias voltage") with respect to the body of the source. For existing neutral beam heating systems, the voltage of the accelerator ranges from several tens of kilovolts, e.g. 80 kV of JET early injectors [14], to a maximum of 500 kV on JT-60U [15]. The ion beam can be accelerated over a single acceleration gap or in several stages; as an example, in the quoted 500 kV NBI of JT-60U, three main acceleration gaps are present. A common design feature of neutral beam accelerators is the compromise between beam optics and voltage holding, two aspects having opposite needs: longer gaps between the grids help electrical insulation, while deteriorating the optics of the ion beam. In general the distance between grids is close to the breakdown limit in vacuum and during operation breakdowns occur routinely. The full voltage holding capability of the system is achieved in a gradual process of "conditioning", starting at a voltage as low as a third of the nominal value.
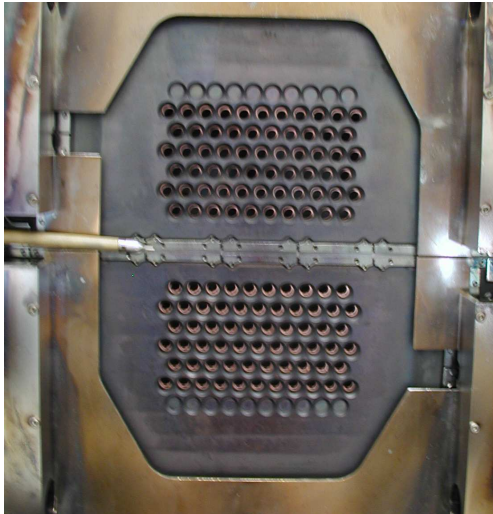
The ion beam output by the accelerator goes through the "neutraliser", typically consisting in a region with neutral gas at a favourable pressure for charge-exchange collisions. The neutralisation efficiency is not 100% and ions still present in the beam at the exit of the neutraliser are deflected, either magnetically or electrically, onto a "residual ion dump". The remaining neutral beam reaches the plasma unaffected by confinement magnetic fields.

The main parameters of a neutral beam are energy and power. The energy determines the acceleration voltage and dictates the type of source, based either on positive or negative ions. Negative ions are the only option at energies above 160 keV, for which the neutralisation efficiency of positive ions becomes vanishingly small [9]. The overall efficiency of neutral beam injection is low and ranges between 20% and 30%, a significant fraction of the ion beam energy being lost in the residual ion dump. The current to be supplied by the ion source is determined by the target neutral beam power. The desired ion beam current also affects the design of the accelerator, because optimum beam optics requires that, for a given geometry, the ratio between accelerator voltage and beam current correspond to a fixed value, known as "perveance match" [16].

FIG. 2.2 -– PLASMA GRID FOR A NEGATIVE ION SOURCE TEST STAND AT GARCHING, GERMANY

2.2 The power supply system

A Neutral Beam Injector (NBI) requires a complex power supply system, with many distinct pieces of equipment. Four main blocks can be identified (fig.2.3):

1) The "High Voltage Power Supply" (HVPS), feeding the accelerator, is the main plant in terms of rated power and voltage. The HVPS outputs a dc power that corresponds to the combination of acceleration voltage and ion beam current.

2) The "Ion Source Power Supplies" (ISPS), needed for the operation of the ion source. Exact number and nature of the ISPS depend on the type of source, arc or radio-frequency.

3) A high voltage "Transmission Line" (TL), carrying electrical, gas and cooling supplies to ion source and accelerator.

4) Additional protection components, necessary to safeguard the accelerator from grid breakdowns (e.g. series resistors and core snubbers [17]).

In most designs, the grid at the exit of the accelerator, known as "post-acceleration grid", is at ground potential. As a consequence, the plasma grid and the ion source to which it is electrically linked (except for the small bias voltage, see §2.1) sit at a potential to ground corresponding to the highest voltage pole of the HVPS. This implies that also the ISPS need to be insulated from ground for a voltage corresponding to the rating of the HVPS. In many instances (e.g. on JET [18]) this is achieved installing the ISPS inside a Faraday cage, supported on post insulators and fed via an isolation transformer. Another common feature is the adoption of a single reference to ground for the whole circuit, at the neutral beam injector end. The ground pole of the HVPS has therefore to be insulated from local ground.

Neutral beam injectors are subject, as described above (§2.1), to more or less frequent breakdowns between accelerator grids. These represent routine events that the system must be capable of surviving without damage to the accelerator and without deterioration of the voltage holding capability. Dedicated studies [19] showed that load protection can be ensured limiting fault energy and peak current. This has a number of implications, noticeably the power supplies of the accelerator must respond to a grid breakdown switching off within few tens of microseconds. In general, capacitive stored energy must be minimised.

Two main requirements apply to the HVPS: it has to provide a regulated dc output voltage with low ripple to ensure perveance match and it needs to cut off in tens of microseconds for load protection purposes. The number and voltage rating of the output terminals of the HVPS is related to the structure of the accelerator it feeds: in case of a single acceleration stage, a single high voltage output is provided. Over the decades a variety of solutions have been employed in the design of a HVPS, reflecting the technology available at the time. The 160 kV HVPS of JET early injectors [18] is based on the complex "star-point controller" topology

[20], combined with isolation transformers and high voltage diode rectifiers. Thyristors perform slow regulation on the low voltage side of the isolation transformer and a tetrode, acting as series switch, performs fast regulation and guarantees removal of the output voltage within 10 μs from detection of a grid breakdown. Nowadays solid state inverters on the low voltage side of the isolation transformers perform both functions of fast regulation and cut off [21,22,23], simplifying considerably the design.
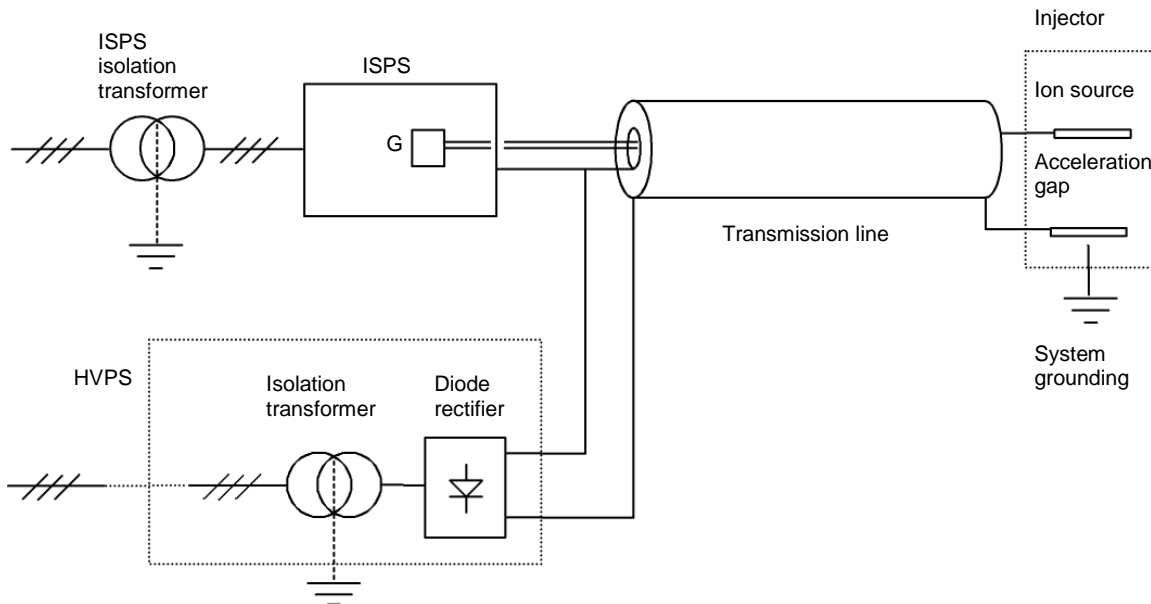

FIG. 2.3 – BLOCK SCHEME OF THE POWER SUPPLY SYSTEM FOR A NEUTRAL BEAM INJECTOR

Power to the ion source and accelerator is carried by a high voltage "Transmission Line" (TL), often gas insulated to minimise capacitively stored energy. If the accelerator has a single stage, the transmission line can be coaxial with two main conductors: the inner conductor is connected to the high voltage terminal of the HVPS and the outer conductor to the other pole, grounded at the load end. Electrical, gas and cooling supplies to the ion source, at high potential with respect to ground, are housed inside the inner conductor of the transmission line (as shown in fig. 2.3 for a sample radio-frequency generator G of a hypothetic RF ion source).

As mentioned above, protection of the accelerator imposes strict limits to peak current and energy delivered to the fault in a grid breakdown. To meet these limits, fast cut off of the power supplies is generally not sufficient and additional protection components must be inserted in the circuit. Such devices can be either passive, typically resistors, inductors and core snubbers, or active, namely series switches and short circuiting devices (also known as "crowbars"). A core snubber [17], typical passive protection component found in neutral beam circuits, consists in a hollow cylinder of ferromagnetic material placed around a conductor. This constitutes an extra inductance that limits the rate of rise of the fault current in a short circuit. Active devices were associated to the use of vacuum tubes and have been abandoned in recent neutral beam systems with solid state power supplies. Moreover, the construction of a dc breaker rated for the extra high voltage required by present and future negative ion based neutral beams is beyond present technology.

2.3 Circuit modelling

The extraction of an ion beam with good optic properties requires low ripple (few percent) of the HVPS output voltage, to ensure the perveance match condition (§2.2) is met. Smoothing filters of the RC type may have to be included in the design, with the size of the filter capacitance playing a crucial role in limiting the rate of rise of the HVPS output voltage in case of sudden loss of load. The storage of capacitive energy associated to an RC filter goes against the general protection principles of the accelerator grids. These conflicting requirements exemplify how coordination of the design of the different items present in the high voltage circuit of a neutral beam injector requires adequate analysis tools at system level. This applies equally to the assessment of the additional protection devices needed to limit breakdown energy and peak current, to which various components contribute.

Complete circuit models of an entire NBI have rarely appeared in literature [22]. The importance of these is related to the prediction of transient breakdown currents and voltages. Furthermore, grounding policies alternative to the single earthing point at the injector end have not been considered up to now. With the foreseen steep increase in voltage of future negative-ion-based NBIs, rapid transients, stray capacitance, role of the ground conductor and distributed nature of the components are those aspects to which special attention will have to be paid in developing circuit simulations.

3. THE POWER SUPPLY SYSTEM OF ITER NEUTRAL BEAM INJECTOR

3.1 ITER neutral beam injector

The availability of neutral beam power will be essential for ITER to achieve its target fusion power [24]. In the ITER design, injection of Deuterium at the energy of 1 MeV is foreseen. Such a figure is unprecedented, the highest neutral beam energy achieved so far in fusion devices being 400 keV [15], and implies an acceleration voltage of -1 MV dc. Efficient neutralisation requires that the ion source be of the negative ion type. The key requirements of ITER neutral beam injector are summarised in table 3.1 [25].

TABLE 3.1 – SPECIFICATIONS OF ITER NEUTRAL BEAM INJECTOR

Parameter	Value
Power of neutral beam	16.7 MW
Ion beam current	40 A
Acceleration voltage	-1 MV
Pulse length	3600 s

Two alternative accelerator designs are candidates for ITER, "Multi Aperture MUlti Grid" (MAMuG) [25] and "SINGle APerture SINgle GAP" (SINGAP) [26]. In MAMuG, negative ions are accelerated to the energy of 1 MeV in five identical acceleration gaps of 200 keV each. The SINGAP solution instead foresees a single main acceleration gap of about 300 mm length. In the work described here, SINGAP has been adopted as reference, although issues and modelling approach apply equally to MAMuG.

In SINGAP the voltage across the main acceleration gap is somewhat less than 1 MV, nominally 940 kV. Upstream of the main acceleration gap, a 60 kV "pre-acceleration" gap is present. The sum of pre-acceleration and main acceleration voltage gives the nominal 1 MV of the ITER specification. Upstream of the pre-acceleration gap is a further 12 kV "extraction gap", functionally part of the ion source. A total of four grids is involved (fig. 3.1):

- Plasma grid, at a nominal potential to ground of -1012 kV

- Extraction grid, at a nominal potential to ground of -1000 kV

- Pre-acceleration grid, at a nominal potential to ground of -940 kV

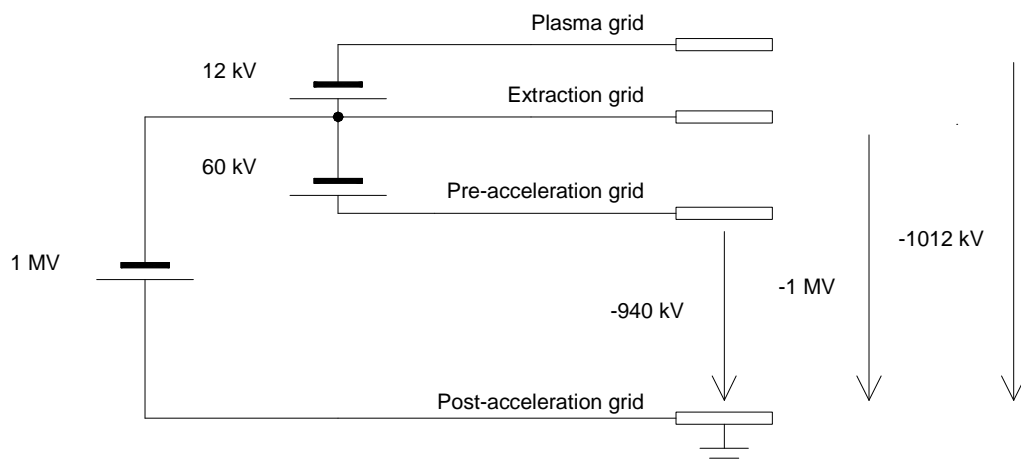- Post-acceleration grid, electrically connected to ground.

FIG. 3.1 – SKETCH OF THE ITER SINGAP ACCELERATOR, SHOWING GRIDS AND VOLTAGES

The grid system of an ITER MAMuG accelerator, shown for a comparison in fig. 3.2, is more complex. From the power supply standpoint MAMuG has significant complications, because it requires feeding to the

accelerator four intermediate voltage conductors, at -200 kV, -400 kV, -600 kV and -800 kV with respect to ground.
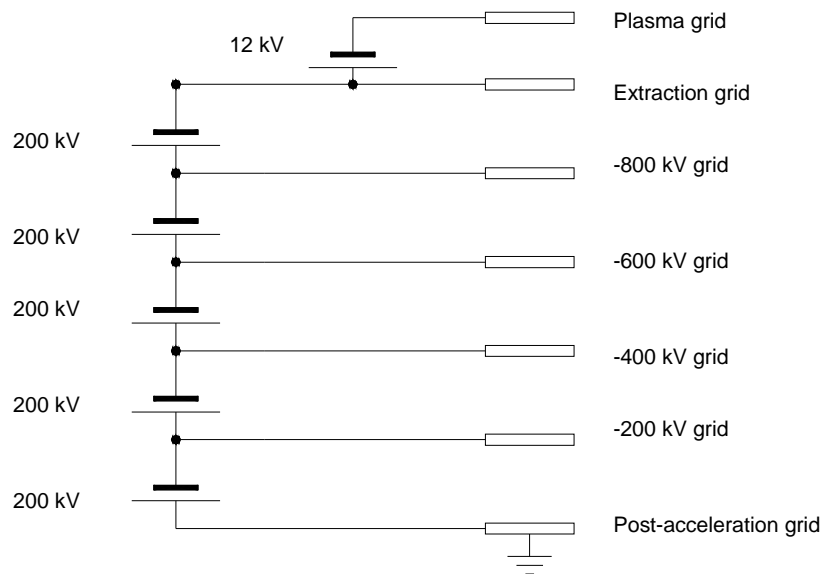

FIG. 3.2 – SKETCH OF THE ITER MAMUG ACCELERATOR, SHOWING GRIDS AND VOLTAGES

3.2 Power supply scheme

The power supply system of ITER neutral beam injector will follow the general structure described in §2.2 and shown in fig. 2.3. Each of the four major components of the circuit is discussed in greater detail in the sections below: High Voltage Power Supply (§3.2.1), Ion Source Power Supplies (§3.2.2), Transmission Line (§3.2.3) and passive protection devices (§3.2.4). Important aspects affecting the power supplies are the type of negative ion source and accelerator to be fed. A radio-frequency driven ion source has been selected for ITER NBI. The choice between MAMuG and SINGAP accelerator is still open and anticipated to require several more years of research and development. The type of accelerator affects the design of HVPS and, to an even greater degree, transmission line. In MAMuG the HVPS has to provide five regulated and filtered dc voltages, nominally at -200 kV, -400 kV, -600 kV, -800 kV and -1 MV to ground; on the contrary SINGAP involves a single -1 MV output. Similarly, the MAMuG transmission line includes five main high voltage conductors, with associated multiple insulation issues - in between conductors and between each conductor and ground. For the analyses described in the following chapters, SINGAP has been adopted as reference and no further discussion will be devoted to MAMuG.

The electrical connection among the main pieces of equipment plays a crucial role in determining the behaviour of the circuit under fault conditions. In SINGAP, the HVPS is connected to ISPS and to the accelerator by a coaxial Transmission Line. The outer conductor of the TL is connected to the post-acceleration grid, in turn connected to ground and representing the only intended reference to ground of the circuit. Wherever possible and with the help of electrostatic screens, the unavoidable stray capacitance of high voltage parts is referred to the return conductor of the transmission line (hereinafter referred to as "return conductor"), rather than to ground. If this were possible in all cases, the fast transients and disturbances resulting from a grid breakdown would stay within the envelope of the return conductor and would not affect significantly external structures. It will be shown in §3.2.2 that is not the case, because of the design choices relating to the power supplies of the ion source. At modelling level, the implication is that an innovative approach is required to distinguish the roles of return conductor and ground.

3.2.1 The High Voltage Power Supply (HVPS)

The design of the HVPS is being developed along the line of a modular structure with five series connected stages, each of rated output 200 kV 59A dc and insulated to ground for up to -1MV dc [27]. Insulation to ground of the individual stage is ensured by an isolation transformer, fed on the primary side by a three-phase inverter working at 150 Hz. This solution ensures that the high voltage output that can be switched off rapidly - within few tens of microseconds - by blocking the inverters, as required by the strict protection

requirements of the neutral beam accelerator Regulation of the output voltage over a large range of variation (20% – 100%) is performed modulating the ON time of the inverter square voltage waveforms. Here it is assumed that the inverter be of the "Neutral Point Clamped" (NPC) type [28], with resulting stepped voltage waveforms of the line to line voltage (fig. 3.3). A three-phase line frequency rectifier supplies, via a capacitor bank, the inverter. The isolation transformer is also a step-up transformer: the rated primary voltage, selected in consideration of the NPC inverter, is of the order of few kilovolts (5 kV) whereas the rated secondary voltage of 160 kV ensures a rectified dc output of 200 kV per stage. The alternating voltage of the isolation transformer secondary windings is rectified by a three-phase high voltage diode rectifier and smoothed by an RC output filter (fig. 3.4). The diode rectifier adopts the standard structure of the six-pulse Graetz bridge. The isolation transformer defines the boundary between low voltage (primary) and high voltage (secondary) side. With this layout, all semiconductor devices requiring firing circuits sit on the low voltage side, with obvious advantages in design, cost and operation.
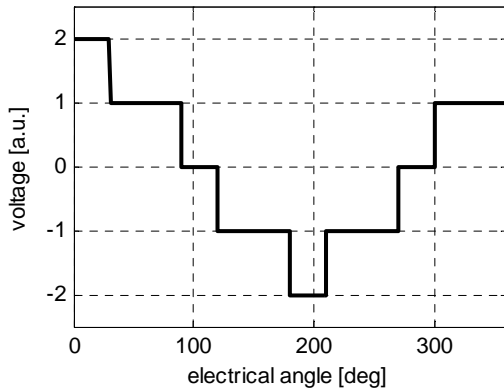

FIG. 3.3 – TYPICAL SHAPE OF THE LINE-TO-LINE VOLTAGE OF AN NPC INVERTER

The HVPS shown in fig. 3.4, if used on a SINGAP accelerator, only has two output terminals: the positive terminal is connected, through the transmission line, to the post-acceleration grid, which is grounded. The conductor connecting positive pole of the HVPS to the post-acceleration grid has been labelled as "return conductor". Note that this conductor is connected to ground at the injector end only; over the rest of its route, the return conductor must be insulated from local ground. The voltage rise of the return conductor with respect to local ground is one of the main areas of investigation of this work (chapter five).

The -1 MV dc isolation transformer mentioned above and the other components on the high voltage side are beyond present technology, the highest voltage used to date in HVDC transmission being 600 kV [29]. In principle, a design with different insulation levels is possible, where the rating is -200 kV dc for the first stage, -400 kV dc for the second and so on, down to -1 MV dc for the fifth and last stage. Here it is assumed that the insulation transformers be all identical and rated for -1 MV dc to ground.

The transformer circuit parameters important in building a circuit model for fast transients are leakage inductance, capacitance to screen, capacitance to tank and series capacitance. The leakage inductance was determined from the value of short-circuit impedance (16%) found in literature [27] The capacitance to screen of each high voltage winding C_{wc} is computed as for a cylindrical capacitor of internal radius R_i=0.35 m (estimated outer radius of the electrostatic screen), external radius R_e=0.6 m (estimated inner radius of the high voltage winding) and height H=1.5 m. A relative dielectric constant ε_r=3 is used, which seems reasonable considering that for mineral oils values between 2.2 and 3.3 have been reported [30] and that also some solid insulation is likely to be present:

$$C_{WS} = \frac{2 \cdot \pi \cdot \varepsilon_r \cdot \varepsilon_0}{\ln\left(\dfrac{R_e}{R_i}\right)} \cdot H = \frac{2 \cdot \pi \cdot 3 \cdot 8.85 \cdot 10^{-12} F/m}{\ln\left(\dfrac{0.6m}{0.35m}\right)} \cdot 1.5m = 460 pF \qquad (3.1)$$
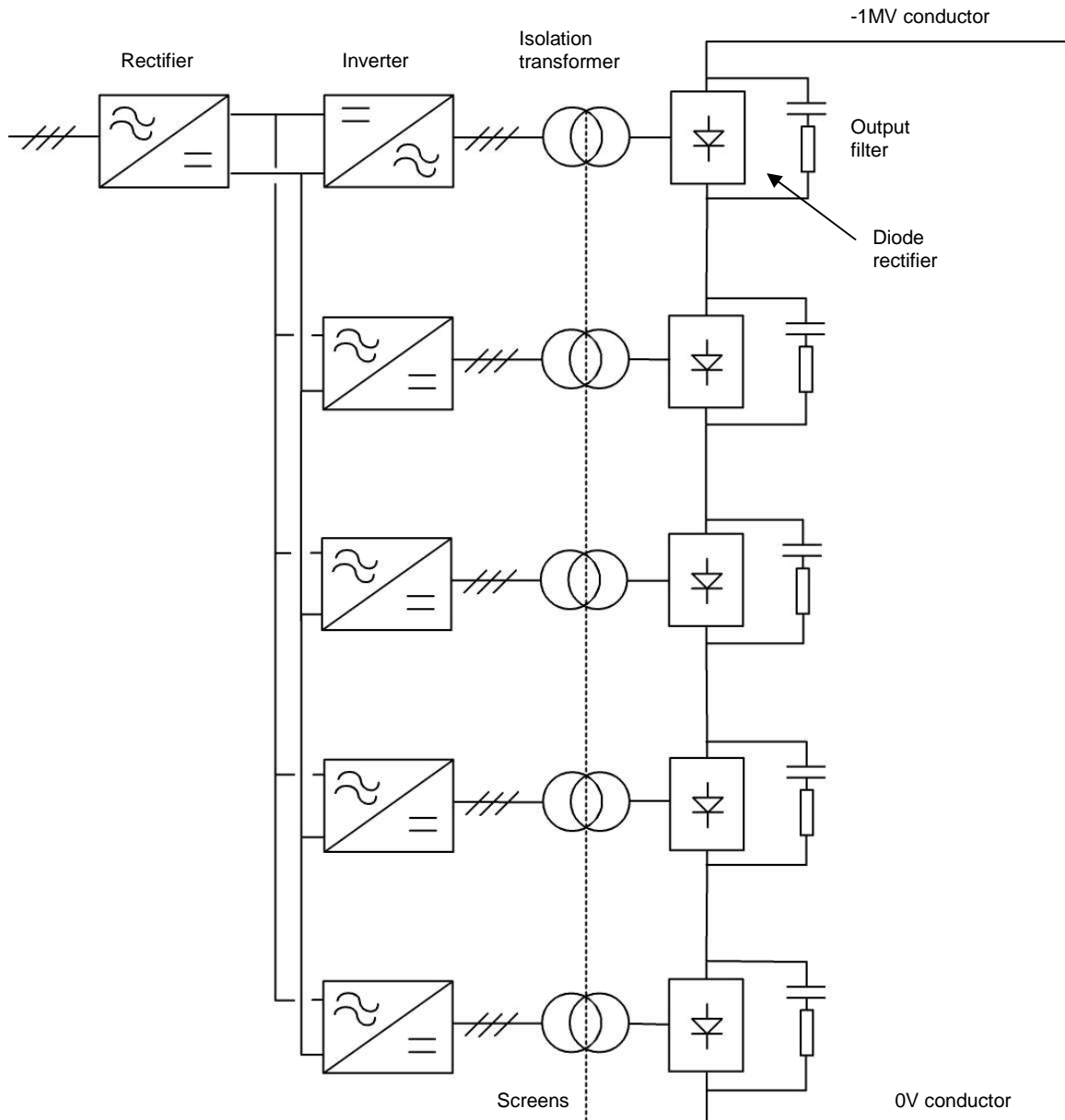
FIG. 3.4 – CIRCUIT DIAGRAM OF THE HVPS FOR ITER NBI

The capacitance C_{WT} between high voltage winding and surrounding structures, i.e. transformer tank, is expected to be smaller than C_{WS}, because of the longer distances. A precise calculation of C_{WT} would require knowledge of the geometry of the transformer; here it has been estimated as half of C_{WS}. The winding series capacitance, representing the equivalent of all interturn capacitances, is taken to be 1/100 of the capacitance to screen, following a sample transformer described in [31]. The resulting stray capacitances associated to each high voltage winding are shown in fig. 3.5. The transformer bushings are also anticipated to contribute large stray capacitance; a value as high as 1200 pF was measured for the oil to air bushing of an HVDC energy transmission system at 600 kV [32]. The HVPS isolation transformer bushing is of the oil to gas (SF6) type, the diode rectifier tank being SF6 insulated. Here 600 pF is assumed for the capacitance of the isolation transformer bushing, considering that, with respect to oil to air bushings of equal voltage rating, oil to gas bushings are shorter.

In fig. 3.4, the electrostatic screens of all high voltage windings are connected to the return conductor, rather than to local ground. The underlying logic is to keep as much as possible of the capacitive stored energy between high voltage conductors and return conductor: if the screen was connected to local ground, during a breakdown the energy stored in the stray capacitance of the high voltage windings would discharge to local ground and through the soil back to the grounding point of the injector. The resulting transient voltages and currents are difficult to predict and no earlier simulations in an integrated neutral beam circuit model are

known of. As an example, one might ask what peak voltage is to be expected between the electrostatic screen of the high voltage winding and the earthed transformer tank. Although purely qualitative for now, this discussion should make obvious the importance to the design of suitable analysis tools, yet to be developed. In chapters four and five, some weak points of traditional simulations will be exposed and subsequently addressed.
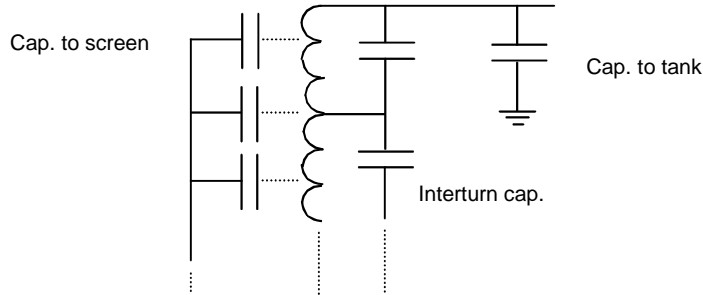

FIG. 3.5 – STRAY CAPACITANCES ASSOCIATED TO THE HIGH VOLTAGE WINDING OF THE ISOLATION TRANSFORMER

A smoothing filter of the RC type is foreseen downstream of each high voltage diode rectifier, to meet the output voltage ripple requirement (±5%) imposed by perveance matched operation. Also the firing strategy of the inverters of each HVPS stage affects significantly the ripple; an aspect covered in greater detail in chapter four. In principle, the filter capacitance should be kept as low as possible, to minimise stored energy that contributes to fault energy and peak current in a grid breakdown. In practice, it turns out that the filter capacitance has also a beneficial role, in limiting the rate of rise of the output voltage in case of sudden loss of the ion beam (e.g. due to a fault in the gas feed system or in the ion source power supplies). Some optimisation is therefore required and the underlying analysis tools are developed in the next chapter.

The salient circuit parameters and specifications of the high voltage power supply, as used hereinafter for all circuit simulations, are summarised in table 3.2.

TABLE 3.2 – MAIN CIRCUIT PARAMETERS OF THE HVPS

Parameter	Value
HVPS rated dc output (Deuterium operation)	1 MV 59 A
Maximum ripple of the HV dc output	5%
Isolation transformer rated power	12 MVA
Isolation transformer primary voltage	5 kV
Isolation transformer secondary voltage	160 kV
Isolation transformer short-circuit impedance	16%
Capacitance to screen of isolation transformer winding	460 pF
Capacitance to tank of isolation transformer winding	230 pF
Series capacitance of isolation transformer winding	4.6 pF
Capacitance of isolation transformer bushing	600 pF
High voltage rectifier snubber (equivalent per branch)	10 kΩ 10 nF
Filter capacitance (per stage)	300 nF
Filter resistance (per stage)	68 Ω
Filter tank capacitance	600 pF

3.2.2 The Ion Source Power Supplies (ISPS)

The power supplies for the ion source of ITER NBI have to operate at a voltage to ground determined by the HVPS, up to the rated value of -1 MV dc. Insulation is ensured by feeding the ISPS through an isolation transformer and by physically housing them inside an indoor metallic cage, supported on post insulators capable of withstanding a voltage of -1 MV dc [33]. The ISPS platform in the ITER jargon goes under the name of "High Voltage Deck 1" (HVD1) and has approximate dimensions of 12 m length by 8 m width by 10 m height (fig. 3.6). The estimated length of the post insulators is around 5 m.

In terms of power, the three largest pieces of equipment inside HVD1 are:

- The four 1 MHz RF generators [34]

- The Extraction Grid Power Supply (EGPS)
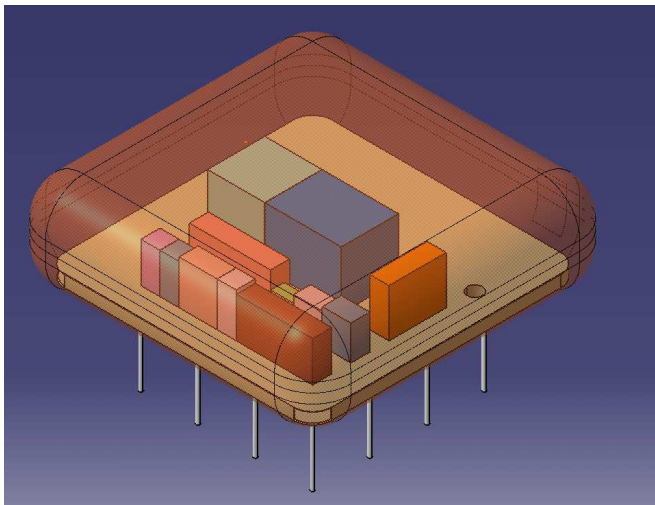
- The pre-acceleration grid power supply.

The RF generator supplies multi-turn coils (fig. 3.7) and by inductive coupling of the radio-frequency power to the gas inside the ion source generates a plasma. The EGPS extracts an ion beam from the ion source, subsequently accelerated by the pre-acceleration grid power supply to up to 60 kV across the pre-acceleration gap. Like the HVPS, in case of breakdown the extraction grid and pre-acceleration grid power supplies have to switch off rapidly, within 100μs. The key features of the main ISPS are listed in 3.3:

FIG. 3.6 – THREE-DIMENSIONAL VIEW OF "HIGH VOLTAGE DECK 1"

TABLE 3.3 - ESSENTIAL FEATURES OF THE MAIN ISPS

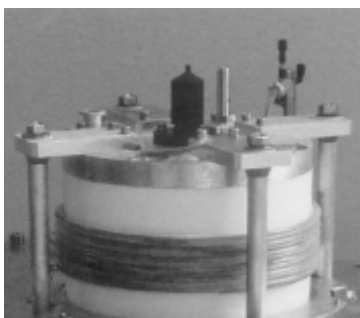|	*RF generators*	*Extraction Grid PS*	*Pre-acceleration Grid PS*
Number of units	4	1	1
Output ratings (per unit)	250kW 50Ω load	140A 12kV dc 100μs cutoff	6A 60kV dc 100μs cutoff

FIG. 3.7 – SAMPLE COIL OF AN RF ION SOURCE

Here the focus is on those aspects of the ISPS relevant to fault analysis at system level, i.e. stray capacitance and connections to HVPS and transmission line. The scheme outlined above has a significant implication: there exist a direct capacitance between the metallic cage of HVD1 and ground. There is no screening by the return conductor, like in the case of most of the isolation transformer capacitance. During a grid breakdown, the energy associated to HVD1 capacitance discharges and fast voltage oscillations result, involving the return conductor according to its capacitive and inductive coupling with the ground. An estimate of the capacitance of HVD1 is obtained assuming a spherical capacitor, of internal radius R_A=6.9 m and external radius R_B=12 m:

$$C_{HS} = \frac{4 \cdot \pi \cdot \varepsilon_0}{\dfrac{1}{R_A} - \dfrac{1}{R_B}} = \frac{4 \cdot \pi \cdot 8.85 \cdot 10^{-12}\, F/m}{\dfrac{1}{6.9m} - \dfrac{1}{12m}} = 1800\, pF \qquad (3.2)$$

Where R_A has been determined as the radius that gives the same external surface as the one of HVD1 parallelepiped; R_B is computed adding to R_A the estimated length of the post insulators (~5 m). C_{HS} obtained in eq. (3.2) is in good agreement with the figure of 1600 pF resulting from finite element electrostatic analyses [Recchia M., private communication].

The ISPS isolation transformer is the other major contributor of capacitive stored energy. Since insulation to ground for -1 MV dc, similarly to the HVPS isolation transformer(s), has to be ensured, one may reasonably assume similar insulation dimensions of the high voltage (secondary) windings in the radial direction. The height of the winding is likely to be different, since the voltage of the ISPS secondary winding is only 6.6 kV. Following [33], a height of 0.7m is used in determining the winding stray capacitance to screen C_{WIS} with the formula for cylindrical capacitors:

$$C_{WIS} = \frac{2 \cdot \pi \cdot 3 \cdot 8.85 \cdot 10^{-12}\, F/m}{\ln\!\left(\dfrac{0.6m}{0.35m}\right)} \cdot 0.7m = 220\, pF \qquad (3.3)$$

As discussed above for the HVPS transformers, the capacitance to tank C_{WIT} is estimated as half of C_{WIS}. In terms of circuit model, the electrostatic screen of the isolation transformer is connected to local ground, a connection to the "return conductor" appearing problematic.

The parameters of the ISPS, as used in all simulations below, are summarised in table 3.4.

TABLE 3.4 – MAIN CIRCUIT PARAMETERS OF THE ISPS

Parameter	Value
Isolation transformer rated power	5 MVA
Isolation transformer primary voltage	22 kV
Isolation transformer secondary voltage	6.6 kV
Isolation transformer short-circuit impedance	10%
Capacitance to screen of isolation transformer winding	220 pF
Capacitance to tank of isolation transformer winding	110 pF
Series capacitance of isolation transformer winding	2.2 pF
Capacitance of isolation transformer bushing	1000 pF
Filter capacitance (per stage)	300 nF
Filter resistance (per stage)	68 Ω

3.2.3 The Transmission Line (TL)

The high voltage Transmission Line serves the purpose of connecting electrically the HVPS and the ISPS to the neutral beam injector. Additionally, it carries also gas and cooling water supplies to the ion source, ensuring insulation to ground for -1 MV dc.

For the SINGAP accelerator the high voltage transmission line is coaxial, with inner conductor at around -1000 kV to ground [35] and outer conductor connected to ground at the neutral beam injector. Inside the inner conductor of the TL are housed electrical conductors and pipes, mainly for the ion source. These supplies have voltages to ground that depend on their final use: as an example, the RF coils for plasma generation inside the ion source work at the plasma grid potential. Within the injector, there exist three distinct high voltage levels (fig. 3.1):

- The plasma grid and ion source potential, nominally -1012kV to ground;

- The extraction grid potential, nominally -1000 kV to ground;

- The pre-acceleration grid potential, nominally -940 kV to ground.

It is a delicate design choice to which of these three close voltage levels the inner conductor of the transmission line should be connected, with non obvious implications on the behaviour of the system during fast transients. An informed decision on the subject is linked to the results of grid breakdown simulations of the type discussed in the next two chapters of this work.

The baseline layout of the connections considered here is the one in which the inner conductor of the transmission line is connected to the -1000 kV potential, i.e. to the negative pole of the HVPS. This implies that inside the inner conductor of the transmission line have to be housed:

- A conductor connecting the positive pole of the pre-acceleration grid power supply to the pre-acceleration grid (-940 kV to ground). The insulation of this conductor from the inner conductor of the transmission line must withstand 60 kV dc.

- A conductor connecting the negative pole of the EGPS to the plasma grid (-1012 kV to ground). The insulation of this conductor from the inner conductor of the transmission line must withstand 12 kV dc.

- Additional conductors and pipes for the ion source, whose detailed list is beyond the scope of this work. Insulation of these additional services from the inner conductor of the transmission line must withstand 12 kV dc.

Insulation between inner and outer conductor of the ITER NBI Transmission Line will be ensured by SF6 at a pressure of at least 3 bar, in order to meet electrostatic design criteria at the same time as tight constraints of the layout at the ITER site. Complex bushings have to be provided to interface the SF6 environment of the transmission line with HVD1 and injector. In general, the function of a bushing is to provide a vacuum-tight barrier between two different volumes, while feeding through electrical conductors. The ITER NBI transmission line requires two bushings, both rated for -1 MV to ground:

- An air-to-SF6 bushing, at the interface with HVD1

- A vacuum-to-SF6 bushing, at the interface with the injector.

Design and manufacture of the NBI 1 MV bushings is one of the major challenges of the ITER NBI system [36,37].

The circuit parameters of the TL depend on its physical dimensions and here the values quoted in [35] have been adopted. The Transmission line is divided in three sections, as follows:

- A section known as TL1, corresponding to the span between the HVPS (start of the TL) and HVD1 (where the ISPS conductors join the TL);

- A section known as TL2, corresponding to the span between HVD1 and HVD2. HVD2 is an insulated Faraday cage, in principle similar to HVD1 but considerably smaller. The function of HVD2 is to enable cooling water and gas supplies for the injector to join the TL. HVD2 is installed in the vicinity of the NBI and TL2 is the longest of the three TL sections;

- The section known as TL3 corresponds to the span between the HVD2 (where cooling water and gas supplies join the TL) and the -1 MV bushing (interface between TL and injector).

Geometrical data for the three sections of the transmission line are listed in table 3.5. Also the estimated average height of the TL over the ground is indicated; a datum that will be important when considering inductive and capacitive coupling between TL and ground. Limited information [38] is available in literature on the anticipated layout of the NBI plant in general and of the transmission line in particular. The lengths of the TL sections listed in table 3.5 have been worked out from preliminary layout drawings for the ITER site. The estimate of the height over ground is even more uncertain, since for TL1 and TL2 the choice between installation on elevated tray or in underground trench is still open. Here it has been assumed that both TL1 and TL2 will run mostly underground. For TL3 instead, installation on elevated supports is forced by the requirements of integration with the structure of the injector.

Per unit length inductance L_{TL} and capacitance C_{TL} of the transmission line have been computed with the classic formulas for coaxial conductors:

$$L_{TL} = \frac{\mu_0}{4\pi} \ln\left(\frac{R_{OUTER}}{R_{INNER}} \right)$$
(3.4)

$$C_{TL} = \frac{2\pi \cdot \varepsilon_0}{\ln\left(\dfrac{R_{OUTER}}{R_{INNER}} \right)}$$
(3.5)

Where R_{OUTER} is the internal radius of the outer conductor and R_{INNER} the external radius of the inner conductor.

TABLE 3.5 – TRANSMISSION LINE DIMENSIONS AND CIRCUIT PARAMETERS

	TL1	TL2	TL3
Inner diameter	400 mm	400 mm	400 mm
Outer diameter	1100 mm	1100 mm	1650 mm
Inductance per unit length	0.2 µH/m	0.2 µH/m	0.28 µH/m
Capacitance per unit length	55 pF/m	55 pF/m	39 pF/m
Estimated length	30 m	65 m	15 m
Estimated height over the ground (average)	1 m	1 m	10 m

The internal inductance of the conductors can be safely neglected, even more so in the prospective of simulations of grid breakdown, characterised by fast oscillations in the megahertz range [19,39]. Consider the skin depth δ_{ST} of stainless steel (a possible material of choice for the conductors of the transmission line is the AISI 316 grade, with a resistivity $\rho_{st}=7.4\cdot10^{-7}$ Ωm [40]) at the frequency of $f=1$ MHz:

$$\delta_{ST} = \sqrt{\frac{\rho_{ST}}{\pi \cdot \mu_0 \cdot f}} = \sqrt{\frac{7.4 \cdot 10^{-7}\,\Omega m}{\pi \cdot \mu_0 \cdot 10^6\,Hz}} = 0.43\,mm \qquad (3.6)$$

Computing the internal inductance L_{II} of the inner conductor of the transmission line as for a thin cylindrical conductor of thickness δ_{ST}, one gets:

$$L_{II} = \frac{\mu_0}{4 \cdot \pi} \frac{\delta_{ST}}{R_{INNER}} = \frac{\mu_0}{4 \cdot \pi} \frac{0.43\,mm}{200\,mm} = 0.43\,nH/m \qquad (3.7)$$

which is three orders of magnitude smaller than the figure shown in table 3.5.

3.2.4 Passive components for load protection
The neutral beam injector of ITER will be subject to more or less frequent breakdowns between acceleration grids. As discussed above, these events are viewed as part of the operational routine and proper design must ensure that the accelerator is not damaged or its voltage holding capability not deteriorated. The duty of providing adequate load protection falls mainly on the high voltage circuit, where capacitive energy is stored and rapidly discharged upon a fault.
In broad terms, protections can be classified as of active or passive nature. For ITER NBI, the only active response from the power supplies to a grid breakdown is blocking of the switching devices of HVPS, EGPS and pre-acceleration grid PS. No dedicated active protection device is foreseen, since a solid state series switch or short- circuiting device rated for 1 MV dc is considered unrealistic. The power supplies have to switch off within 100 µs from detection of a breakdown, which is a long time in comparison to the timescale of the evolution of the breakdown current, as measured [19,41] and simulated (chapters four and five). The power supply cutoff time can afford to be comparatively long because the large short circuit impedance of the isolation transformers limits the rate of rise of the fault current fed from the inverters. A gross estimate for this rate of current rise can be obtained considering a short circuit of the isolation transformer, only limited by the leakage inductance L_{LEAK} worked out from the short circuit impedance of table 3.2:

$$L_{LEAK} = \frac{1}{2\pi \cdot 150\,Hz} \frac{0.16 \cdot (160kV)^2}{12MVA} = 0.36H \qquad (3.8)$$

For one of the star-connected secondary windings, the following rate of rise of the short circuit current $(di/dt)_{SC}$ results:

$$\left(\frac{di}{dt}\right)_{SC} = \frac{160kV}{\sqrt{3} \cdot 0.36H} = 25 \cdot 10^{-4}\,\frac{A}{s} \qquad (3.9)$$

Over an interval of 100 µs, (3.9) gives an increase of about 25 A, negligible when compared to anticipated peak fault currents on the load in the kiloampère range.

Large stored energy is left in the HVPS output filters after the power supply has switched off. One of the purposes of the passive protections is to minimise the fraction of this energy dissipated into the breakdown. It is generally accepted that protection of a neutral beam injector requires both fault energy and peak current not to exceed given thresholds [19]. Figures for the maximum tolerable breakdown peak current (3 kA) and energy dissipated into the arc (10 J) are quoted in early ITER NBI design studies [42]. A somewhat different approach has been proposed as part of a recent review [43], however the different schemes all foresee additional components to meet their protection criteria. In the breakdown simulations of chapters four and five, the following passive protection devices are included:

- A first core snubber, known as "Core Snubber 1" (CS1), installed at the end of TL2

- A second core snubber, known as "Core Snubber 2" (CS2), installed at the start of TL3

- A series resistor installed at the start of TL1, either on the -1 MV conductor or on the return conductor.

The different sets of circuit parameters proposed by various authors and considered here are summarised in table 3.6. Qualitatively the function of the passive protection components can be explained as follows. In general core snubbers (see §2.2) constitute an additional series inductance, limiting the rate of rise of the fault current. In addition, the core snubbers proposed for ITER NBI [39] employ a dissipative magnetic material, to reduce the energy dissipated into the breakdown. The role of the series resistor is related to the topology of the circuit of an inverter-based HVPS, in which a dc current path exists for the flow of current of inverse polarity, through the diodes of the high voltage rectifier. The additional series resistor as originally proposed [43] should prevent the inversion of polarity of the breakdown current.

TABLE 3.6 – CIRCUIT PARAMETERS OF THE PASSIVE PROTECIONS

Passive protection component	Circuit parameters
Core snubber 1 Reference Alternative scheme	1000 Ω 500 µH 100 Ω 140 µH
Core snubber 2 Reference Alternative scheme	1000 Ω 500 µH 100 Ω 95 µH
Series resistor Reference Alternative scheme	50 Ω 6.8 Ω

3.3 Circuit modelling for ITER neutral beam injector

The power supplies of ITER NBI have to meet various and at times conflicting requirements, linked to both normal operation and load protection in a grid breakdown. A number of design issues at system level arise by the integration of different pieces of equipment: the connections of the isolation transformer screens (§3.2.1) and of the high voltage conductors to the transmission line (§3.2.3) are good examples. At component level, the development of insulation for the record voltage of -1 MV dc and capable of withstanding accelerator breakdowns requires some prior knowledge of the associated transient waveforms. There are several reasons why circuit simulations are important in advancing toward the new technology of the power supplies for ITER NBI. Below the essential features of the neutral beam circuit models found in literature are reviewed (§3.3.1) and compared against the needs outlined above, leading to the identification of open questions (§3.3.2) that call for further progress of the analysis tools.

3.3.1 Existing models

In literature there are few circuit models of neutral beam systems [20,22,44,45,46]. In particular, no instance is known of where the distributed nature of the transmission line and of the transformer winding capacitance has been taken into account. Moreover, the return conductor has always been treated as an ideal "constant voltage" reference throughout the system. These modelling assumptions, originating from design studies where phenomena in the power supply converters were the objective, make it difficult to investigate aspects like fast transients in the transmission line during grid breakdowns, or at all impossible in the case of the voltage rise of the return conductor with respect to ground. The latter and rather specific aspect is not

mentioned anywhere in the neutral beam publications, possibly because it never became an issue for systems of low voltage and small physical dimensions in comparison to ITER's.

Let us spend few more words on the circuit model of Jensen et al. [22]. This is probably the most complete of the published models and has been an extremely useful basis for the model of JET neutral beam circuit presented later in this work (chapter five). The model of Jensen et al. is reproduced in fig. 3.8, showing the following salient characteristics:

1) The ground is treated an ideal constant voltage reference

2) The outer conductor of the coaxial and SF6 insulated transmission line is at fixed ground potential

3) The 85 m long SF6 transmission line is modelled with a single cell

4) The 180 m long power supply cable is modelled with a single cell

5) No stray capacitance is included in particular no capacitive stored energy of the power supply isolation transformers.

The above list deserves some comments.

Point 1) is equivalent to neglecting the ground as a conductor in its own right. With reference to the coaxial transmission line for SINGAP, the role of the ground can be sketched as in fig. 3.9: even if the ground is galvanically isolated from the circuit, as a consequence of the capacitive coupling with the outer conductor of the transmission line, a current distribution J_G may flow in the ground. In turn, the electromotive force (e.m.f.) along the dashed path is non zero, due to the flux linkage with the dotted area. To all effects, the ground is coupled magnetically and capacitively with the transmission line. This stays true also under the assumption of perfectly conducting ground, the main consequence being that J_G is purely superficial [47]. In principle the ground should therefore be treated as one of the conductors of the circuit, although in practice such a refinement of the model is unlikely to be necessary unless fast transients are of interest. Consider as an example the stray capacitance to ground of HVD1, C_{HS} of eq. (3.2). If one compares the associated transverse impedance at a generic frequency f with the TL series impedance (0.2μH/m from table 3.5 and about·100 m length), the frequency f_{GND} at which the two become comparable is given by:

$$f_{GND} = \frac{1}{2\pi} \frac{1}{\sqrt{1.8 \cdot 10^{-9}\,F \cdot 2 \cdot 10^{-7}\,H/m \cdot 100m}} \cong 840\,kHz \qquad (3.10)$$

f_{GND} falls in the range of the breakdown frequencies in neutral beam injectors, typically between hundreds of kilohertz and few megahertz [19,39].

Point 2) is a mere consequence of the assumption under point 1). Point 3) and point 4) limit the scope of the model to phenomena occurring on a wave length λ_{MIN} much larger than the length of the cabling. If one takes λ_{MIN} as ten times greater than the length of the cabling, rounded to 200 m for convenience:

$$\lambda_{MIN} = 10 \cdot L_C = 10 \cdot 200m = 2000m \qquad (3.11)$$

In terms of timescale, the fastest phenomena for which the model could be employed reliably correspond therefore to the frequency f_{MAX}:

$$f_{MAX} = \frac{c}{\lambda_{MIN}} = \frac{3 \cdot 10^8\,m \cdot s^{-1}}{2 \cdot 10^3\,m} = 150\,kHz \qquad (3.12)$$

which is about an order of magnitude lower than the anticipated fast transients at the breakdown.

Point 5) is equally significant, because in the ITER system the large energy stored by stray capacitances can not be ignored in breakdown simulations. As an example, at -1 MV the energy associated to the stray capacitance of HVD1 is (1/2)·(1.8 nF)·(1 MV)^2=900 J, a figure much greater than the maximum tolerable energy into the breakdown.
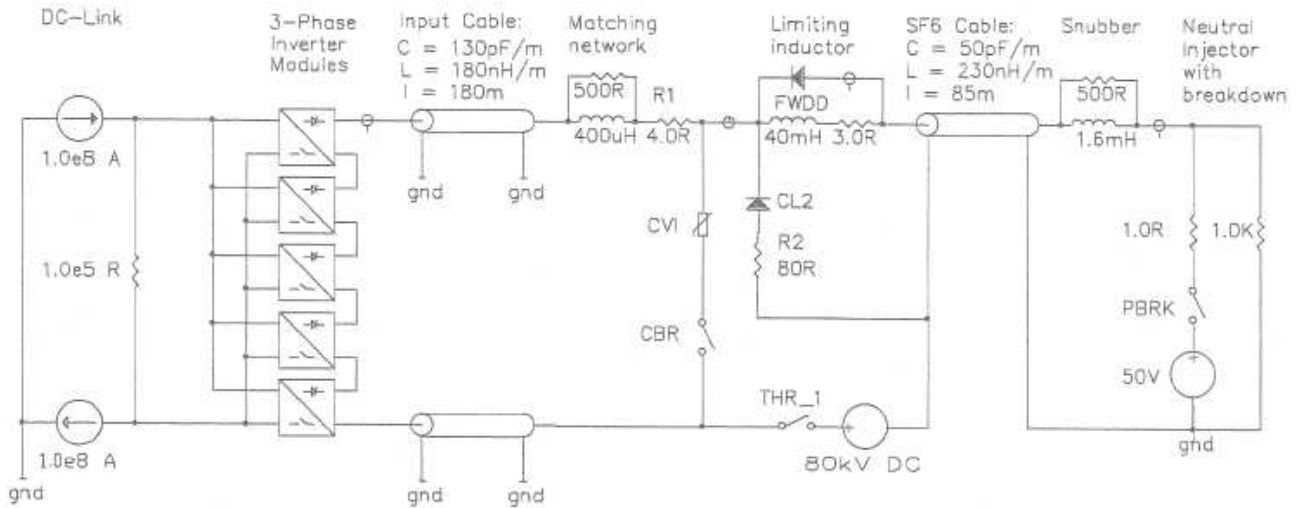
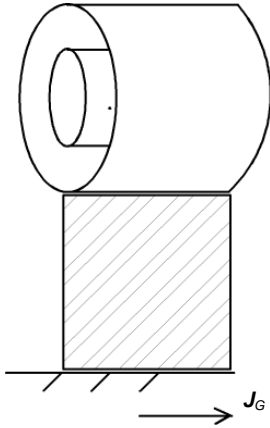FIG. 3.8 – THE MODEL OF JENSEN ET AL. [22] FOR JET NEUTRAL BEAM CIRCUIT

FIG. 3.9 – COAXIAL TRANSMISSION LINE
RUNING ABOVE THE GROUND

Stray capacitance also plays an important role in beam extraction, since it affects the ripple of the HVPS output voltage. This has been the object of another major modelling exercise, as covered in detail in chapter four. The ripple of the output voltage deteriorates the quality of the optics of the ion beam and ideally should be as low as possible, 5% maximum is specified for ITER (table 3.2). The RC filters at the output of the high voltage rectifiers indeed serve the purpose of smoothing the HVPS output voltage. In addition to the parameters of the filters, the relative phases of the HVPS inverters are a further factor affecting the ripple. In this respect, two distinct aspects have to be considered:

- *Sequence of commutation of the various stages.*
  Let us label the five stages of ITER HVPS as #1 (-1 MV to ground), #2 (-800 kV to ground), #3 (-600 kV to ground), #4 (-400 kV to ground) and #5 (-200 kV) and the three phases as *r*, *s* and *t*. The line-to-line voltage between phase *r* and phase *s* at the output of the NPC inverter of a generic stage #*i*, v_{i_rs}, is a periodic function of time with angular frequency $\omega_{INV}=2\cdot\pi\cdot(150\ Hz)$:

$$v_{i\_rs} = v_{i\_rs}\left(\omega_{INV}t + \vartheta_i\right) \qquad i = 1,2...5 \qquad (3.13)$$

Similarly, for the other two line-to line voltages of the three-phase system:

$$v_{i\_st} = v_{i\_st}\left(\omega_{INV}t + \frac{2}{3}\pi + \vartheta_i\right) \qquad i = 1,2...5 \qquad (3.14)$$

$$v_{i\_tr} = v_{i\_tr}\left(\omega_{INV}t - \frac{2}{3}\pi + \vartheta_i\right) \qquad i = 1,2...5 \qquad (3.15)$$

Each of the five HVPS stages is characterised by its own phase θ_i, *i*=1, 2, 3, 4, 5. If the switching delay angle between consecutive stages is θ_D, the phase of each stage takes one of the five values {*0, θ_D, 2·θ_D, 3·θ_D, 4·θ_D*}. By "switching sequence" is intended the exclusive association of each of the five stage phases, {*θ_1, θ_2, θ_3, θ_4. θ_5*}, to one of the five available values {*0, θ_D, 2·θ_D, 3·θ_D, 4·θ_D*}. Note

that the position $\theta_i=0$ sets stage #*i* as a reference for the phase of the other four stages. In a low voltage conversion system, the switching sequence makes little difference to the resulting ripple of the output voltage; it is the value of θ_D that matters. On the contrary, in a high voltage system with series connected modules each of these sits at a different voltage with respect to ground. Based on this observation, a qualitative recipe for the optimisation of the inverter switching sequence comes from a recent experience on JET neutral beam circuit with inverter-based HVPS [48].

- *The amplitude of the switching delay θ_D, in electrical degrees, between consecutive stages.*
  This is similar to the series connection of two six-pulse converters: by introducing a phase delay of 30° between the three-phase supplies to the two bridges, the resulting ripple has twelve pulses per period and its amplitude is minimised [49]. The ITER HVPS has five stages, therefore one might erroneously expect that the ripple be minimised when the phases are staggered by (60°)/5=12° (corresponding to the supposed period of the ripple divided by the number of series connected rectifier bridges). Though literature on HVDC and harmonics is abundant [e.g. 50,51,52,53], no instance has been found of optimisation of the inverter switching delay in presence of high voltage and stray capacitance.

3.3.2 Open issues
The modelling approach used in the past for neutral beam circuits and described in the previous paragraph would have strong limits in the context of ITER breakdown simulations:

- Travelling wave effects along transmission lines would not be predicted, because the distributed nature of the phenomena would not be taken into account. These effects could be important, e.g. in assessing voltage inversion and related risks for insulation materials [54]

- The full extent of the voltage rise of the conductors with respect to local ground would not be simulated, because of the assumption of constant voltage ground. Such an idealisation seems weak, in studying fast transients and at some distance from the injector grounding point. An example: a rating of 100 kV has been considered for the insulation of the return conductor of ITER NBI circuit. Will this be sufficient to avoid failures at the start of TL1? A further consideration: without a model of the ground impedance, it would problematic to evaluate the full impact of alternative earthing schemes. Instead a possible scenario might be worth analysing, in which the single earthing point is abandoned and the start of the transmission line grounded through some impedance.

- The extent of the power supply contribution to the peak breakdown current would be unknown, unless some estimate of the stray capacitance were performed and included in the model.

Additionally, the theory of low voltage converters and literature on HVDC ripple appear unable to provide indications on how to optimise HVPS inverter switching, from the standpoint of minimising the ripple of the dc high voltage.

In the next two chapters a novel approach is presented, capable of addressing some of the above issues. On the aspect of ground impedance, that constitutes the core of the work, a gradual process seemed appropriate and the first analyses shown refer to the standard hypothesis of ideal ground at constant voltage (chapter four). This also provides a term of comparison for the results shown later and obtained with an innovative ground impedance circuit (chapter five). Even so, it was thought the results of the ITER breakdown simulations with ground impedance would be received with scepticism, unless supported by more than inductance and capacitance calculations. A modelling activity, in parallel to the ITER one, has therefore been carried out for the neutral beam circuit of JET. Ground impedance effects have been included in the circuit model, experimental measurement taken on JET and compared against the prediction of the simulations, confirming the validity of the proposed scheme and supporting its use on ITER (chapter five).

4. FIRST MODELS FOR ITER NEUTRAL BEAM CIRCUIT

4.1 Ripple, beam extraction and fault conditions

During extraction of the beam, good optics requires that the ratio between acceleration voltage and ion beam current stay at a fixed value, known as "perveance match" condition. Any ripple of the acceleration voltage implies a deviation from perveance match and is therefore undesirable. In this respect, a filter of larger capacitance at the output of the HVPS is a favourable feature. Similarly, in case of sudden loss of HVPS load (for instance due to a fault in the ion source), before the inverters are switched off the output voltage will increase, at a rate limited only by the filter capacitance.
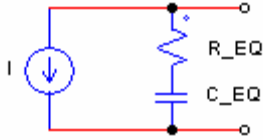
FIG. 4.1 – SIMPLIFIED CIRCUIT FOR THE LOSS OF HVPS LOAD

Let us analyse in greater detail the loss of load, in an attempt to find the relation between filter capacitance and rate of rise of the HVPS output voltage. The discussion in §3.2.4 about the dynamics of the HVPS current in the first few tens of microseconds following a breakdown, highlighted the large inertia to current changes represented by the isolation transformer leakage inductance. In first approximation, the HVPS can be represented as a current source, of amplitude equal to the value of the current at the instant of the loss of load. The five series connected filters are equivalent to a single RC circuit of resistance $R_{EQ}=5\cdot R_F$ and capacitance $C_{EQ}=C_F/5$, where R_F and C_F are the parameters of the filter for the individual stage. The simple model of fig. 4.1 results for the HVPS loss of load.

The time evolution of the voltage V_C across capacitance C_{EQ} is described by the following equation:

$$I = -C_{EQ}\frac{dv_C}{dt} \tag{4.1}$$

The worst case for the overvoltage is when the loss of load occurs with acceleration voltage and beam current at their rated values for Deuterium operation, -1 MV and 59 A respectively. The overvoltage is estimated neglecting the voltage drop across R_{EQ}, equal to 59A·(5·68Ω)=20kV. Once current and voltage rate of rise were fixed, eq. (4.1) could be used to determine C_{EQ}. It is generally accepted that to ensure integrity of the insulation, the voltage should not decrease by more than 10% below the rated value of -1 MV, over the 100 µs interval required to switch off the HVPS inverters. This condition corresponds to the following voltage rate of rise:

$$\frac{dv_C}{dt}\bigg|_{MIN} = -\frac{100}{100}\frac{kV}{\mu s} = -10^9\,V/s \tag{4.2}$$

Inserting the voltage rate of rise given by eq. (4.2) into eq. (4.1), the following minimum filter equivalent capacitance results:

$$C_{EQ}\big|_{MIN} = -\frac{I}{\dfrac{dv_C}{dt}\bigg|_{MIN}} = \frac{59}{10^9}\frac{A}{V/s} \cong 60nF \tag{4.3}$$

The capacitance required for the filter of each of the five HVPS stages is given by $C_F = 5\cdot C_{EQ}=300nF$. Although simplified, this analysis has illustrated the basic mechanism behind the overvoltage upon loss of HVPS and substantiated the value of filter capacitance introduced earlier (table 3.2).

A first set of circuit models and simulations, described in §4.2, concerns the ripple of the HVPS output voltage. The filter parameters of table 3.2 are used. The objective of the analyses is to investigate the inverter switching strategies that minimise the ripple of the HVPS output voltage, checking at the same time whether in absolute value it stays below the threshold of 5%. The issue has already been introduce qualitatively in §3.3.1, now the circuit models will be presented (§4.2.2) and the results of the simulations discussed thoroughly (§4.2.3).

The behaviour of the circuit in a load breakdown is another crucial aspect and filtering of the output voltage needs to be coordinated with load protection. In §4.3 a model of the ITER circuit is developed, along the following lines:

- Inclusion of stray capacitance

- Multi-cell model of the transmission line

- Ideal ground at constant voltage.

The required length of the transmission line cell is determined with an iterative process (§4.3.2), in which decreasing cell lengths are considered up to the point where further reductions do not affect the simulations. A critical review (§4.3.3) of the results follows and the exposed weakness of the model will lead to the enhancements presented in chapter five.

4.2 Analysis of the ripple of the HVPS output voltage

4.2.1 Development of a distributed circuit model

The structure of the ITER HVPS, with five series connected stages each delivering an output voltage of -200 kV, has been presented in §3.2.1. Subsequently the issues critical to circuit modelling of the HVPS has been reviewed (§3.3), having to do mainly with the isolation transformer stray capacitances and their distributed nature. The role of the latter aspect may be quantified by comparing the results obtained with different degrees of discretisation: let us consider initially a scheme where each winding of the isolation transformer is modelled by a single cell as shown in fig. 4.2.
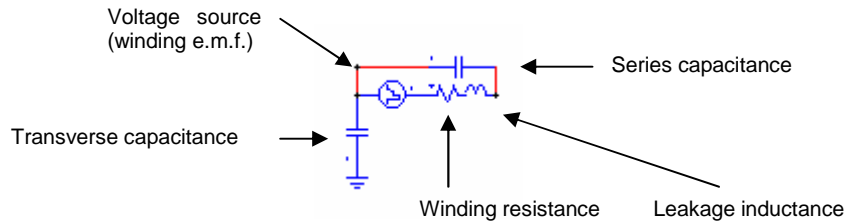
FIG. 4.2 – SINGLE CELL CIRCUIT MODEL FOR THE HIGH VOLTAGE WINDING OF A HVPS ISOLATION TRANSFORMER

The corresponding circuit model of the whole HVPS is shown in fig. 4.3. The following salient points should be noted:

- Only the high voltage side of the circuit is covered, including isolation transformer secondary windings, oil to gas bushings, diode rectifiers and load. The inverters are simulated through square waveform e.m.f.s.

- The high voltage transmission line is absent and the load is simulated by an ideal dc current source, an approach rather common in converter studies [49].

- Only one cell is used for each transformer winding.

The model of fig. 4.3 has been implemented in the circuit simulation software PSIM Version 6.0 [55], with the circuit parameters of table 3.2. PSIM uses a fixed time step and 1 μs has been adopted throughout ripple simulations, an adequate time step considering that the phenomena under investigation range from few kilohertz to few tens of kilohertz.

This preliminary study has the objective to determine the number of cells to be used in the distributed model of the isolation transformer secondary winding. In the simulations shown below, the number of cells is the only parameter that will be varied, checking the effects on the Fourier content of the simulated HVPS output voltage.

For the simulation to run, a phase θ_i must be assigned to the inverter of each HVPS stage. The index *i* takes the values *i*=1,2…5, where the stages are numbered from 1 (-1 MV to ground) to 5 (-200 kV to ground) in increasing order of voltage to ground. As far as the analysis of the winding number of cells is concerned, the following switching phases are used:

$$\begin{bmatrix} \theta_1 \\ \theta_4 \\ \theta_2 \\ \theta_5 \\ \theta_3 \end{bmatrix} = \begin{bmatrix} 0 \\ \pi/15 \\ 2\pi/15 \\ \pi/5 \\ 4\pi/15 \end{bmatrix} \qquad (4.4)$$
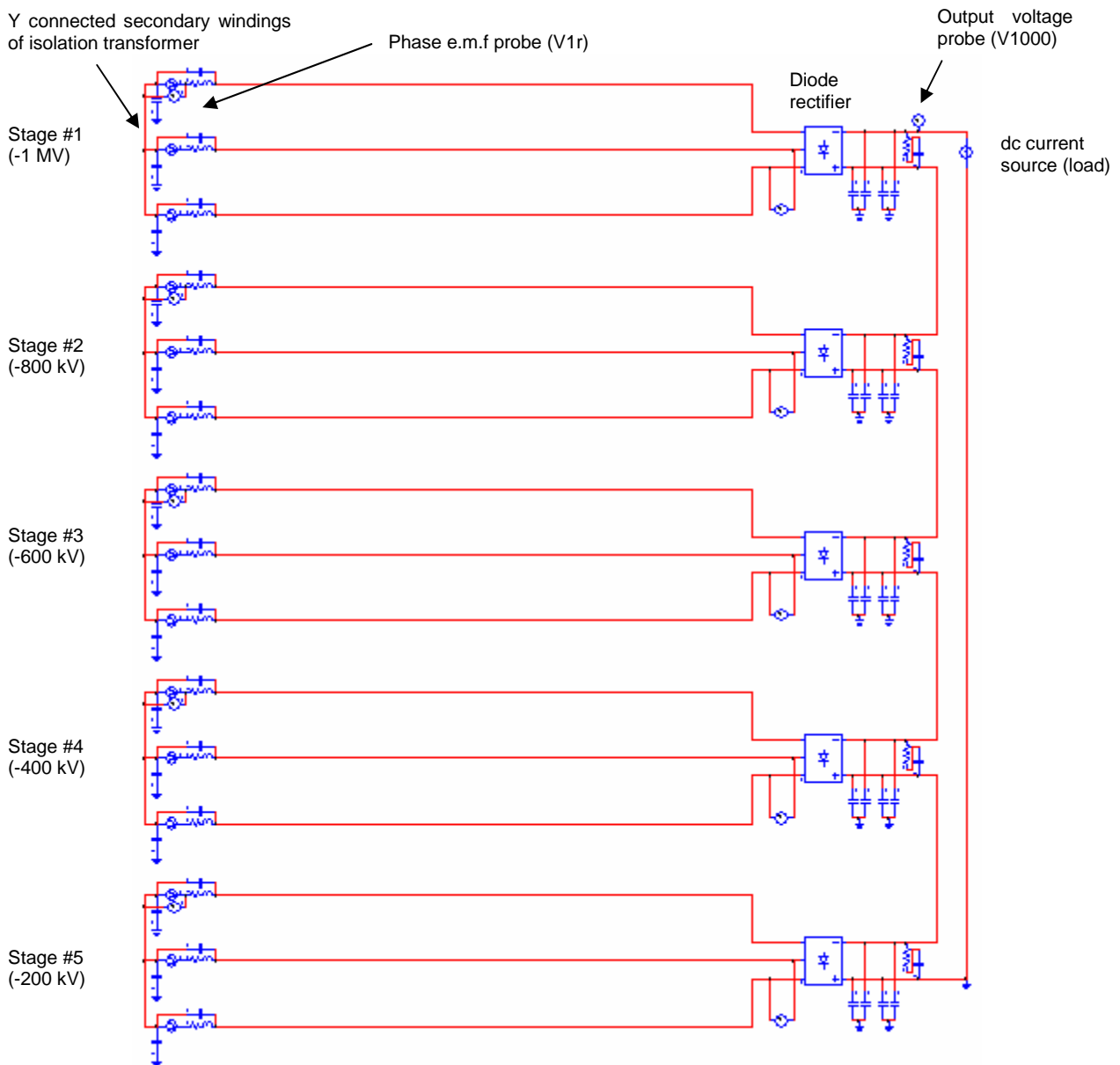
FIG. 4.3 – HVPS CIRCUIT MODEL WITH ONE CELL PER ISOLATION TRANSFORMER SECONDARY WINDING

These switching phases are characterised by $\pi/15$ (12°) delay between consecutive stages, as one would choose for a low voltage converter with five series connected units having six pulse ripple. The sequence of the stages in (4.4) is optimised according to the indications available in literature [48] and discussed in §3.3.1; further details are given in §4.2.2.

The simulated output voltage from the model of fig. 4.3 with the switching phases of (4.4) is shown in fig. 4.4 and the corresponding main Fourier components of the spectrum are listed in table 4.1.
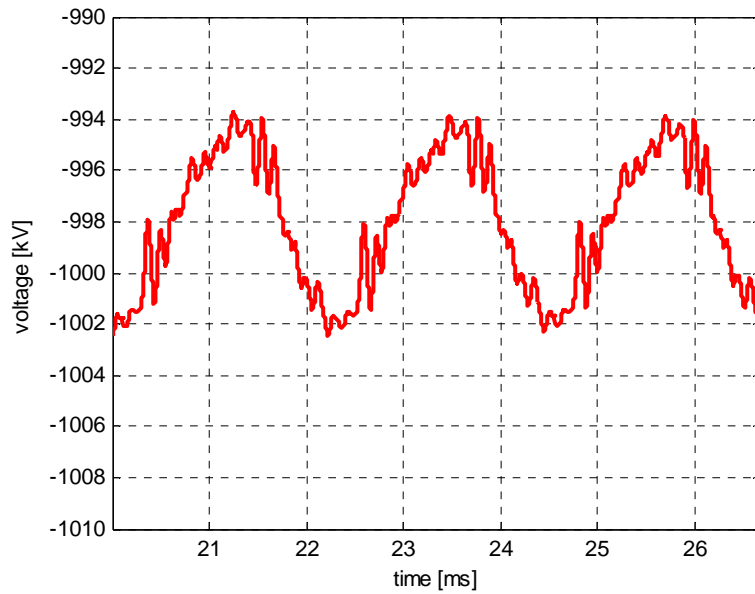
FIG. 4.4 – SIMULATED OUTPUT VOLTAGE OF THE HVPS WITH ONE CELL PER TRANSFORMER WINDING

TABLE 4.1: PARAMETERS OF THE HVPS OUTPUT VOLTAGE SIMULATED WITH SINGLE CELL WINDING

Parameter	Value
Minimum voltage	-1002 kV
Maximum voltage	-993.8 kV
Peak to peak ripple (% of dc component)	0.82%
Dc component	1000 kV
3rd harmonic (450 Hz) % of dc component	3.58 kV 0.359%
6th harmonic (900 Hz)	429 V
15th harmonic (2.25 kHz)	301 V
30th harmonic (4.5 kHz)	217 V
Inverter duty	85.5% On 14.5% Off

In fig. 4.4 a period of the inverter frequency (150 Hz) is displayed and the voltage waveform shows three pulses. This indicates that the third harmonic is the largest component of the ripple, as confirmed by the analytical detail of table 4.1. The circumstance is somewhat surprising: for a low voltage converter, the main component of the ripple is expected at a frequency given by the fundamental inverter frequency (150 Hz), multiplied by six (for six pulse conversion) and further multiplied by five (for the number of equally phase-displaced stages). Such a frequency corresponds to 4.5 kHz in the case of ITER HVPS. To confirm that the peculiar results of fig. 4.4 have to be attributed to stray capacitance at high voltage, the simulation has been repeated removing from the model all transverse capacitances. This new simulation confirms (fig. 4.5 and table 4.2) that in absence of stray capacitance the ripple is dominated by the thirty pulse harmonic component at 4.5 kHz. Note also that, the same linear scale for the voltage having been used in the two cases, a comparison between the two waveforms gives a visual appreciation of the importance of the ripple

due to transverse stray capacitance: the peak-to-peak ripple of fig. 4.4 is more than ten times larger than that of fig. 4.5.
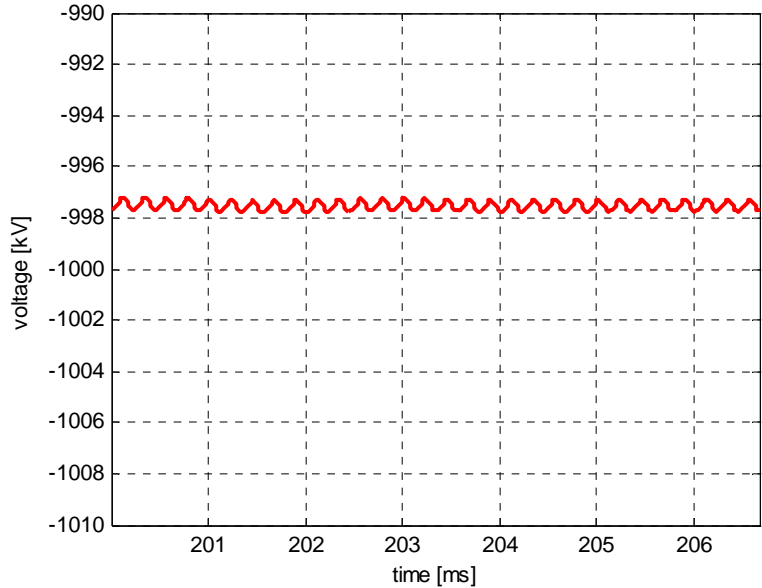

FIG. 4.5 – HVPS OUTPUT VOLTAGE WITH ONE CELL PER TRANSFORMER WINDING AND NO TRANSVERSE CAPACITANCE

TABLE 4.2: HVPS OUTPUT VOLTAGE WITH SINGLE CELL WINDING AND NO TRANSVERSE CAPACITANCE

Parameter	Value
Minimum voltage	-997.8 kV
Maximum voltage	-997.2 kV
Peak to peak ripple (% of dc component)	0.06%
Dc component	997.5 kV
3rd harmonic (450 Hz)	24.9 V
6th harmonic (900 Hz)	3.90 V
15th harmonic (2.25 kHz)	1.25 V
30th harmonic (4.5 kHz)	239 V
Inverter duty	85.5% On 14.5% Off

A final comment to the results of fig. 4.4 and fig. 4.5 concerns the waveform of the voltage sources representative of the winding electromotive forces. These have the shape displayed in fig. 4.6 for the e.m.f. of phase *r* of the isolation transformer of stage #1. The stepped waveform shown is the result of 85.5% ON / 14.5% OFF modulation of the phase voltage performed by the NPC inverter on the primary side of the isolation transformer. The other windings have an e.m.f. with identical shape, but are phase shifted according to the phase and to the stage they belong to. The figure of 85.5% for the ON time proved the one that guarantees a dc component of the output voltage close to -1000 kV in most situations. Below, while circuit models with different number of cells for the transformer winding are compared; the ON modulation will stay at the value of 85.5%, to ensure that the supply voltage has the same harmonic spectrum in all cases.
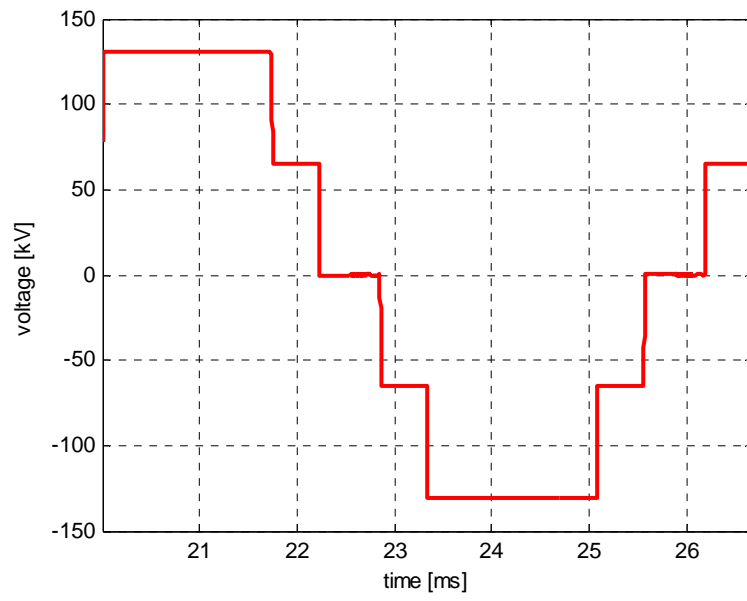
FIG. 4.6 – SAMPLE PHASE E.M.F OF TRANSFORMER WINDING USED IN THE SIMULATIONS OF FIG. 4.3 AND FIG. 4.4

At this point transverse capacitances are re-instated in the model and the number of cells per transformer winding is increased to two. The simulated output voltage of fig. 4.7 results, with the parameters listed in table 4.3.
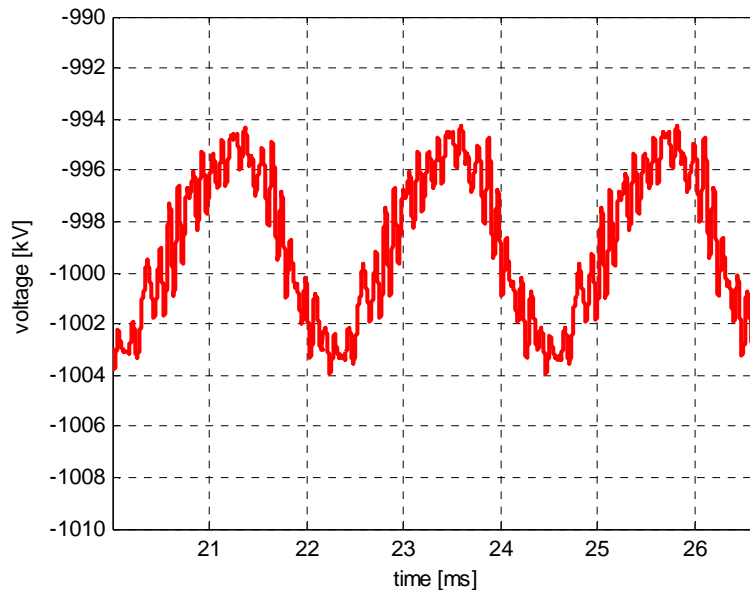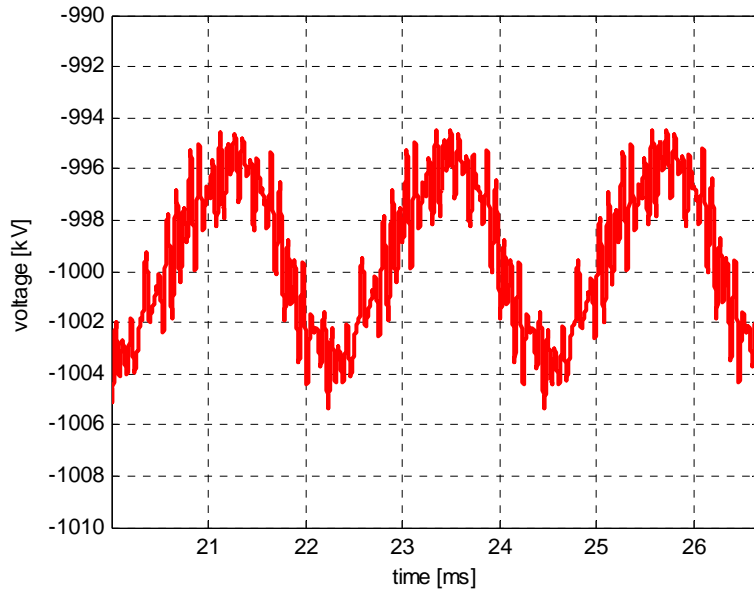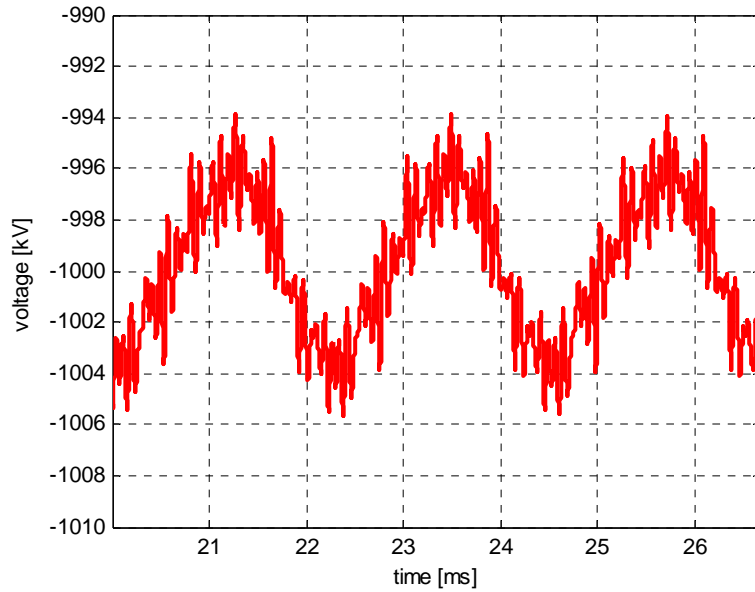

FIG. 4.7 – SIMULATED OUTPUT VOLTAGE OF THE HVPS WITH TWO CELLS PER TRANSFORMER WINDING

TABLE 4.3: HVPS OUTPUT VOLTAGE WITH TWO CELLS PER WINDING

Parameter	Value
Minimum voltage	-1004 kV
Maximum voltage	-994.2 kV
Peak to peak ripple (% of dc component)	0.98%
Dc component	998.9 kV
3rd harmonic (450 Hz) % of dc component	3.85 kV 0.385%
6th harmonic (900 Hz)	448 V
15th harmonic (2.25 kHz)	308 V
30th harmonic (4.5 kHz)	193 V
Inverter duty	85.5% On 14.5% Off

Comparing table 4.1 with table 4.3, it emerges that the third harmonic component of the ripple has increased in relative terms by about 7% and the sixth harmonic component by about 5%. Visually a change of shape of the output voltage appears clear, with a dirtier waveform characterised by larger oscillations at higher frequency. The third harmonic remains by far the largest component of the ripple. In the light of this, the following criterion is adopted to determine when to halt the refinement of the transformer winding model:

With respect to the previous step, a change of amplitude of the third harmonic by 1% or less.

The criterion presented above deserves some comment. The reason for basing the choice on the third harmonic has already been mentioned: it is the largest contributor to the ripple of the output voltage. Alternatively, the peak to peak value of the ripple itself could have been chosen. The third harmonic has been preferred because less sensitive to variations of modulation. When the inverter modulation changes,

the harmonic mix of the winding e.m.f changes and, depending for instance on the filter parameters, the resulting peak to peak ripple also changes. The threshold of 1.5% is the result of a compromise: in principle the lower the tolerance the more accurate the final model, however one should also consider the practicality of managing a circuit with hundreds of elements.

Having exposed the reasons for a further refinement of the model, three cells per winding have been simulated next (fig. 4.8 and table 4.4). With respect to the two cell model, the amplitude of the third harmonic has decreased by about 2%, failing the "stop" criterion set above.
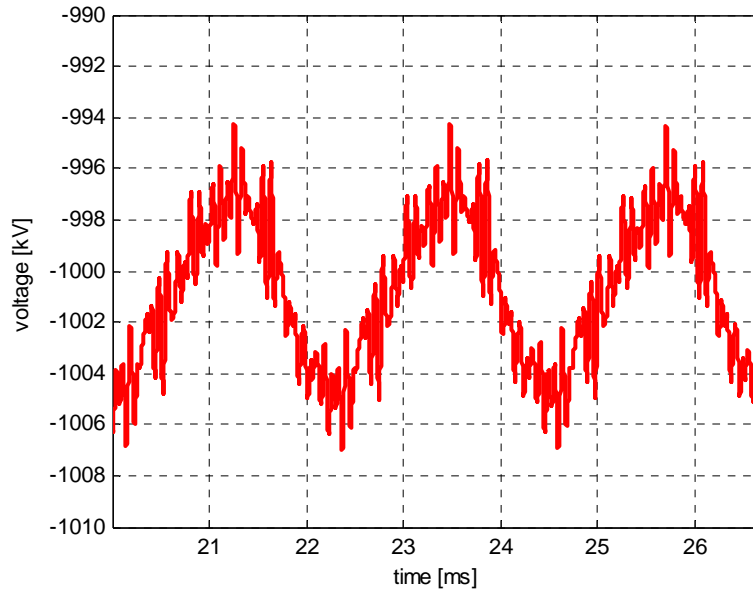

FIG. 4.8 – SIMULATED OUTPUT VOLTAGE OF THE HVPS WITH THREE CELLS PER TRANSFORMER WINDING

TABLE 4.4: HVPS OUTPUT VOLTAGE WITH THREE CELLS PER WINDING

Parameter	Value
Minimum voltage	-1005 kV
Maximum voltage	-994.5 kV
Peak to peak ripple (% of dc component)	1.05%
Dc component	999.4 kV
3rd harmonic (450 Hz) % of dc component	3.76 kV / 0.376%
6th harmonic (900 Hz)	431 V
15th harmonic (2.25 kHz)	321 V
30th harmonic (4.5 kHz)	190 V
Inverter duty	85.5% On / 14.5% Off

With four cells per winding, the simulation gives the HVPS output voltage of fig. 4.9 and table 4.5. The third harmonic has gone down by 3% with respect to the three cell analysis.

FIG. 4.9 – SIMULATED OUTPUT VOLTAGE OF THE HVPS WITH FOUR CELLS PER TRANSFORMER WINDING

TABLE 4.5: HVPS OUTPUT VOLTAGE WITH FOUR CELLS PER WINDING

Parameter	Value
Minimum voltage	-1006 kV
Maximum voltage	-993.9 kV
Peak to peak ripple (% of dc component)	1.21%
Dc component	999.8 kV
3rd harmonic (450 Hz) % of dc component	3.65 kV 0.365%
6th harmonic (900 Hz)	405 V
15th harmonic (2.25 kHz)	328 V
30th harmonic (4.5 kHz)	190 V
Inverter duty	85.5% On 14.5% Off

In the following refinement five cells per winding have been used, as reported in fig. 4.10 and table 4.6. The amplitude of the third harmonic component is up by about 3% as compared to the four cell simulation.
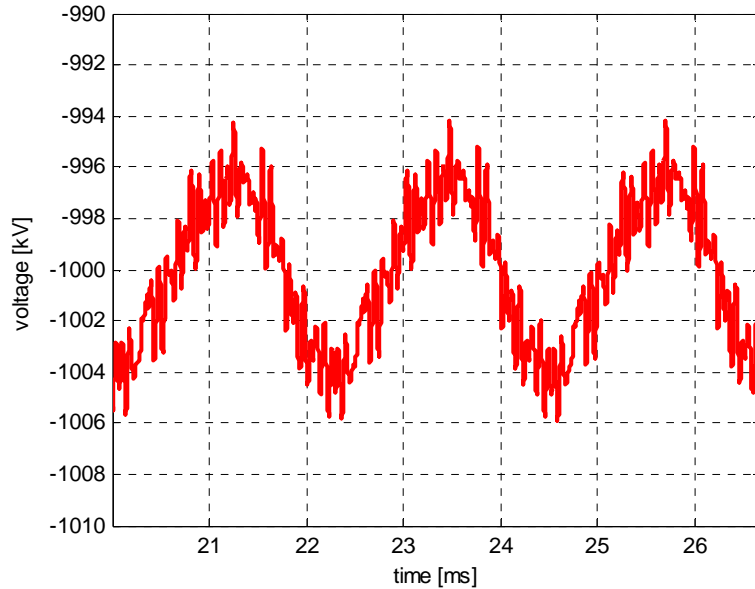

FIG. 4.10 – SIMULATED OUTPUT VOLTAGE OF THE HVPS WITH FIVE CELLS PER TRANSFORMER WINDING

TABLE 4.6: HVPS OUTPUT VOLTAGE WITH FIVE CELLS PER WINDING

Parameter	Value
Minimum voltage	-1007 kV
Maximum voltage	-994.2 kV
Peak to peak ripple (% of dc component)	1.28%
Dc component	1001 kV
3rd harmonic (450 Hz) % of dc component	3.76 kV 0.376%
6th harmonic (900 Hz)	444 V
15th harmonic (2.25 kHz)	335 V
30th harmonic (4.5 kHz)	192 V
Inverter duty	85.5% On 14.5% Off

The next step takes the number of cells per winding to seven, with an increase of two cells. This is because, as the number of cell increases, the increment of one cell at a time becomes less significant in relative terms. The HVPS output voltage of the seven cell simulation is illustrated by fig. 4.11 and table 4.7. The change in the third harmonic component with respect to the previous model is 1%, meeting the "stop" criterion set above. The final circuit model of the HVPS with seven cells per winding is shown in fig. 4.12 and as such will be employed in the analysis of the inverter sequence for ripple minimisation treated below (§4.2.2).

FIG. 4.11 – SIMULATED OUTPUT VOLTAGE OF THE HVPS WITH SEVEN CELLS PER TRANSFORMER WINDING

TABLE 4.7: HVPS OUTPUT VOLTAGE WITH SEVEN CELLS PER WINDING

Parameter	Value
Minimum voltage	-1006 kV
Maximum voltage	-994.2 kV
Peak to peak ripple (% of dc component)	1.18%
Dc component	1000 kV
3rd harmonic (450 Hz) % of dc component	3.73 kV 0.373%
6th harmonic (900 Hz)	421 V
15th harmonic (2.25 kHz)	331 V
30th harmonic (4.5 kHz)	183 V
Inverter duty	85.5% On 14.5% Off
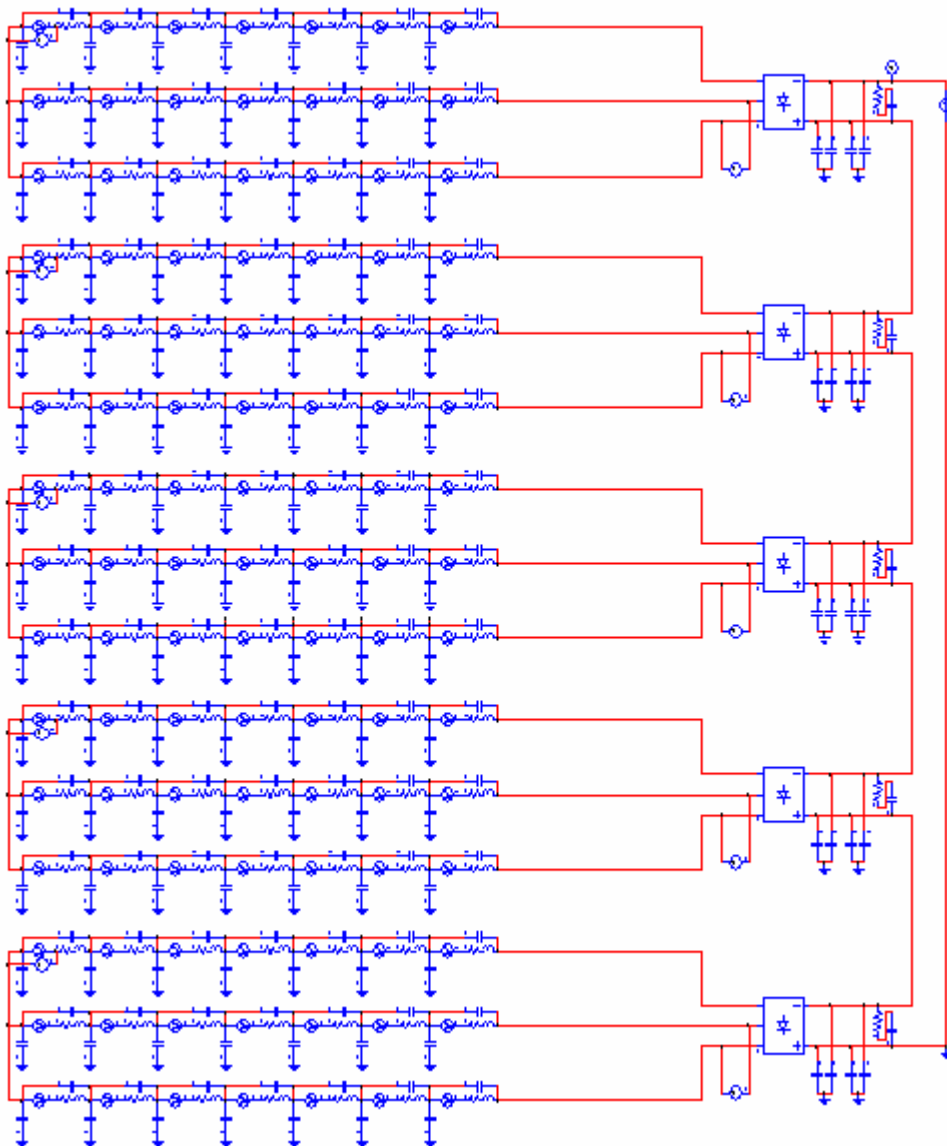
FIG. 4.12 – HVPS CIRCUIT MODEL WITH SEVEN CELLS PER ISOLATION TRANSFORMER SECONDARY WINDING

4.2.2 Optimisation of the inverter switching delay and comparison with converter theory

A working model, characterised by seven cells per transformer winding, has been established above (§4.2.1) for the ripple studies and will be employed in the optimisation of the inverter switching phases. In this respect, the basic concepts have been introduced in §3.3.1 and need to be discussed now at a greater length.

The HVPS output voltage is the result of the series connection of the output voltage of five stages. The output voltage of each stage is controlled by the voltage waveform supplied by the three-phase inverter to the isolation transformer. The waveform of the three-phase inverter is determined by a number of design features:

- The NPC architecture [28] of the three-phase inverter. This implies that the waveform of the phase voltage is square and controlled with a PWM technique. The resulting line-to-line voltage has a stepped shape like in fig. 3.3

- The frequency of the inverter is 150 Hz

- The high voltage diode rectifiers have the structure of the Graetz bridge, outputting a rectified output with six pulses.

In general, the modulation of the ON time of the inverter is dictated by the requested amplitude of the HVPS output voltage. The only degrees of freedom available to minimise the ripple of the HVPS are represented by the relative phases of the inverters of the five stages. In formulas, the three-phase system of voltages supplying the high voltage diode rectifier of a generic stage i is composed of periodic functions of time, with angular frequency $\omega_{INV}=2\pi(150\ Hz)$:

$$V_{i\_rs} = V_{i\_rs}\left(\omega_{INV}t + \theta_i\right)$$

$$V_{i\_st} = V_{i\_st}\left(\omega_{INV}t + \frac{2}{3}\pi + \theta_i\right) \tag{4.5}$$

$$V_{i\_tr} = V_{i\_tr}\left(\omega_{INV}t - \frac{2}{3}\pi + \theta_i\right)$$

where the matter object of optimisation is the relative angular displacement θ_i, i=1,2…5. Assuming, as it appears reasonable, that θ_i be in reality multiple of a given switching delay angle θ_D, each θ_i takes one of the values found in the following vector:

$$\Theta_D \equiv \begin{bmatrix} 0 \\ \theta_D \\ 2\theta_D \\ 3\theta_D \\ 4\theta_D \end{bmatrix} \tag{4.6}$$

The inverter switching pattern is fully defined once:

- The *switching sequence* has been chosen, meaning the five phases θ_1, θ_2, θ_3, θ_4, θ_5 have been arranged into a vector Θ_P associating them to the five switching delays in Θ_D. As an example, the sequence of formula (4.4) is expressed with the position:

$$\Theta_P = \begin{bmatrix} \theta_1 \\ \theta_4 \\ \theta_2 \\ \theta_5 \\ \theta_3 \end{bmatrix} \tag{4.7}$$

- A value for θ_D has been selected. In a low voltage conversion system made of n series connected modules, each characterised by m-pulse ripple, it is common practice to choose $\theta_D=2\pi/(m \cdot n)$. In the case of ITER HVPS with five diode rectifiers of the six-pulse type, this position would imply $\theta_D=2\pi/(6 \cdot 5)=\pi/15\ (12°)$.

Let us discuss first the role of the switching sequence. The results of Ganuza et al. [48] for a high voltage power supply with structure similar to ITER'S HVPS suggest that the switching sequence does affect the ripple of the output voltage. This will be checked below with simulations of ITER HVPS, where different switching sequences are compared, all other parameters being equal. In the simplest sequence one might conceive, the stages follow in order of voltage:

$$\Theta_{PS} = \begin{bmatrix} \theta_1 \\ \theta_2 \\ \theta_3 \\ \theta_4 \\ \theta_5 \end{bmatrix} \tag{4.8}$$

For the sake of this analysis, a switching delay of $\pi/15\ (12°)$ is used, therefore:

$$\Theta_{PS} = \begin{bmatrix} \theta_1 \\ \theta_2 \\ \theta_3 \\ \theta_4 \\ \theta_5 \end{bmatrix} = \begin{bmatrix} 0 \\ \pi/15 \\ 2\pi/15 \\ \pi/5 \\ 4\pi/15 \end{bmatrix} \qquad (4.9)$$

The circuit model with seven cells per transformer winding is employed, as developed in the previous paragraph (fig. 4.11). With the non-optimised switching phases (4.9), the simulated output voltage of fig. 4.13 and table 4.8 results.

A comparison between table 4.8 and table 4.9 shows that the non-optimised sequence (4.9) increases by a fair amount, in relative terms, the third harmonic component of the ripple. The role of the switching sequence is explained qualitatively by Ganuza et al. [48] in the following terms. The preliminary consideration is that in a high voltage system with multiple and series connected modules, each module is at a different voltage with respect to ground. Because of this, when a commutation is performed e.g. in the inverter of a module close to ground potential, the capacitive currents drained are different from those of a module close to the high voltage potential. The switching sequence that minimises the ripple is the one that, as much as possible, distributes in a uniform fashion high and low voltage commutations over a period of the fundamental frequency. In this respect, the commutation of the stages in order of voltage as in formula 4.9 is the worst possible choice – and indeed the corresponding simulation gave the highest ripple.
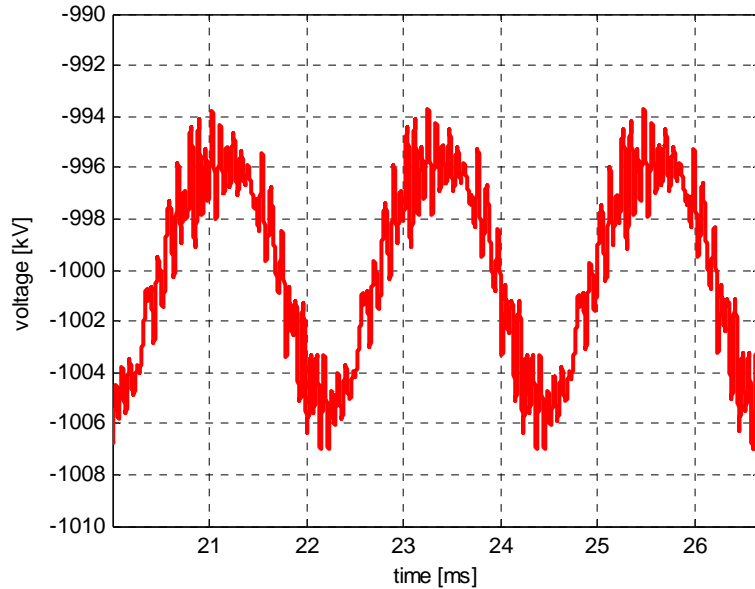
FIG. 4.13 – SIMULATED OUTPUT VOLTAGE OF THE HVPS WITH NON OPTIMISED SWITCHING SEQUENCE AND 12° DELAY

TABLE 4.8: HVPS OUTPUT VOLTAGE WITH NON OPTIMISED SWITCHING SEQUENCE AND 12° DELAY

Parameter	Value
Minimum voltage	-1007 kV
Maximum voltage	-993.7 kV
Peak to peak ripple (% of dc component)	1.33%
Dc component	999.9 kV
3rd harmonic (450 Hz) % of dc component	4.82 kV 0.482%
6th harmonic (900 Hz)	421 V
15th harmonic (2.25 kHz)	331 V
30th harmonic (4.5 kHz)	183 V
Inverter duty	85.5% On 14.5% Off

As far as the switching delay is concerned, in a low voltage conversion system the baseline position would be to adopt a delay of $\pi/15$ (12°). This value has already made its way into some ITER design studies.

Here an alternative approach is proposed, with a switching delay of $2\pi/15$ (24°). This is based on the simple consideration that, due to the combination of high voltage and stray capacitance, the main ripple of ITER HVPS has three rather than six pulses. A numerical simulation has been performed to check the effect of the value of $2\pi/15$ (24°) for the switching delay; the same switching sequence has been kept as in (4.7) and the following switching phases result:

$$\Theta_{PO} = \begin{bmatrix} \theta_1 \\ \theta_4 \\ \theta_2 \\ \theta_5 \\ \theta_3 \end{bmatrix} = \begin{bmatrix} 0 \\ 2\pi/15 \\ 4\pi/15 \\ 2\pi/5 \\ 8\pi/15 \end{bmatrix} \tag{4.10}$$

The result of the simulation is shown in fig. 4.14; the detail of the Fourier components can be found in table 4.9. Indeed, the simulation proves that a switching delay tuned on the third harmonic reduces significantly the overall peak to peak ripple (almost halved). The reduction of the third harmonic component is even more dramatic, down to about one third of the value in table 4.7. On the other hand, other harmonics have increased, e.g. the sixth. This is because the new phases are no longer optimum from the point of view of the sixth harmonic. The circumstance can be appreciated if the phases (4.10) are rewritten highlighting integer multiples of $\pi/3$ (60°):

$$\begin{bmatrix} 0 \\ 2\pi/15 \\ 4\pi/15 \\ 2\pi/5 \\ 8\pi/15 \end{bmatrix} = \begin{bmatrix} 0 \\ 2\pi/15 \\ 4\pi/15 \\ \pi/15 + \pi/3 \\ \pi/5 + \pi/3 \end{bmatrix} \tag{4.11}$$

To the sixth harmonic component of the ripple, having angular frequency (6·ωt) and periodicity $\pi/3$, the sequence of commutation of the stages (4.10) is equivalent to a new sequence Θ_{P6}, given by (4.11) where integer multiples of $\pi/3$ (60°) have been disregarded:

$$\Theta_{P6} = \begin{bmatrix} \theta_1 \\ \theta_5 \\ \theta_4 \\ \theta_3 \\ \theta_2 \end{bmatrix} = \begin{bmatrix} 0 \\ \pi/15 \\ 2\pi/15 \\ \pi/5 \\ 4\pi/15 \end{bmatrix} \tag{4.12}$$

In the sequence of sixth harmonic (4.12), the stages follow in order of voltage, a situation far from the optimum. However, because the dominant harmonic is the third, the overall effect of phases (4.10) is a consistent reduction of the ripple.
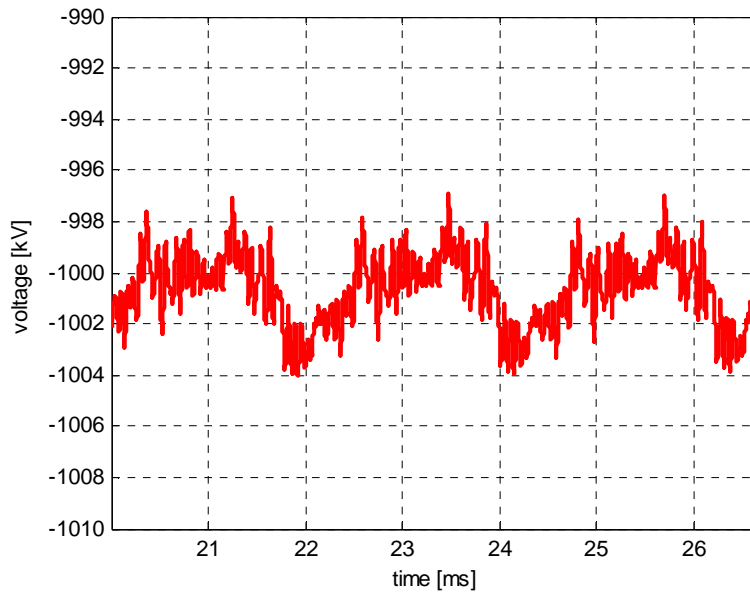

FIG. 4.14 – SIMULATED OUTPUT VOLTAGE OF THE HVPS WITH OPTIMISED SWITCHING SEQUENCE AND 24° DELAY

TABLE 4.9: HVPS OUTPUT VOLTAGE WITH OPTIMISED SWITCHING SEQUENCE AND 24° DELAY

Parameter	Value
Minimum voltage	-1004 kV
Maximum voltage	-996.9 kV
Peak to peak ripple (% of dc component)	0.71%
Dc component	1001 kV
3rd harmonic (450 Hz) % of dc component	1.35 kV 0.135%
6th harmonic (900 Hz)	494 V
15th harmonic (2.25 kHz)	771 V
30th harmonic (4.5 kHz)	182 V
Inverter duty	85.5% On 14.5% Off

4.2.3 Some considerations on ripple simulations

The circuit model developed above for the ripple of the HVPS output voltage and its use in optimising the inverter switching delay has shown amplitudes of the ripple well below the specified 5% limit. One might therefore question the practical value of the results presented above and the opportunity to devote large efforts to an aspect that is minor from the qualitative point of view.
The answer is threefold:
1) The methodology has a general validity that goes beyond the present case of ITER HVPS

2) The performance of ITER injector benefits from lower ripple even if this is already below the maximum tolerable limit. Lower ripple implies better optics, which in turn means e.g. lower losses on the mechanical components along the beam line.

3) The absolute values of the ripple illustrated above depend critically on one circuit parameter: the stray capacitance of the HVPS isolation transformer. This parameter has been assessed making a reasonable estimate, as illustrated in §3.2.1; however such a machine has never built and not even designed. Therefore, stepping into the territory of unknown technology, surprises are possible.

Let us place on a quantitative footing the observation under point 3). A rudimental parametric analysis is performed, repeating the simulation for optimised switching sequence and $2\pi/15$ (24°) delay (fig. 4.14) with doubled stray capacitance of the transformer windings.
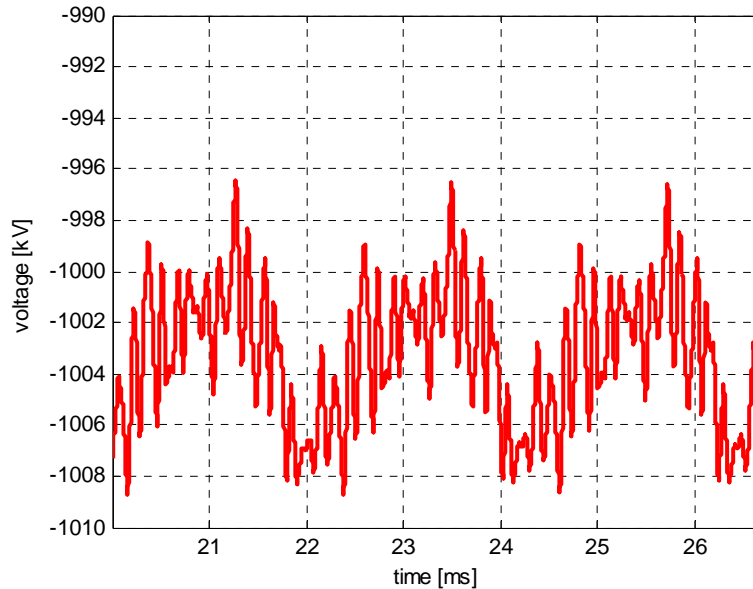
FIG. 4.15 – SIMULATED HVPS OUTPUT VOLTAGE (24° DELAY) WITH DOUBLED TRANSFORMER CAPACITANCE

The resulting peak to peak ripple is 12.6 kV (fig. 4.15), almost doubled with respect to fig. 4.14.
This result emphasises the value of developing analysis tools; the circuit parameters and the simulations may be refined in the years to come, once more is known about the actual technology and design of the HVPS components.

4.3 Simulation of load breakdown

The breakdown of the accelerator is a demanding condition, against which performance of the NBI high voltage circuit must be checked. Commonly adopted criteria to measure the severity of a breakdown include the energy dissipated into the fault (arc) and the peak fault current, as illustrated by Owren et al. [19]. Their work on a breakdown test stand with variable stored energy showed that, when fault energy and peak current were below some thresholds found experimentally, neither damage to the accelerator nor deterioration of its voltage holding capability would occur.
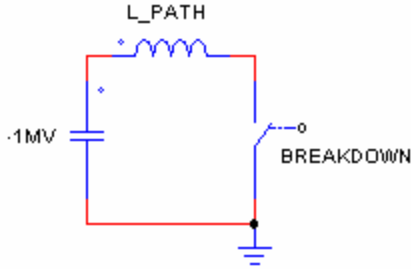
FIG. 4.16 –SIMPLIFIED CIRCUIT DIAGRAM FOR ESTIMATING THE PEAK FAULT CURRENT INSIDE THE INJECTOR

Early ITER design reports reflect this view, where limits of 10 J and 3 kA respectively were prescribed for breakdown energy and peak current respectively [42]. More recently, the value of specifying absolute limits for energy and current has been questioned, as far as the design of the injector power supply system is concerned [43]. Bigi et al. noted that, although for ITER NBI circuit (chapter three) core snubbers are foreseen along the high voltage transmission line, no protection device can be installed inside injector and -1 MV bushing. The capacitive stored energy of those is not insignificant and the only impedances limiting its discharge are the inductance associated to the current path (of the order of the metre) and the impedance of the arc. Literature is of little help in associating a voltage-current characteristic to the breakdown of the NBI accelerator, because no publication covers arcs between metallic electrodes in vacuum, on lengths of the order of tens of centimetres (the SINGAP main acceleration gap is about 30 cm long). An approximation often used consists in assuming for the arc a constant voltage drop of 100V. However, if one intends to estimate the order of magnitude of the peak fault current associated to the stored energy inside bushing and accelerator, the arc can be treated as a short circuit, leading to the simplified scheme of fig. 4.16.

In fig. 4.16, C_{LOAD} is the equivalent capacitance of the injector (referred to -1 MV potential) and L_{PATH} the stray inductance associated to the path of the fault current inside the injector. The difficulty of assessing the equivalent circuit parameters, even in presence of a design of the accelerator, appears clear. C_{LOAD} is anticipated to be of the order of the nanofarad (see table … below), whereas L_{PATH} should fall in the range of few hundreds nanohenries – let us assume 400 nH, for the sake of a calculation. The peak breakdown current I_{PEAK} is given by the initial voltage V_0 at which capacitor C_{LOAD} is charged, divided by the impedance of the LC circuit:

$$I_{PEAK} = \frac{V_0}{\sqrt{\dfrac{L_{PATH}}{C_{LOAD}}}} = \frac{1MV}{\sqrt{\dfrac{400nH}{1nF}}} = \frac{1MV}{20\Omega} = 50kA \qquad (4.13)$$

The associated frequency of oscillation f_{BDOWN} can be computed as:

$$f_{BDOWN} = \frac{1}{2\pi}\frac{1}{\sqrt{L_{PATH}C_{LOAD}}} = \frac{1}{2\pi}\frac{1}{\sqrt{400nH \cdot 1nF}} = 8MHz \qquad (4.14)$$

Estimate (4.13) of the peak fault current in the accelerator is an order of magnitude greater that the 3 kA limit quoted above. Bigi et al. insist that it makes little sense to specify protections that keep the power supply contribution to the fault significantly below the anticipated peak due to the injector capacitance. In actual fact, the true amplitude of the peak breakdown current in a real injector is unknown, because the measurement is problematic on an operating plant. A current transducer of large bandwidth would have to be installed inside the injector! The conclusion drawn by Bigi et al. is that the protection devices should be specified and designed with the aim of limiting the contribution to the fault from the power supply system, acknowledging that a fast breakdown dynamics exist within the injector, related to locally stored energy and beyond any control.

This introduction has given some background to the scope of the breakdown modelling presented below. The main objective here is to develop tools of analysis for the behaviour of the power supply circuit during a

grid breakdown, having as main application the investigation of different options at system level, with particular reference to:

- Nature, parameters and position in the circuit of the protection devices

- Grounding of the system.

4.3.1 Modelling issues

The circuit model for the breakdown used in this chapter is developed under the conventional idealisation of ground at constant voltage. The various items of plant reviewed in chapter 3 are included with their associated stray capacitance, whose important role has been stressed above on several occasions. Of the HVPS, only the output filters and the diode rectifiers are present. The simulations presented here limit their scope to the first few microseconds after the breakdown, a time over which the discharge of the output filters is small. This simplification makes the circuit purely passive and reduces the number of elements, an important fact also in the light of the 1 ns time step deemed necessary for breakdown simulations.

In addition to the components reviewed in chapter three, the circuit model of the breakdown will include SINGAP injector and bushing. These will be modelled with a simple network of capacitors and inductors shown in fig. 4.17. The corresponding circuit parameters are listed in table 4.10 [56].
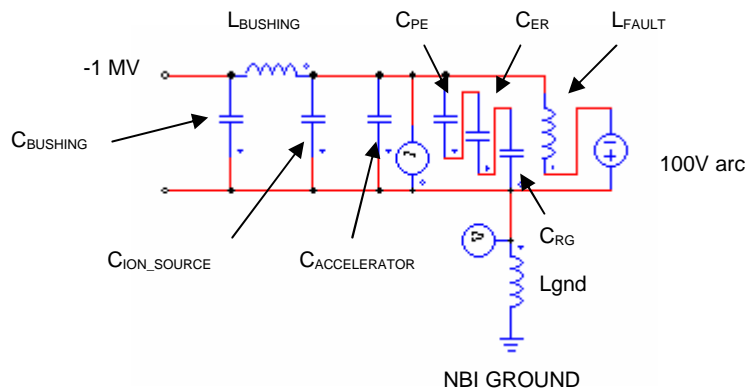
FIG. 4.17 – EQUIVALENT CIRCUIT MODEL FOR SINGAP INJECTOR AND BUSHING

TABLE 4.10: CIRCUIT PARAMETERS FOR SINGAP INJECTOR AND BUSHING

Parameter	Value
Bushing capacitance to ground ($C_{BUSHING}$)	576 pF
Bushing inductance ($L_{BUSHING}$)	250 nH
Ion source capacitance to ground (C_{ION_SOURCE})	676 pF
Accelerator cap. to ground ($C_{ACCELERATOR}$)	426 pF
Mutual capacitance between plasma grid and extraction grid (C_{PE})	17770 pF
Mutual capacitance between extraction grid and pre-acceleration grid (C_{ER})	2660 pF
Mutual cap. between pre-acceleration grid and post-acceleration grid (C_{RG})	152 pF
Inductance of fault current path (L_{FAULT})	300 nH
Inductance of grounding path (L_{GND})	1 μH

The structure of the model is shown in fig. 4.18, where blocks have replaced the three sections of the transmission line. The TL constitutes the main open modelling issue at this point. A distributed model of the transmission line is certainly necessary, as previously discussed (§3.3) and the level of discretisation (i.e. the length of the cell) is to be determined next.
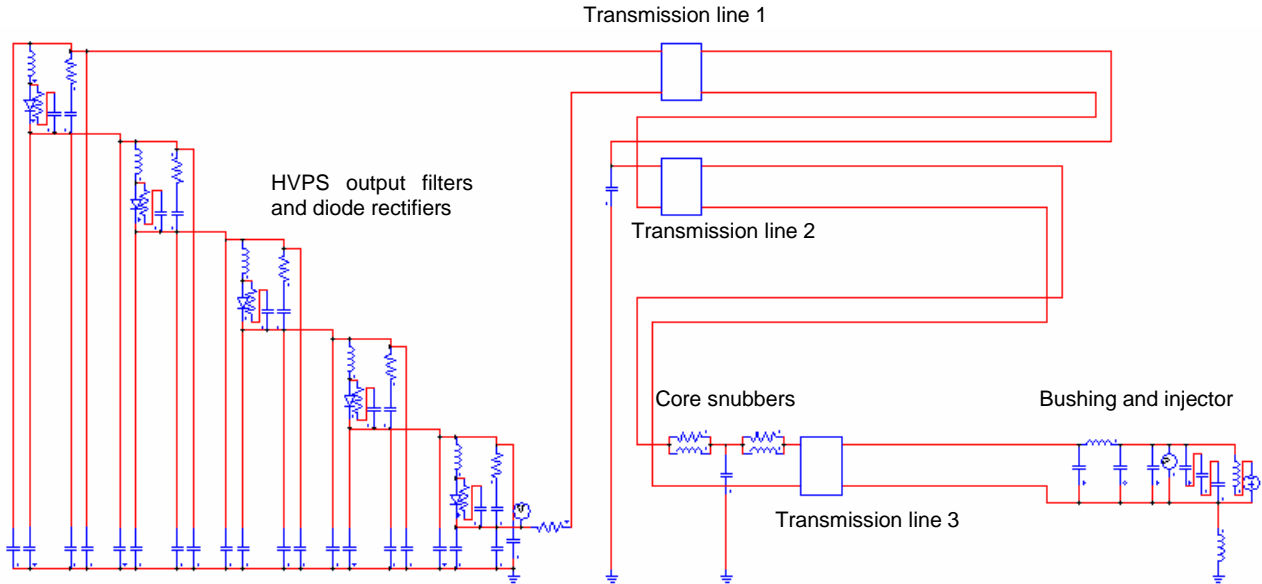

FIG. 4.18 – FIRST CIRCUIT MODEL FOR THE BREAKDOWN SIMULATIONS

4.3.2 Length of the transmission line cell

Indications coming from the literature [39] and the preliminary assessment carried out above with formula (4.14) have set close to 10 MHz the estimated bandwidth of the breakdown transient voltages and currents. This frequency corresponds to a length of 30 m and modelisation of the transmission line should ensure that over such distance several cells are comprised.

To investigate the effects of different lengths of the transmission line cell, from the complete breakdown circuit of fig. 4.18 a reduced model has been extracted, including only TL3, bushing and accelerator. At the start of the transmission line, inner and outer conductor are connected by a resistance equal to the transmission line characteristic impedance Z_{TL3} (see table 3.5):

$$Z_{TL3} = \sqrt{\frac{0.28}{39} \frac{\mu H / m}{pF / m}} = 85.8\Omega \qquad\qquad (4.15)$$

A first version of this simplified model, with three cells over the 15m length of TL3, is shown in fig. 4.19. The length of each cell is 5 m, reasonably below the figure of 30 m discussed above. The intention is to run breakdown simulations in a purely passive fashion, where at the initial time all capacitances are charged at the potential of -1 MV. The waveforms of the arc current (current recorded through the inductance of the arc short circuiting the accelerator, *Lfault* of fig. 4.19) obtained for decreasing cell lengths will be compared, up to the point when a pre-established criterion is met for stopping the iterative process. In this case, the variable used in the decision is the frequency of the largest harmonic component of the arc current. The criterion employed is the following: the cell length is decreased in subsequent steps, until a further reduction does not cause the frequency of the largest harmonic component to increase. The choice of the breakdown current as the quantity to base the criterion on is the most natural, since it characterises well the fast oscillations of the resonant LC circuit and constitutes the basis for the traditional protection criteria of neutral beam injectors. The particular criterion adopted ensures that fast phenomena of importance are not excluded, as a result of an insufficient level of discretisation in the transmission line model. Stricter or more elaborate criteria are of course conceivable, however may lead to a model with hundreds of elements, difficult to manage and cumbersome to run.
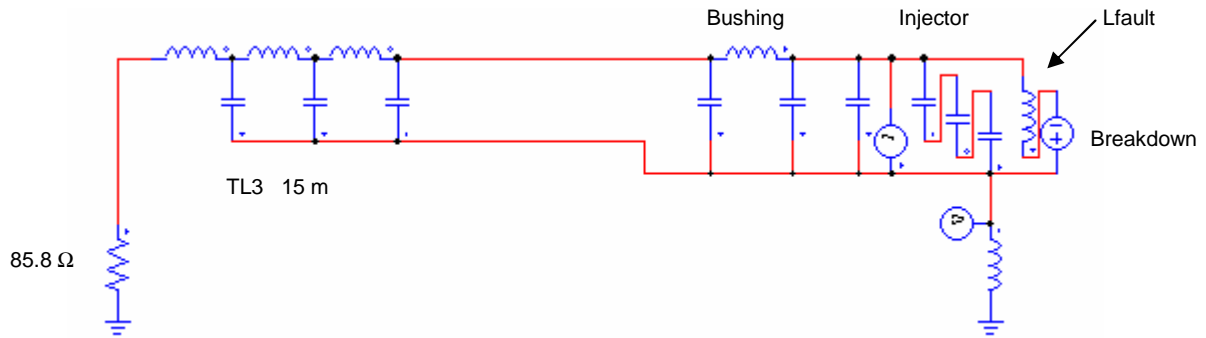
FIG. 4.19 – REDUCED BREAKDOWN MODEL WITH THREE CELL TL3, BUSHING AND ACCELERATOR

The simulated arc current obtained with three cells of 5 m length each is shown in fig. 4.20. From the associated Fourier spectrum (fig. 4.21) it results that the main harmonic component lies at a frequency of 5.6 MHz, with amplitude of 5.0 kA.

The subsequent step halves the length of the transmission line cell, down to 2.5m, increasing at the same time the number of cells to six. The simulation has provided the waveform of fig. 4.22, having its main harmonic component of 3.9 kA amplitude at 5.8 MHz. This frequency is up by more than 3.5% with respect to the three cell case. A further reduction of the cell length is performed, down to 1.25 m and leading to a total of twelve cells. The new simulation is shown in fig. 4.23, giving a main harmonic of 3.5 kA at 5.8 MHz. The frequency of the largest harmonic component has not changed and, according to the criterion previously laid, the cell of 2.5 m length is set as reference for the breakdown simulation with the complete model illustrated below.

A summary of the comparison among the three reduced models can be found in table 4.11.
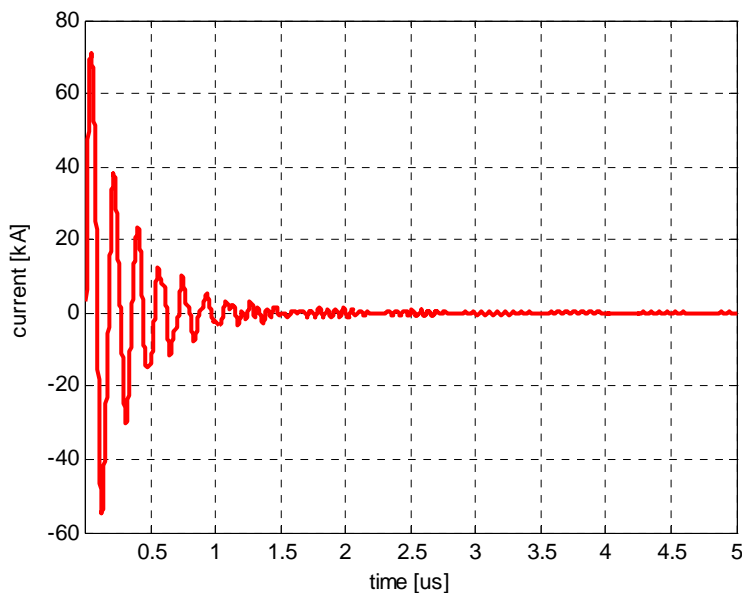
FIG. 4.20 - SIMULATED ARC CURRENT OF THE REDUCED MODEL WITH THREE CELLS
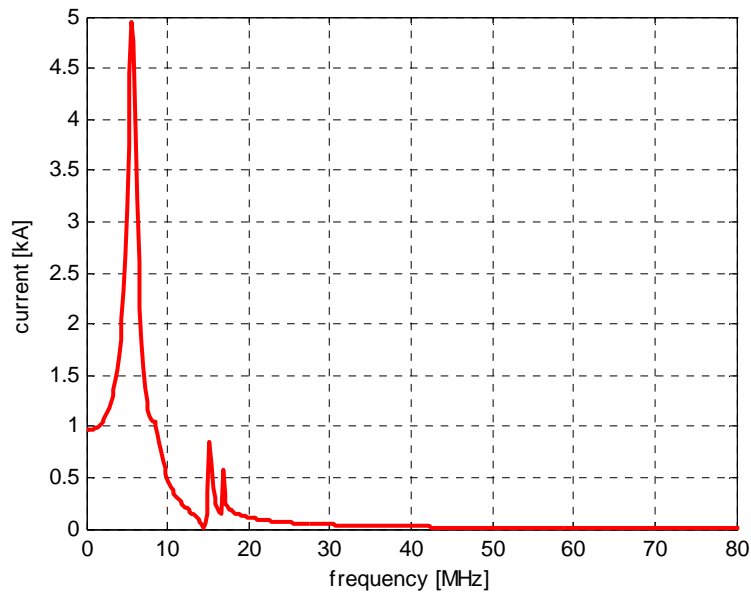
FIG. 4.21 – FOURIER SPECTRUM OF THE ARC CURRENT OF THE REDUCED MODEL WITH THREE CELLS
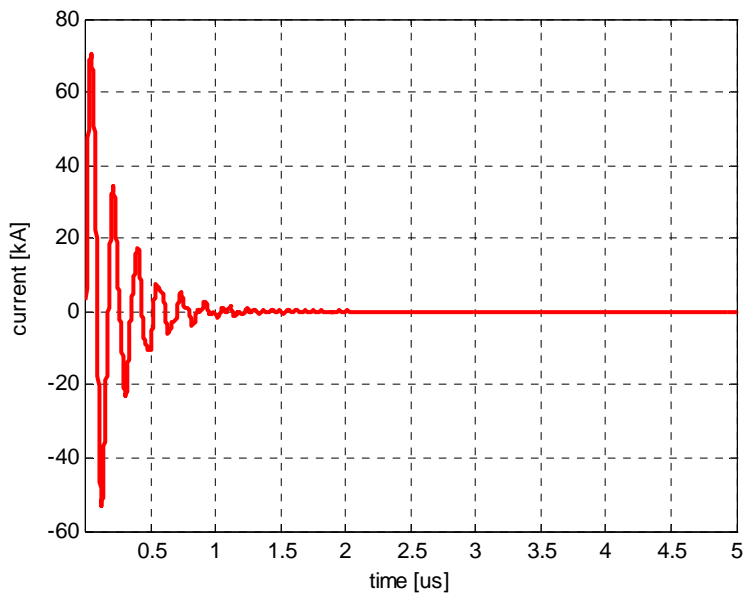
FIG. 4.22 - SIMULATED ARC CURRENT OF THE REDUCED MODEL WITH SIX CELLS
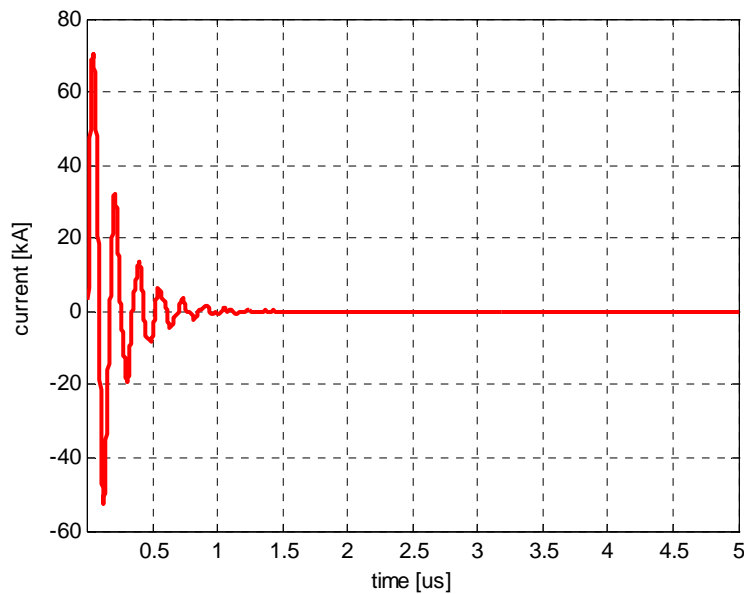
FIG. 4.23 - SIMULATED ARC CURRENT OF THE REDUCED MODEL WITH TWELVE CELLS

TABLE 4.11 - A COMPARISON AMONG THE THREE REDUCED BREAKDOWN MODELS

Number and length of TL3 cells	Largest harmonic component of arc current
Three cells of 5 m each	5.6 MHz (5.0 kA)
Six cells of 2.5 m each	5.8 MHz (3.9 kA)
Twelve cells of 1.25 m each	5.8 MHz (3.5 kA)

4.3.3 Simulation results and limits of the model

In the light of the discussion in the previous paragraph, a length of the transmission line cell of 2.5 m has been applied to the scheme of fig. 4.18, leading to the complete breakdown circuit model of fig. 4.25.

The circuit model has been drawn under the hypothesis of ground reference at constant voltage, as proven by the presence of several "ground" symbols, e.g. "injector grounding" and "HVPS ground". This approach is rather common in circuit modelling and is generally acceptable at low frequencies (in fact it has already been used above, in the ripple studies of §4.2). The consistency of the simulation results will have to be checked carefully against the hypothesis of constant voltage ground.

In fig. 4.25 three distinct passive protection components are included: two core snubbers and an additional resistor in series to the return conductor, at the start of the transmission line. The non-linearity of the core snubbers is disregarded here, an assumption that may be correct if the design of the core snubbers ensures that saturation does not occur during a breakdown. Indeed, the expected flux swing of a core snubber at the breakdown can only be obtained from simulation at system level; nonetheless such a figure is indispensable in the design of the individual component.

The simulation with the model of fig. 4.25 is purely passive and run from the initial condition of all capacitances charged at their rated voltage with respect to ground; in most case, this corresponds to -1 MV, however in the HVPS output filters the other intermediate voltages are present (from -200 kV down to -800 kV). In principle the initial condition for the current in the inductances could also be set to a value different from zero, however the energy stored inductively is negligible as compared to capacitive stored energy. The breakdown is already present in the model at the time of start of the simulation, a time that corresponds therefore also to the instant of the breakdown. The time step of all breakdown simulations is 1 ns.

A first simulation has been run, with the following parameters of the protection components:
- Core snubbers of 1000 Ω, 500μH each

- Additional resistor of 50 Ω

Three waveforms show the results:
- Current through the arc short circuiting the accelerator, fig. 4.26 (in the model it is recorded as the current through the fault inductance *Lfault*)

- Current through the injector grounding path, fig. 4.27 (in the model it is recorded as the current through the associated inductance *Lgnd*)

- Voltage across the filter capacitance of the -1 MV stage, fig. 4.28 (probe *Vfilter1* in fig. 4.25).

The waveform of the arc current has a number of features worth commenting on. The first 2 microseconds following the breakdown (i.e. the start of the simulation) are dominated by fast oscillations with peak amplitude and aspect very close to those obtained with the reduced model (see fig. 4.22). The circumstance confirms that, as postulated earlier on, the core snubbers have little influence on the discharge of stray capacitance close to the injector. After the initial phase, the arc current decays with a far smaller time constant, related to the discharge of the energy stored in the HVPS output filters. At time t=10 μs (end of the simulation), the arc current is still around 5 kA.
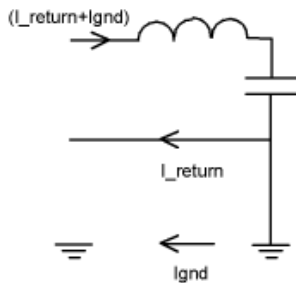
FIG. 4.24 – SIMPLIFIED DIAGRAM OF TL AND GROUND, SHOWING CURRENT PATHS

A first check of the consistency of the results against the assumption made in developing the model leads to consider the decay of the voltage in the HVPS output filters. Waveform *Vfilter1* (fig. 4.28) shows that, at the end of the simulation, the voltage of the filter capacitance of stage #1 is still in excess of 75% of its nominal value, thus legitimising the choice of a purely passive model.

A second check concerns the waveform of the current in the injector grounding path (fig. 4.27). The waveform shows a current in the range of several kiloampères, comparable to the amplitude of the arc current (after the initial 2 microseconds). This implies that a large fraction of the fault current flows through the ground, from the injector grounding point to e.g. the HVPS ground. However, this model is unable to attribute the correct impedance to current that, from the -1 MV conductor, winds its way back to the HVPS filter through the ground. The principle is shown in the simplified circuit of fig. 4.24, including a single cell transmission line: the fraction of the current flowing through the ground, *Ignd*, experiences the same impedance as the fraction of the current flowing through the return conductor, *I_return*, although the associated physical paths and flux linkages are different. This limit of the model has to do mainly with the way the interaction between transmission line and ground has been treated (in actual fact, ignored). The issue could be of little practical relevance, had the simulation shown that the current through the ground is negligible as compared to that through the return conductor. This not being the case, a novel modelling approach will have to developed, integrating in the circuit model of the transmission line the impedance associated to current flowing through the ground. An aspect that certainly requires reliable modelling of the ground impedance is the evaluation of the voltage rise of the return conductor with respect to local ground. With the model of fig. 4.25, the simulated voltage rise to ground at the HVPS end (probe "V_return") is shown in fig. 4.29. A very large value, in excess of 200 kV, results which if confirmed would have an enormous impact on the design. For the time being the waveform of fig. 4.29 is kept aside, for a future comparison with the results of a model including the impedance of the ground.
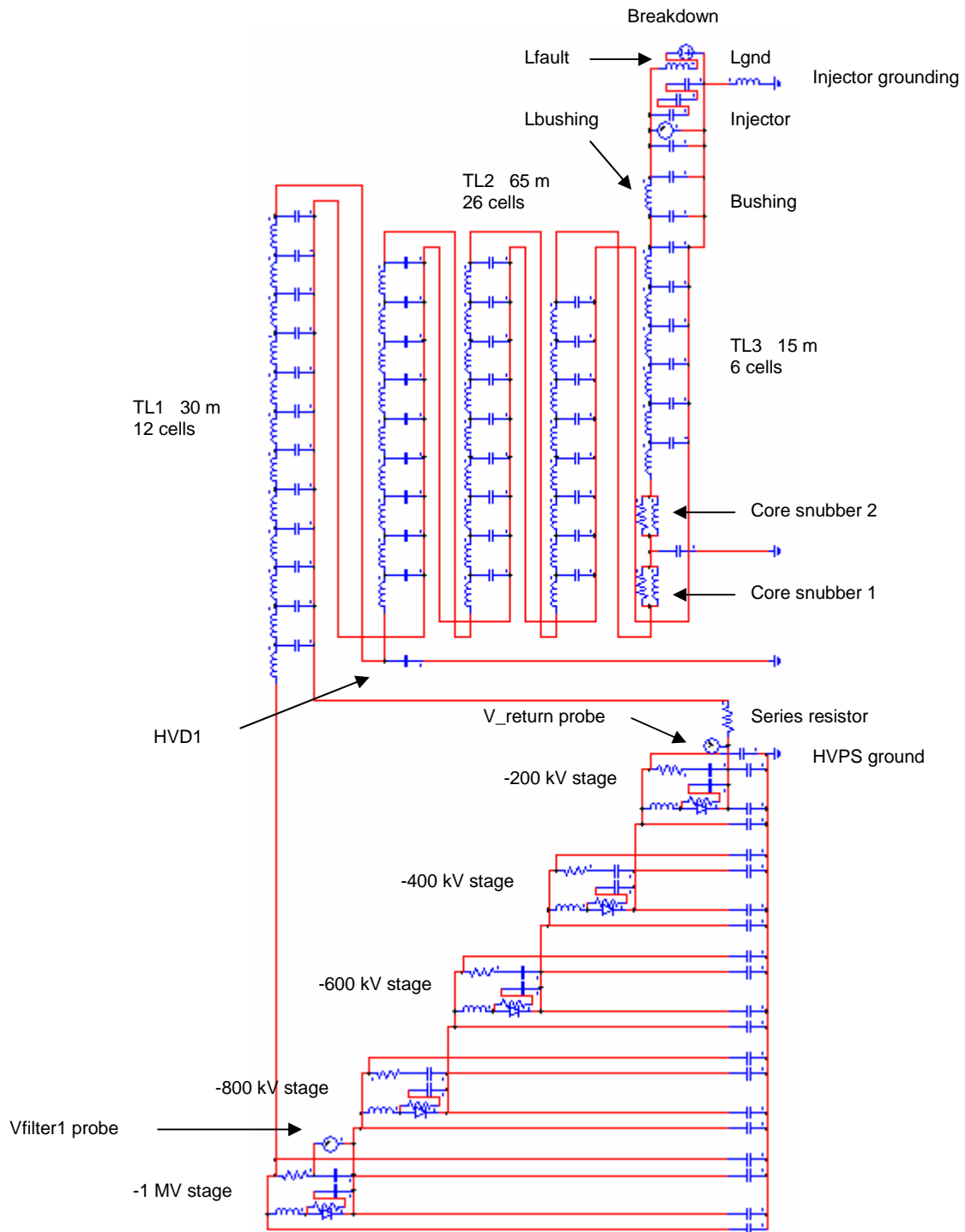
FIG. 4.25 – A FIRST BREAKDOWN CIRCUIT MODEL WITH GROUND REFERENCE AT CONSTANT VOLTAGE
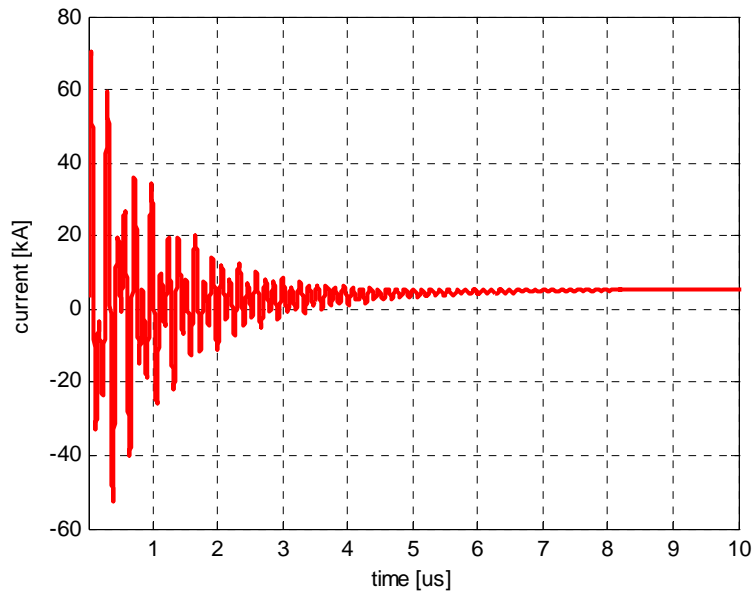
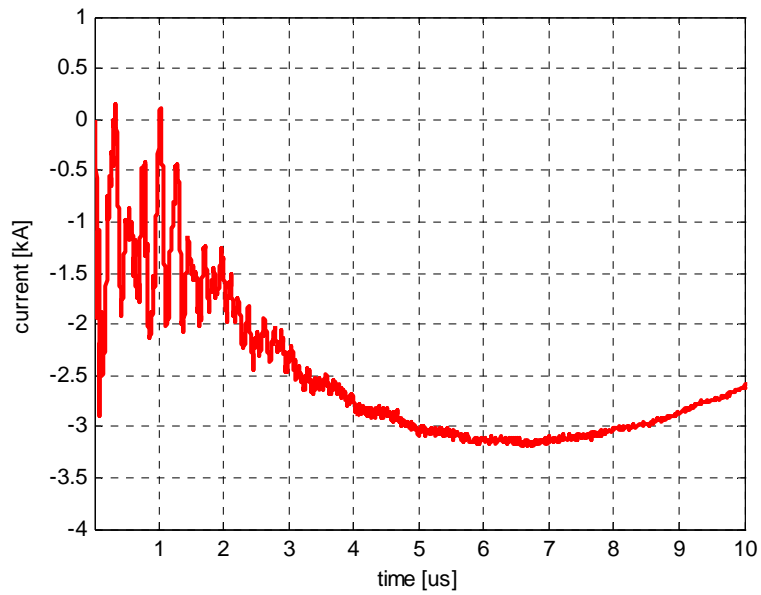*FIG. 4.26 – SIMULATED CURRENT THROUGH THE ARC AT THE BREAKDOWN*

FIG. 4.27 – SIMULATED CURRENT THROUGH INJECTOR GROUNDING AT THE BREAKDOWN
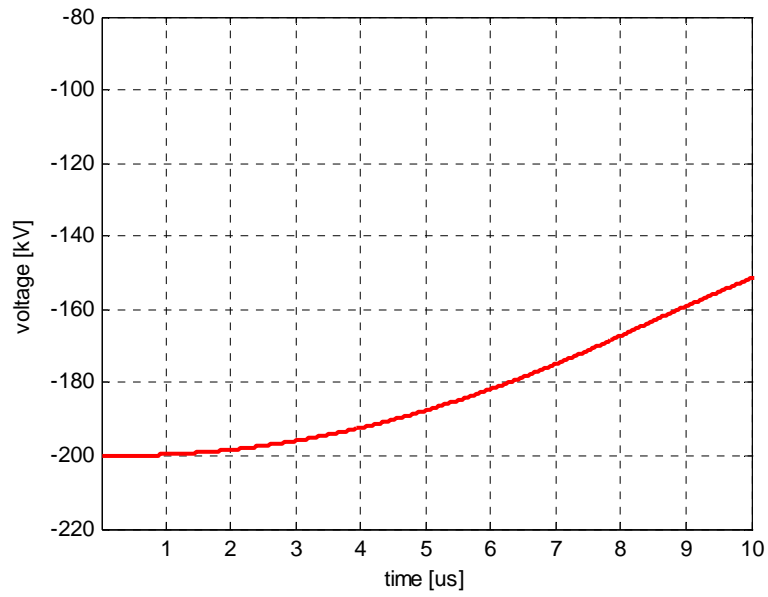
FIG. 4.28 – SIMULATED VOLTAGE AT THE BREAKDOWN ACROSS THE FILTER CAPACITANCE OF THE -1 MV STAGE
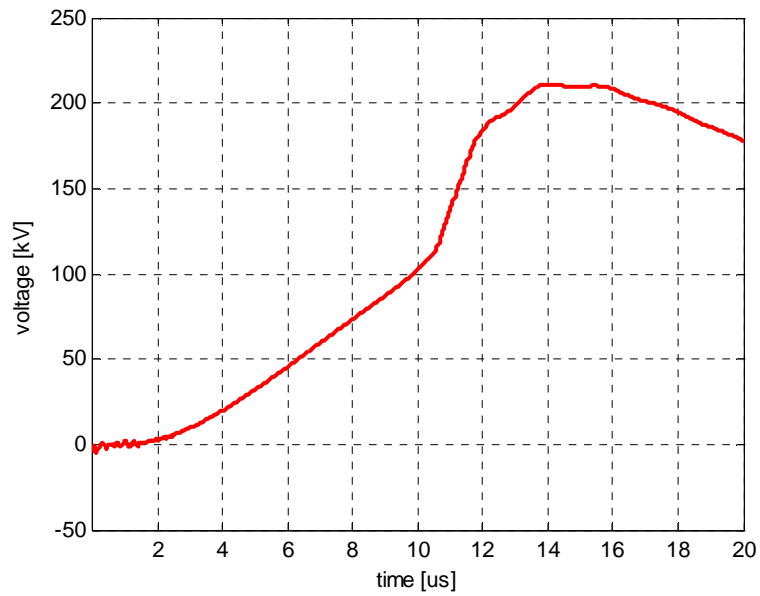

FIG. 4.29 – SIMULATED VOLTAGE RISE OF THE RETURN CONDUCTOR AT THE BREAKDOWN

5. ADVANCED CIRCUIT MODELS FOR LOAD BREAKDOWN

5.1 Circuit model with ground impedance effects

The high voltage circuit of ITER neutral beam injector is composed of several components, located at a distance one from the other that can exceed 100 m. There exist three main localised components, whose size is of the order of few metres:

- HVPS high voltage circuits (isolation transformers, high voltage rectifiers and output filters)

- High voltage deck 1, where the power supplies of the ion source are installed

- The neutral beam injector.

Connection among those is ensured by the coaxial and SF6 insulated transmission line, with an estimated overall length of 110 m.

In §4.3 a first model of the breakdown has been introduced, including stray capacitance to ground of the components mentioned above. Let us consider two sample capacitances: at the one end the stray capacitance to ground of the HVPS filter tank and at the other end the mutual capacitance between pre-acceleration grid and post-acceleration grid (fig. 4.17). In the previous circuit models the former capacitance is directly connected to the ground symbol, representative of a reference at zero voltage irrespective of the transients of the circuit. The latter capacitance is connected, through the inductance for the injector grounding path, to another ground symbol, i.e. to the same voltage reference. The use of the same voltage reference at two locations far apart, in terms of wavelength associated to the fastest transients the system can experience, constitutes an idealisation. Because of the current distribution in the ground and associated flux linkage, in general the potential at the two locations will be different.

Components other than the transmission line are small as compared to the characteristic wavelength of breakdown oscillations, such length being of the order of 30 m (see §4.3.2). As a consequence, the modelling issue of the current flowing in the ground concerns only the transmission line. Let us consider a section of infinitesimal length *dx* of the SINGAP coaxial transmission line, running above the ground (fig. 5.1). This is viewed as a system of three conductors, TL inner conductor, TL outer conductor and ground, mutually coupled both inductively and capacitively. Let us consider the inductive coupling first. Having labelled the currents of the three conductors i_{TL}, i_{OUTER} and i_{GROUND}, Kirchhoff's current law imposes that, at each location along the transmission line, their sum be zero even in presence of transverse capacitance, whose currents are infinitesimals of higher order:

$$i_{TL} + i_{OUTER} + i_{GROUND} = 0 \qquad (5.1)$$

It is convenient to choose the TL outer conductor as return for the current of the other two conductors, with the position:

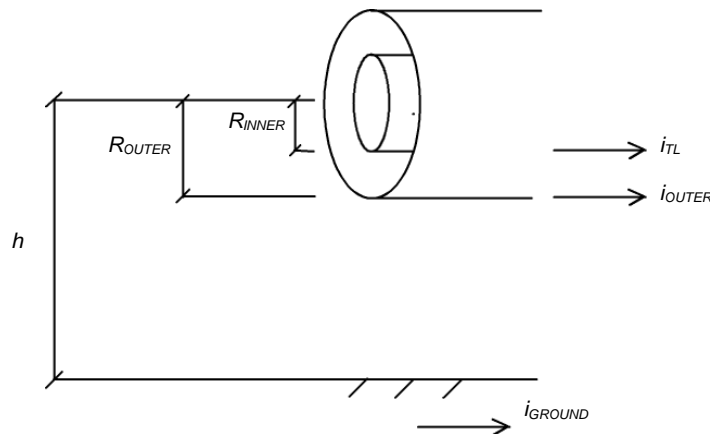$$i_{OUTER} = -i_{TL} - i_{GROUND} \qquad (5.2)$$

FIG. 5.1 – A SECTION OF THE TRANSMISSION LINE RUNNING ABOVE THE GROUND

To the resulting magnetic field, the current distribution of fig. 5.1 is equivalent to the superposition of two separate circuits (fig. 5.2):

- A circuit formed by the transmission line inner and outer conductors, labelled "TL circuit" and characterised by current i_{TL}

- A circuit formed by the ground and the transmission line outer conductor, labelled "ground circuit" and characterised by current i_{GROUND}.
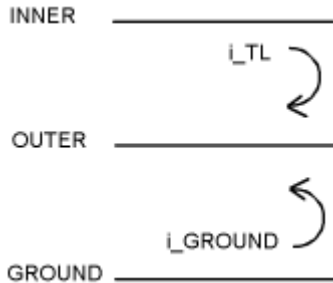

FIG. 5.2 – TRANSMISSION LINE VIEWED AS SUPERPOSITION OF TWO SEPARATE CIRCUITS

This is an instance of the generic situation arising with a system of *n* conductors, satisfying Kirchhoff's current law: once a reference conductor is selected as return for the current of the remaining *(n-1)* conductors, *(n-1)* coupled circuits are identified and inductive and capacitive couplings described by *(n-1)×(n-1)* matrices.

In the case of the transmission line and ground, the choice of the TL outer conductor as a return simplifies things noticeably, because the mutual inductance between the two resulting circuits is zero. The circumstance is easily verified: when current i_{TL} flows in the "TL circuit", because of the coaxial geometry there is no magnetic field outside the transmission line and therefore no flux linked with the "ground circuit". In other words, the inductance matrix of the system of coupled circuits,

$\mathbf{L}_{TLG}$, is diagonal:

$$\mathbf{L}_{TLG} = \begin{bmatrix} L_{TL} & 0 \\ 0 & L_{GND} \end{bmatrix}$$

(5.3)

The capacitive couplings have a similar structure, with a diagonal matrix $\mathbf{C}_{TLG}$:

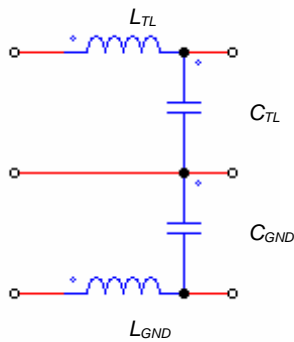$$\mathbf{C}_{TLG} = \begin{bmatrix} C_{TL} & 0 \\ 0 & C_{GND} \end{bmatrix}$$

(5.4)

FIG. 5.3 – PER UNIT LENGTH CIRCUIT MODEL OF TRANSMISSION LINE AND GROUND

The physical motivation being that the TL outer conductor screens electrostatically the ground from the TL inner conductor and vice versa.

At this stage, the per unit length circuit model of transmission line and ground is fully defined and has the structure shown in fig. 5.3.

The self inductance per unit length of the "TL circuit", L_{TL}, is given by the classic formula for two coaxial conductors of radiuses R_{OUTER} and R_{INNER}:

$$L_{TL} = \frac{\mu_0}{2\pi} \ln\left(\frac{R_{OUTER}}{R_{INNER}}\right)$$

(5.5)

The calculation of the self inductance per unit length of the "ground circuit", L_{GND}, will be performed here under the assumption of perfectly conducting ground. The method of image currents can be used, substituting the ground current with an image conductor located at a depth *h* below the ground surface (fig. 5.4). The magnetic flux per unit length to be calculated is the one linked with the dashed area comprised between the ground surface and the TL outer conductor. This flux φ_{GROUND} is calculated adding together a

contribution φ_{IMAGE}, due to a current i_{GROUND} flowing in the image conductor and a contribution φ_{OUTER}, due to a current $-i_{GROUND}$ flowing in the TL outer conductor:

$$\varphi_{IMAGE} = \frac{\mu_0}{2\pi} i_{GROUND} \int_{h}^{(2h-R_{OUTER})} \frac{dr}{r} = \frac{\mu_0}{2\pi} i_{GROUND} \ln\left(\frac{2h - R_{OUTER}}{h}\right) \tag{5.6}$$

$$\varphi_{OUTER} = \frac{\mu_0}{2\pi} i_{GROUND} \int_{R_{OUTER}}^{h} \frac{dr}{r} = \frac{\mu_0}{2\pi} i_{GROUND} \ln\left(\frac{h}{R_{OUTER}}\right) \tag{5.7}$$

$$\varphi_{GROUND} = \varphi_{IMAGE} + \varphi_{OUTER} = \frac{\mu_0}{2\pi} i_{GROUND} \ln\left(\frac{2h - R_{OUTER}}{R_{OUTER}}\right) \tag{5.8}$$

The expression of φ_{GROUND} leads to the self inductance of the "ground circuit":

$$L_{GND} = \frac{\mu_0}{2\pi} \ln\left(\frac{2h - R_{OUTER}}{R_{OUTER}}\right) \tag{5.9}$$
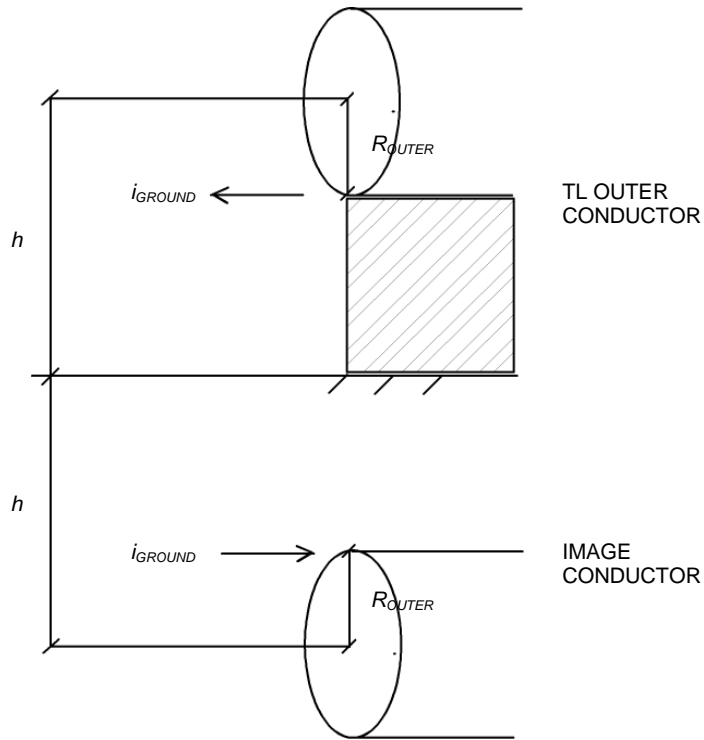
FIG. 5.4 – THE METHOD OF IMAGE CURRENTS APPLIED TO THE COMPUTATION OF THE GROUND INDUCTANCE

The self-capacitance of the transmission line, C_{TL}, is given by:

$$C_{TL} = \frac{2\pi\varepsilon_0}{\ln\left(\frac{R_{OUTER}}{R_{INNER}}\right)} \tag{5.10}$$

The self-capacitance of the "ground circuit", C_{TL}, can be computed with the method of image charges, leading to the following expression:

$$C_{GND} = \frac{2\pi\varepsilon_0}{\ln\left(\frac{2h - R_{OUTER}}{R_{OUTER}}\right)} \tag{5.11}$$

The above ground parameters have been calculated for perfectly conducting ground, in which case the ground current distribution is purely superficial. If the ground is not perfectly conducting, additional ground internal inductance and resistance arise, as a result of the current distribution within the medium [47]. Expressions exist for these extra parameters, as a function of frequency. Here it is preferred to adopt the simpler hypothesis of perfectly conducting ground, since the inductance of eq. (5.9) is expected to represent the majority of the impedance in the ground path.

The newly developed circuit model of the transmission line addresses the main issue raised by the breakdown analyses with ground at constant voltage (§4.3). From this point onward, the transmission line cell of fig. 5.3 will appear in all breakdown simulations. For ITER NBI, table 5.1 contains the updated list of the transmission line parameters, where to those of table 3.5 have been added the "ground circuit" parameters, calculated according to eq. (5.9) and eq. (5.11). The resulting values of ground inductance and capacitance are comparable to those of the transmission line, suggesting a rather different scenario from the one of the model with ground at constant voltage.

TABLE 5.1 – ITER TRANSMISSION LINE PARAMETERS INCLUDING GROUND INDUCTANCE AND CAPACITANCE

	TL1	*TL2*	*TL3*
Inner diameter	400 mm	400 mm	400 mm
Outer diameter	1100 mm	1100 mm	1650 mm
Inductance per unit length	0.2 µH/m	0.2 µH/m	0.28 µH/m
Capacitance per unit length	55 pF/m	55 pF/m	39 pF/m
Estimated length	30 m	65 m	15 m
Estimated height over the ground (average)	1 m	1 m	10 m
Ground inductance per unit length	0.19 µH/m	0.19 µH/m	0.63 µH/m
Ground capacitance per unit length	57 pF/m	57 pF/m	18 pF/m

5.2 Experimental validation on the Joint European Torus (JET)

In the previous paragraph a circuit model integrating ground inductance and capacitance into the transmission line cell been proposed. As already mentioned in the overview of literature on neutral beam circuit analyses (§3.3.1), such an approach is unprecedented and if applied directly to the breakdown simulation of ITER NBI, where no experimental validation is possible, could face a sceptical reception. This concern would be even greater if dramatic results, contrary to widespread belief, were to be predicted by the circuit model.

Those considerations suggested the opportunity to look for a way to validate on an operational neutral beam injector the ground impedance model, before applying it to ITER.

The issue of the voltage rise of the return conductor with respect to local ground, during a breakdown and at some distance from the injector, seemed in several respects an ideal benchmark:

- The execution of experimental measurements is feasible

- The issue has drawn no attention in literature, nonetheless will be of great interest to the design of ITER NBI

- A simulation of the voltage rise with respect to ground implies some evolved circuit modelling of the ground conductor.

Once decided on the benchmark, a threefold validation process would follow:
1) Recording of experimental waveforms for the voltage rise of the return conductor during breakdowns

2) Development of a circuit model with ground impedance, for the injector where the experimental data are captured

3) Comparison between experiment and simulation.

The choice fell on the neutral beam system of the Joint European Torus, for a combination of scientific and practical reasons. On the one hand, as a result of recent enhancements [41] some of JET Positive Ion Neutral Injectors (PINIs) are equipped with inverter-based HVPSs, similar in the circuit structure to the ones foreseen for ITER. On the other hand, there exist a large gap in voltage between JET injectors, working at 130 kV, and ITER's 1 MV. However the only tokamak with injectors at a voltage substantially higher than 130 kV is JT-60U in Naka (Japan), where energies as high as 400 keV were achieved [15]. Experimental access to JET appeared reasonably easy within the framework of the European fusion programme, whereas with JT-60U and ad hoc collaboration would have to be set up, in a timescale difficult to predict.

A proposal for the measurement of the voltage of the return conductor on the JET injectors was launched in January 2007 and endorsed within few weeks. The plan foresaw that the activity would be carried out in the second half of March 2007, on the circuit of those PINIs supplied by inverter based HVPSs. At that time the majority of JET injectors was still fed by old "star point controller" HVPSs [20,57], with the use of tetrodes as fast cut-off switches.

Unfortunately, few days before the planned start of the voltage measurements the PINIs in question suffered major water leaks that took out them out of operation. To make things worse, at the end of March 2007 was to begin a six month long shutdown of the JET machine. In absence of alternatives, it was decided to attempt voltage measurements of the return conductor on the PINIs left in operation, although these had the old circuit topology with "star point controller" HVPS and tetrodes. The last minute change was successful and useful data were recorded, providing a basis for the validation of the breakdown simulations as illustrated below.

5.2.1 The power supply system of JET neutral beams

The high voltage circuit of those JET injectors on which the return conductor voltage was measured during breakdowns is shown in fig. 5.5 [14,18]. The HVPS is of the "star point controller" type [20,57], with voltage regulation performed by thyristors. The output of the HVPS is connected through a cable of 180 m length to a protection cabinet, hosting (among other components) a series tetrode, for fast regulation of the voltage during beam extraction and cutoff upon detection of a breakdown. Downstream of the protection unit an 85 m long, SF6 insulated and coaxial transmission line starts, taking electrical and other supplies to ion source and accelerator. A core snubber, encircling the inner conductor of the transmission line, is placed close to the injector for load protection. The only grounded point of the circuit is at the injector end. In a "high voltage deck", located in the vicinity of the protection unit and supplied through an isolation transformer, the ion source power supplies are installed. The high voltage deck platform is connected to the high voltage pole of the HVPS; the ISPS instead are referred to the HVPS high potential through a resistor [58].

Upstream of the SF6 transmission line, the topology of the old JET circuit differs substantially from the ITER one. In terms of behaviour at the breakdown, the main difference is represented by the interruption performed by the series tetrode. On the contrary, with an inverter based HVPS a dc current path always exist even after the inverters have blocked their active devices, through the high voltage rectifier diodes. The work of Edwards et al. [41] shows the different decays of the breakdown current, in a comparison between the old JET circuit of fig. 5.5 and the new JET circuit with solid state HVPS.

Downstream of the protection cabinet the type of components found on JET is identical to the ones on ITER. One may argue that at the breakdown, before the tetrode intervenes, also the dynamics of the fault in the two cases will be similar.

5.2.2 Voltage measurements on return conductor

The measurements of the return conductor voltage were performed at the protection cabinet, as indicated in fig. 5.5. One end of the probe was connected to the return conductor and the other end to an earthing bar, both inside the protection cabinet. A photograph taken from the thorough review by Claesen and Mondino [18] shows the interior of the protection cabinet (fig. 5.6).

A high voltage probe by Tektronix [59], type P6015A with 75 MHz bandwidth, was used. The signal output by the high voltage probe was recorded with a digital oscilloscope DL 1640 by Yokogawa [60], at a sampling rate of 50 Ms/s. The oscilloscope was powered by its own battery pack and had no electrical connection to the mains during JET plasma discharges. The oscilloscope was triggered by the return conductor voltage itself, with trigger levels between 50V and 100V (these figures refer to the actual value of the voltage on the plant, at the net of the 1:10 ratio of the probe). Ideally, it could have been useful to trigger on some

independent digital signal coming from the breakdown detection electronics, however this would have required advance preparation, also because of galvanic isolation (as mentioned above, the oscilloscope was run on batteries to avoid noise pick-up through the mains). A scheme with a digital trigger signal had been prepared for the HVPS of the new type, on which the return conductor voltage measurements had been originally planned. Unfortunately the water leak mentioned in the previous paragraph forced to switch to the old power supply system and it proved impossible in the tight timescale to arrange for a digital trigger of the breakdown.
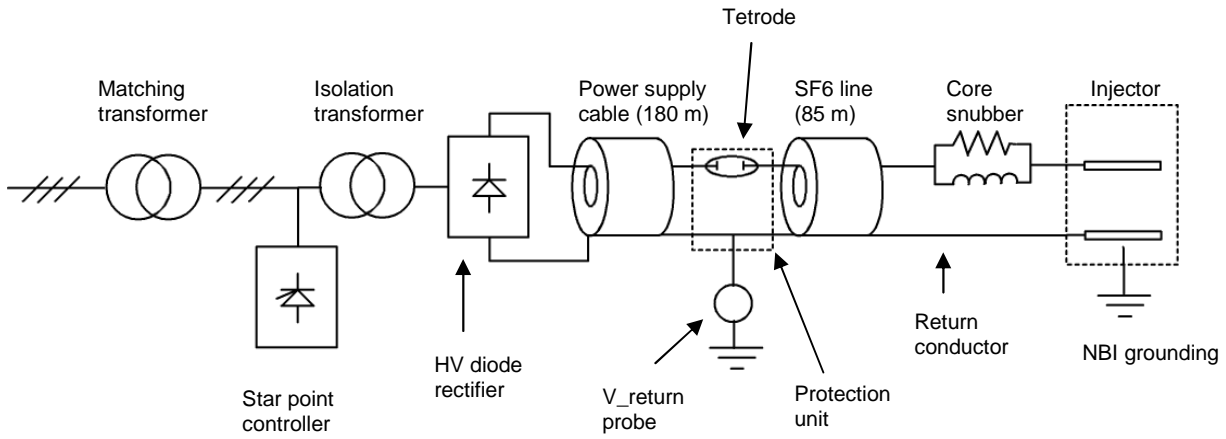
FIG. 5.5 – SIMPLIFIED DIAGRAM OF THE JET HIGH VOLTAGE CIRCUIT OF THE OLD TYPE
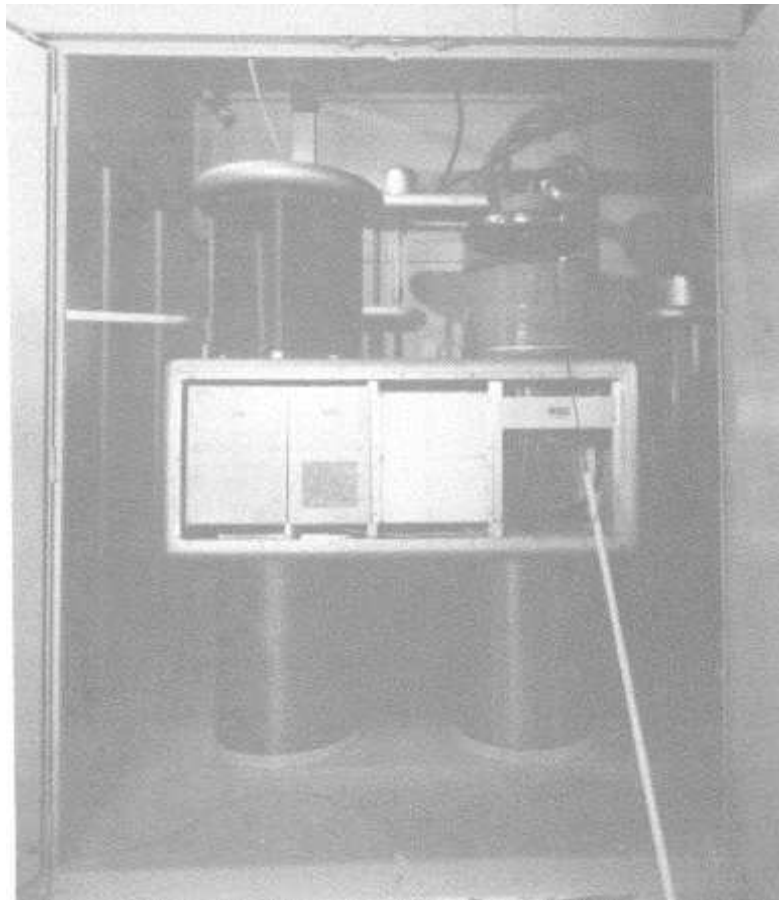
FIG. 5.6 – INTERIOR OF THE PROTECTION CABINET FOR JET HVPS OF THE OLD TYPE

In total about fifteen JET plasma discharges were monitored and eleven voltage waveforms recorded (all shown below). A log book of the experimental activity can be found in table 5.2, including an entry for the "number of breakdowns": these figures were read from a breakdown counter on the front panel of the HVPS, displaying the number of breakdowns over the previous PINI pulse. The parameters are also listed characterising the PINI pulse:

1) Flat top "beam current"

2) Flat top "HVPS input voltage". This is the voltage at the input of the protection cabinet, generated by the "star point controller" power supply

3) Flat top "HVPS output voltage". This is the voltage effectively applied to the PINI acceleration gap. The difference between "HVPS input voltage" and "HVPS output voltage" corresponds to the voltage drop of the series tetrode inside the protection cabinet

4) Pulse duration.

Typical waveforms for the above quantities, as taken from JET pulse file # 70499, are shown in fig. 5.7 (beam current), fig. 5.8 (HVPS input voltage) and fig. 5.9 (HVPS output voltage). The comparison between HVPS input ad output voltages illustrates the role of the tetrode as a switch that turns on the PINI. Note also that the one breakdown of pulse # 70499 is clearly visible at the available sampling rate of 5 kHz. After a breakdown, the power supplies are blocked for a dead time of 40 ms before reapplying the voltage.

The oscilloscope was set up in the "single" trigger mode, i.e. recording the first event within a given JET plasma discharge. In principle there exists no certified proof that the events recorded actually correspond to PINI breakdowns. However, good confidence that this is the case was gained in that instance (pulse no. 70496) when the pulse experienced no breakdowns and the oscilloscope did not trigger.

In general, the recorded waveforms of the return conductor voltage show a good consistency of pattern and even of peak values of the voltage, with a maximum voltage between 300 V and 350 V in most cases. However, there are two instances (# 70498 and # 70503) in which the peak was clipped at ±500 V by the end of scale. The frequency of the voltage oscillations is in the range of few hundred kilohertz up to about 1 MHz, as confirmed by the typical FFT of fig. 5.21. The peak of the spectrum is at 749 kHz, a value that even visually matches well with the time domain waveform, where about four cycles are visible within the first 5 μs after the breakdown (fig. 5.16).
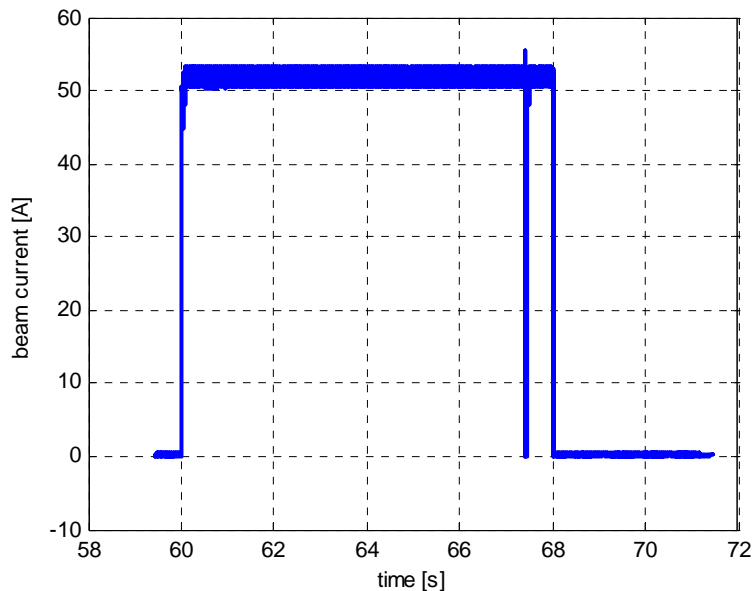

FIG. 5.7 – BEAM CURRENT WAVEFORM FOR PULSE # 70499 (REF. MODULE 9.2, PULSE FILE GP9-IOUT<AVX:001)

TABLE 5.2 – RECORD OF THE WAVEFORMS CAPTURED ON JET

| JET pulse no.	Date and local time	PINI parameters Beam current HVPS input volt. HVPS output volt. Pulse duration	No of breakdowns	Trigger settings	Notes
# 70489	23 March 07 11:20	52 A 89 kV 75 kV 8 s	1	50 V 2 µs pre-trigger	Waveform recorded (20 µs duration, ≅1000 samples))
# 70490	23 March 07 11:46	52 A 89 kV 75 kV 8 s	5	100 V 2 µs pre-trigger	Waveform recorded
# 70491	23 March 07 12:38	52 A 89 kV 75 kV 8 s	Not known	100 V 2 µs pre-trigger	Waveform recorded
# 70493	23 March 07 13:34	52 A 89 kV 75 kV 8 s	1	100 V 2 µs pre-trigger	Waveform recorded
# 70494	23 March 07 14:05	52 A 89 kV 75 kV 8 s	2	100 V 2 µs pre-trigger	No trigger
# 70495	23 March 07 14:34	52 A 89 kV 75 kV 8 s	3	70 V 2 µs pre-trigger	No trigger
# 70496	23 March 07 14:59	52 A 89 kV 75 kV 8 s	0	50 V 2 µs pre-trigger	No trigger
# 70497	23 March 07 15:20	52 A 89 kV 75 kV 8 s	1	50 V 2 µs pre-trigger	Waveform recorded
# 70498	23 March 07 15:50	52 A 89 kV 75 kV 8 s	Not known	50 V 2 µs pre-trigger	Waveform recorded
# 70499	23 March 07 16:20	52 A 89 kV 75 kV 8 s	1	50 V 2 µs pre-trigger	Waveform recorded
# 70500	23 March 07 16:49	52 A 89 kV 75 kV 8 s	1	50 V 10 µs delay	Waveform recorded, trigger delayed to catch tail of waveform
# 70501	23 March 07 17:09	52 A 89 kV 75 kV 1.6 s	0	100 V 2 µs pre-trigger	Waveform recorded but HVPS trip "Regulation amplifier error high"
# 70502	23 March 07 17:24	52 A 89 kV 75 kV 8 s	1	50 V 2 µs pre-trigger	Waveform recorded
# 70503	23 March 07 18:09	50 A 85 kV 72 kV 8 s	2	50 V 2 µs pre-trigger	Waveform recorded
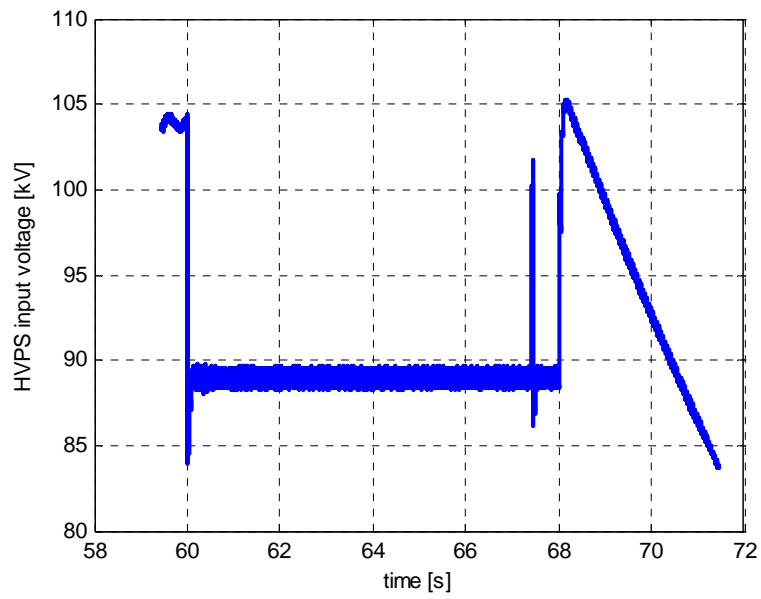
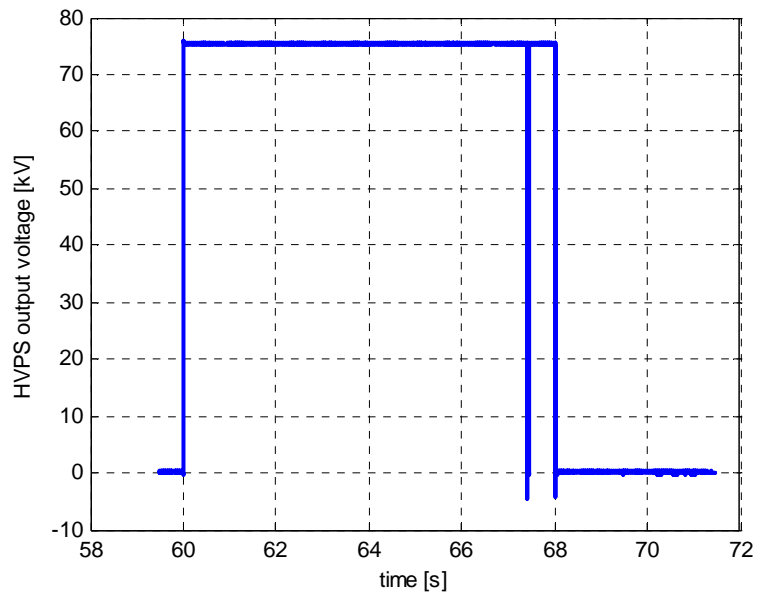*FIG. 5.8 – HVPS INPUT VOLTAGE WAVEFORM FOR PULSE # 70499 (PULSE FILE GP9-VIN<VVX:001)*

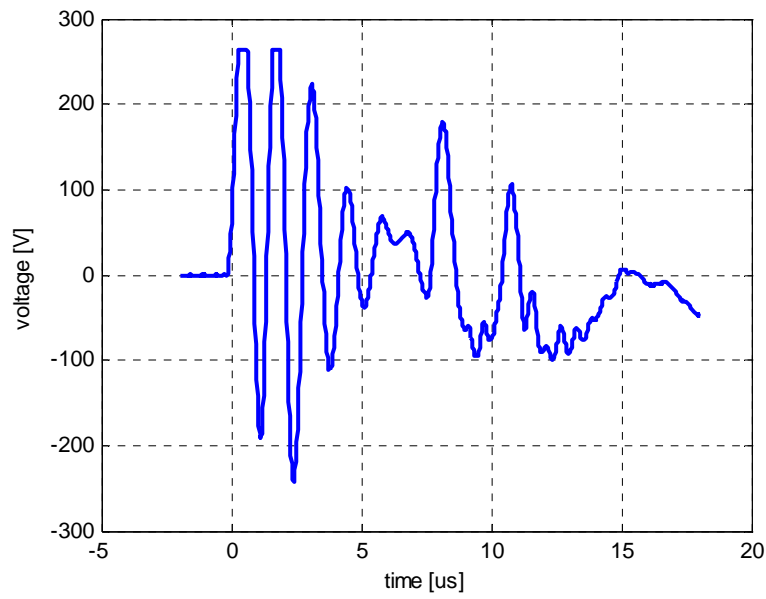*FIG. 5.9 – HVPS OUTPUT VOLTAGE WAVEFORM FOR PULSE # 70499 (PULSE FILE GP9-VOUT<VVX:001)*

FIG. 5.10 – RETURN CONDUCTOR VOLTAGE RECORDED DURING JET PULSE # 70489
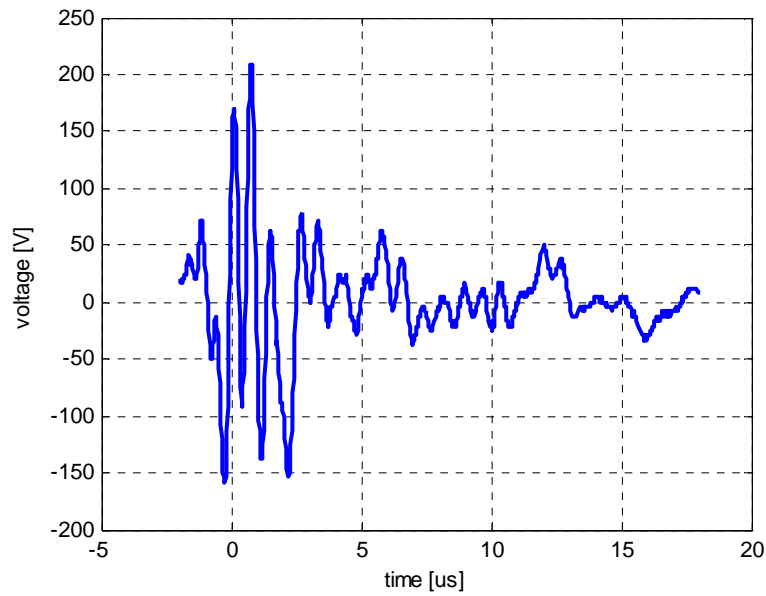

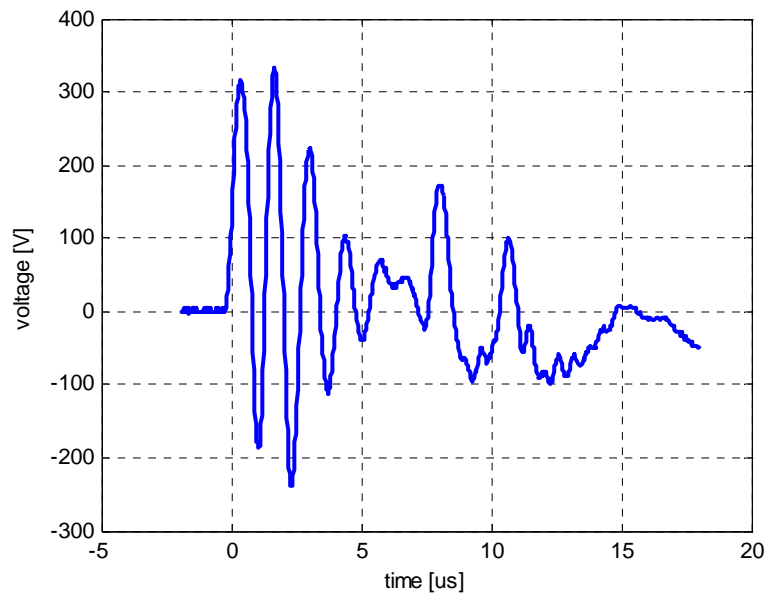*FIG. 5.11 – RETURN CONDUCTOR VOLTAGE RECORDED DURING JET PULSE # 70490*

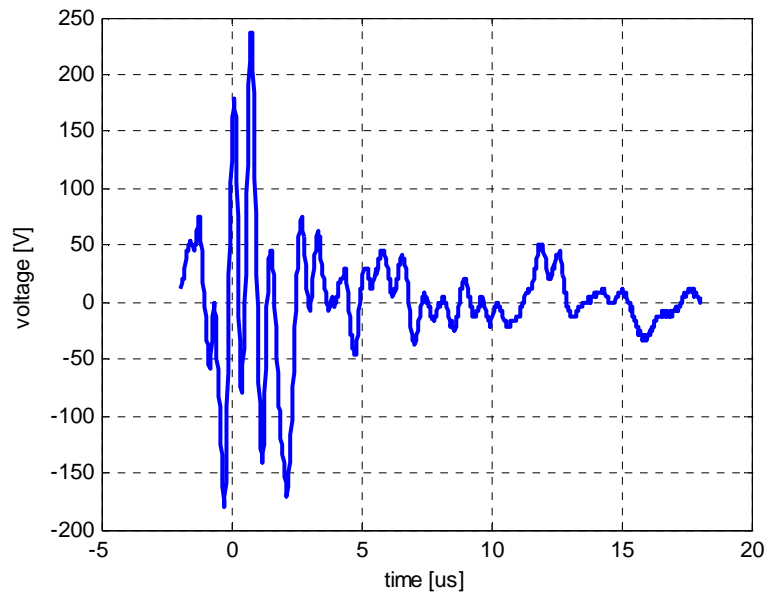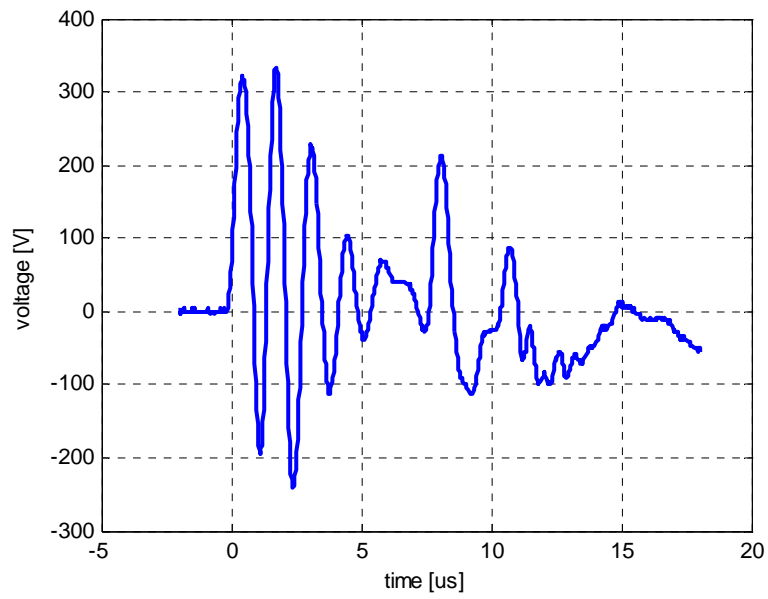*FIG. 5.12 – RETURN CONDUCTOR VOLTAGE RECORDED DURING JET PULSE # 70491*

FIG. 5.13 – RETURN CONDUCTOR VOLTAGE RECORDED DURING JET PULSE # 70493

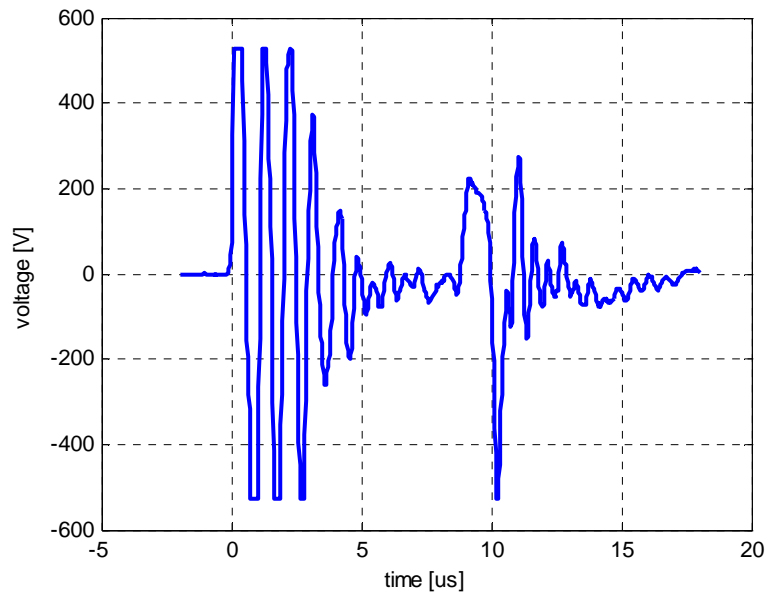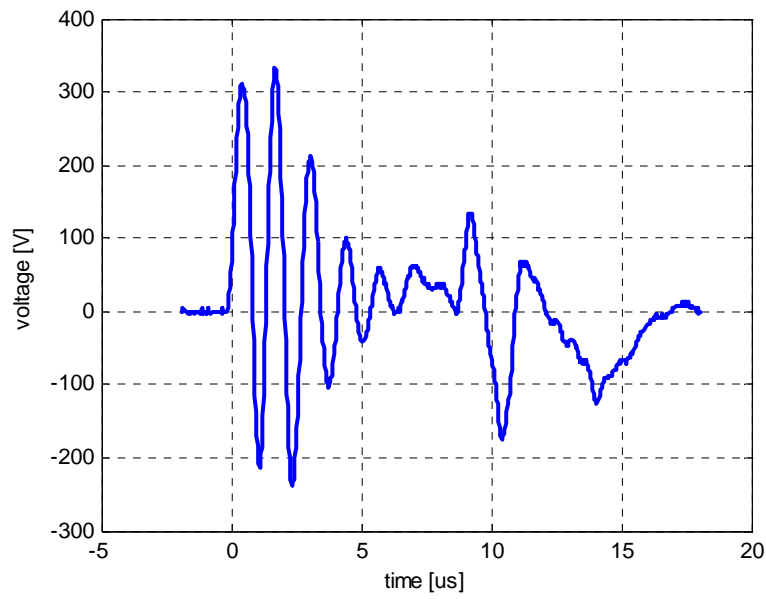*FIG. 5.14 – RETURN CONDUCTOR VOLTAGE RECORDED DURING JET PULSE # 70497*

FIG. 5.15 – RETURN CONDUCTOR VOLTAGE RECORDED DURING JET PULSE # 70498

FIG. 5.16 – RETURN CONDUCTOR VOLTAGE RECORDED DURING JET PULSE # 70499
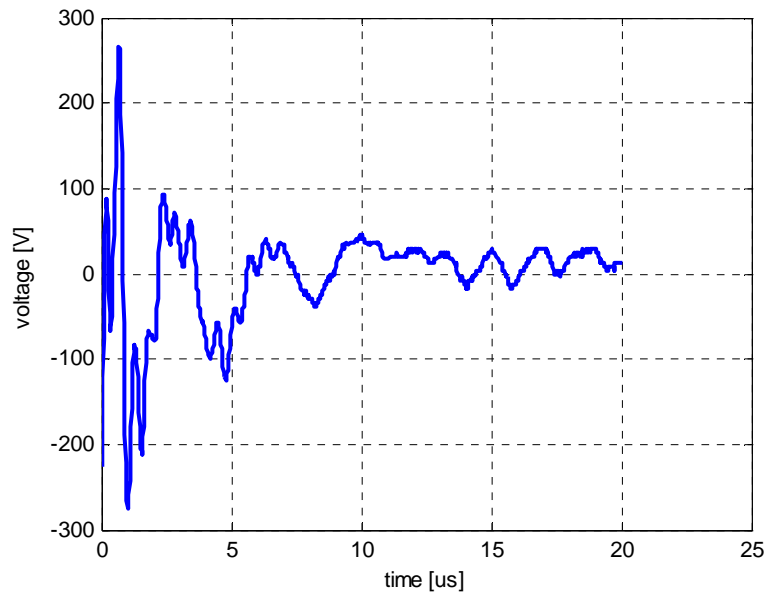

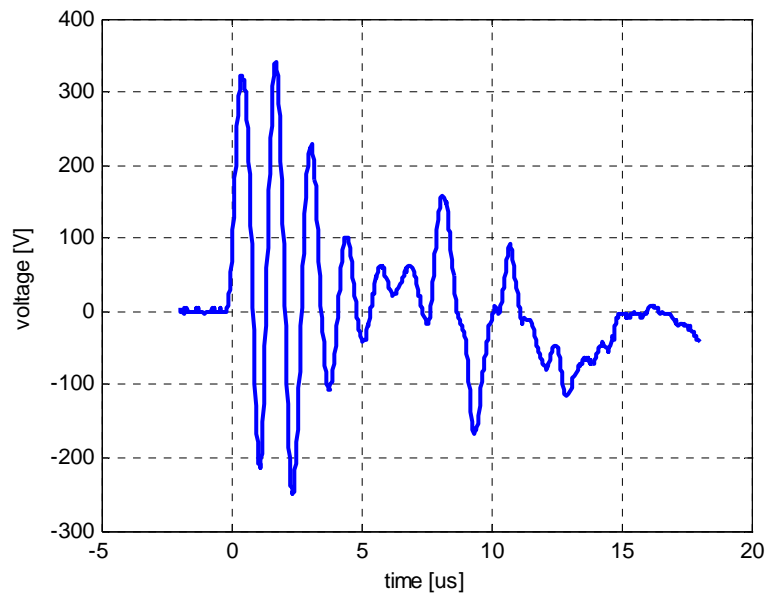*FIG. 5.17 – RETURN CONDUCTOR VOLTAGE RECORDED DURING JET PULSE # 70500*

FIG. 5.18 – RETURN CONDUCTOR VOLTAGE RECORDED DURING JET PULSE # 70501
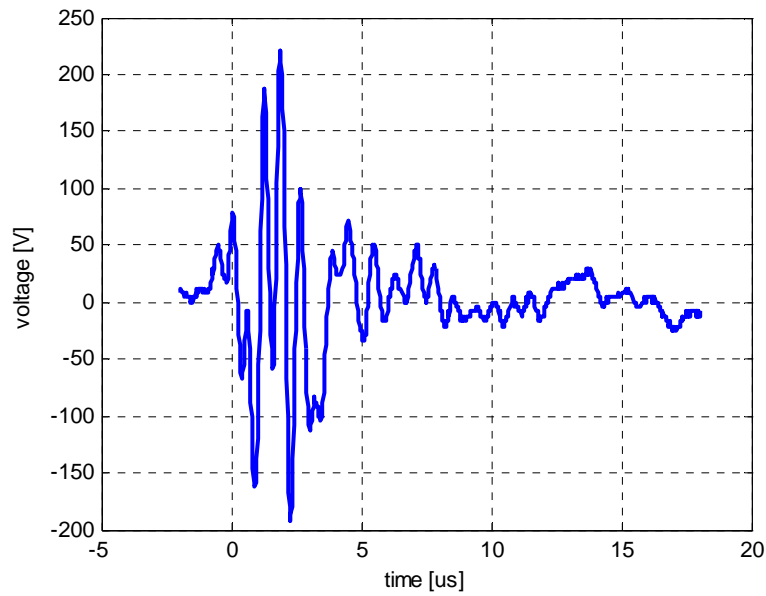

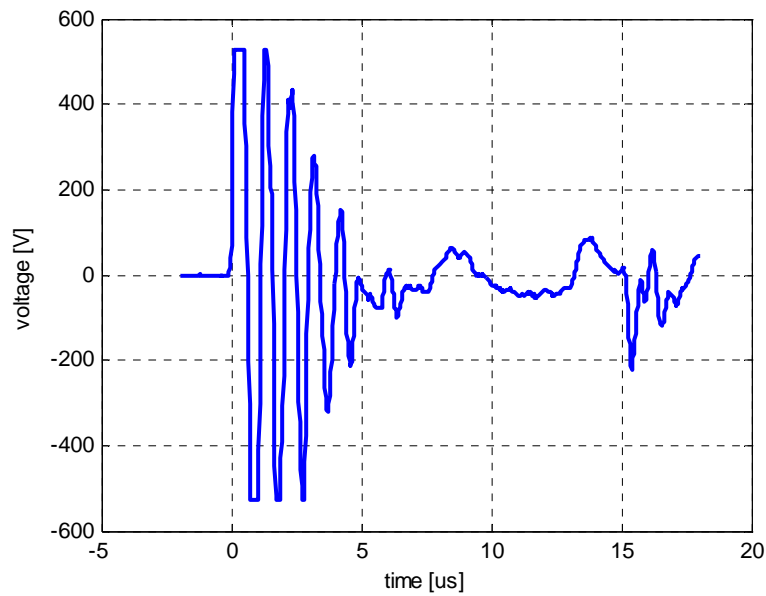*FIG. 5.19 – RETURN CONDUCTOR VOLTAGE RECORDED DURING JET PULSE # 70502*

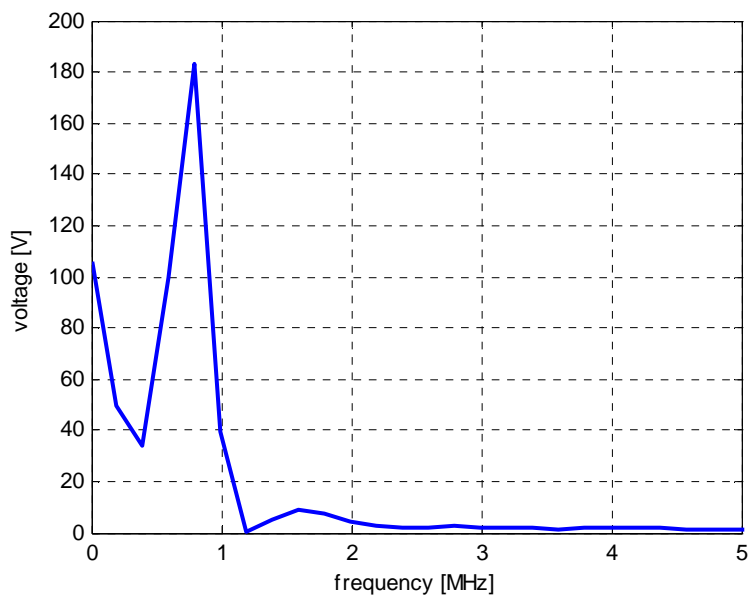*FIG. 5.20 – RETURN CONDUCTOR VOLTAGE RECORDED DURING JET PULSE # 70503*

FIG. 5.21 – FFT OF THE WAVEFORM OF THE RETURN CONDUCTOR VOLTAGE FOR PULSE # 70499

5.2.3 A novel model with ground impedance

The approach to modelling of the ground impedance proposed in §5.1 for ITER will be used to develop for JET a circuit simulation of the return conductor voltage rise during a breakdown, to be compared with the experimental findings illustrated in the previous paragraph.

The model of Jensen et al. [22], already introduced in §3.3.1, constitutes a good basis, as far as many parameters of most components are concerned. Also the works of Aslin et al. [57] and of Basile et al. [58] have proven extremely valuable sources of information.

Building on the model of Jensen et al., the following key changes have been made:

- A distributed model, with cells of 3 m length including the impedance of the ground conductor, has been employed for both SF6 transmission line and power supply cable

- The "high voltage deck" has been included, along with the associated stray capacitance (partly due to the stray capacitance of the isolation transformer windings to the electrostatic screen and partly due to the physical structure of the deck as a Faraday cage)

- The stray capacitance has been added, of the protection cabinet where the measurements of the return conductor voltage were taken

- Stray inductance has been associated to the grounding paths of protection cabinet, high voltage deck and injector. It will turn out that the former two parameters have an important effect on the simulated waveform of the return conductor voltage.

Stray capacitances for main acceleration gap and diode rectifier tanks have also been added. Accurate modelling of the arc short circuiting the accelerator is not viewed as important to the objective of this simulation. The fault is simply represented by a small inductance of 100 nH accounting for the path of the arc. The simulation is not purely passive: a dc voltage source with series diode represents the "star point controller" power supply. For the dc voltage source an amplitude of 89 kV has been chosen, corresponding to the value of the HVPS input voltage recorded on the experiment during beam extraction (fig. 5.8 and table 5.2). The tetrode is modelled by a diode of 14 kV voltage drop, equal to the difference between HVPS input and output voltage. Because a diode can not be switched off, this choice implies that the simulation will only cover the first few microseconds after the breakdown, before the tetrode opens the circuit. In real life the delay between breakdown and intervention of the tetrode lies in the range between 5 µs and 10 µs [18]. For this reason, the duration of the simulation is limited to 4 µs after the breakdown. A simplified approach appears reasonable, when one considers that anticipated voltage peaks of the return conductor immediately after the breakdown constitute the main goal of the exercise. The large complications associated with accurate modelling of the tetrode transient seem not justified.

The simulation starts with no breakdown across the accelerator and initial conditions for all capacitances. The capacitors between high voltage pole of the HVPS and return conductor or ground are charged at a voltage of either 89 kV (if located upstream of the tetrode) or 75 kV (if located downstream of the tetrode). The initial current in the inductors is zero; an initial condition based on the recorded PINI current of 51 A could be used, however the associated stored energy is small as compared the capacitive one. The breakdown occurs at time $t=2$ µs from the start of the simulation, when an ideal switch is closed in parallel to the load. The delay of 2 µs has been chosen to match the pre-trigger time of the experimental waveforms captured by the oscilloscope (table 5.2). A time step of 20 ns has been adopted, corresponding to the sampling period of the oscilloscope.

The circuit parameters used in the simulations are listed in table 5.3 (values of the concentrated components as found in literature), table 5.4 (power supply cable and SF6 transmission line, with ground parameters calculated according to the scheme exposed in §5.1) and table 5.5 (estimated stray inductances and capacitances). The resulting PSIM circuit model is shown in fig. 5.22.

TABLE 5.3 – PARAMETERS OF THE CONCENTRATED COMPONENTS FOR JET BREAKDOWN SIMULATION

Parameter	Value
Output filter of "star point controller" power supply	100 Ω 9.3 µF
Power supply cable matching network	50 Ω 40 nF
Protection cabinet Input snubber	100 Ω 200 µH
Stray capacitance of protection cabinet on load side of the tetrode (In the simulation, 75% to ground, 25% to return conductor)	1 nF
Series resistor	4 Ω
Limiting inductor	100 mΩ 21 mH
Stray capacitance of isolation transformer Resistor connecting deck to ISPS	1.3 nF 10 Ω
Stray capacitance of high voltage deck Figure found in literature Estimate used in simulation	1.5 nF 100 pF
PINI snubber	500 Ω 1.6 mH

TABLE 5.4 – PARAMETERS OF THE DISTRIBUED COMPONENTS FOR JET BREAKDOWN SIMULATION

Parameter	Value
Power supply cable	0.18 µH/m 130 pF/m
Ground parameters of the power supply cable	0.49 µH/m 22 pF/m
Length of cell for the power supply cable	3 m
SF6 transmission line	0.23 µH/m 50 pF/m
Ground parameters of the SF6 transmission line	0.69 µH/m 16 pF/m
Length of cell for the SF6 transmission line	3 m

TABLE 5.5 – ESTIMATED STRAY CAPACITANCES AND INDUCTANCES FOR JET BREAKDOWN SIMULATION

Parameter	*Value*
Stray capacitance of protection cabinet on supply side of the tetrode (In the simulation, 75% to ground, 25% to return conductor)	250 pF
Stay capacitance of return conductor to the physical enclosure of the protection cabinet (C_{PC} in fig. 5.22)	1 nF
Stray capacitance of power supply filter tank	300 pF
Capacitance of main acceleration gap	100 pF
Stray inductance of protection cabinet grounding path (L_{PE} in fig. 5.22)	1 µH
Stray inductance of connection from isolation transformer electrostatic screen to return conductor (L_s in fig. 5.22)	9 µH
Stray inductance of path from structures surrounding high voltage deck to physical ground (L_{HG} in fig. 5.22)	10 µH
Stray inductance of NBI grounding path (L_{GND} in fig. 5.22)	5 µH

Arc inductance

Accelerator capacitance

PINI snubber

SF6 transmission line (90 m)
Each box = 10 cells of 3 m

Deck to ISPS
resistor

Limiting inductor

Series resistor

Tetrode

Input snubber

Cable matching network

Power supply cable (180 m)
Each box = 10 cells of 3 m

Power supply RC filter

Breakdown switch

NBI grounding

L_{GND}

"High voltage deck"
capacitance

L_{HG}

L_S

Isolation transformer
capacitance

Return conductor

C_{PC}

L_{PE}

V_return
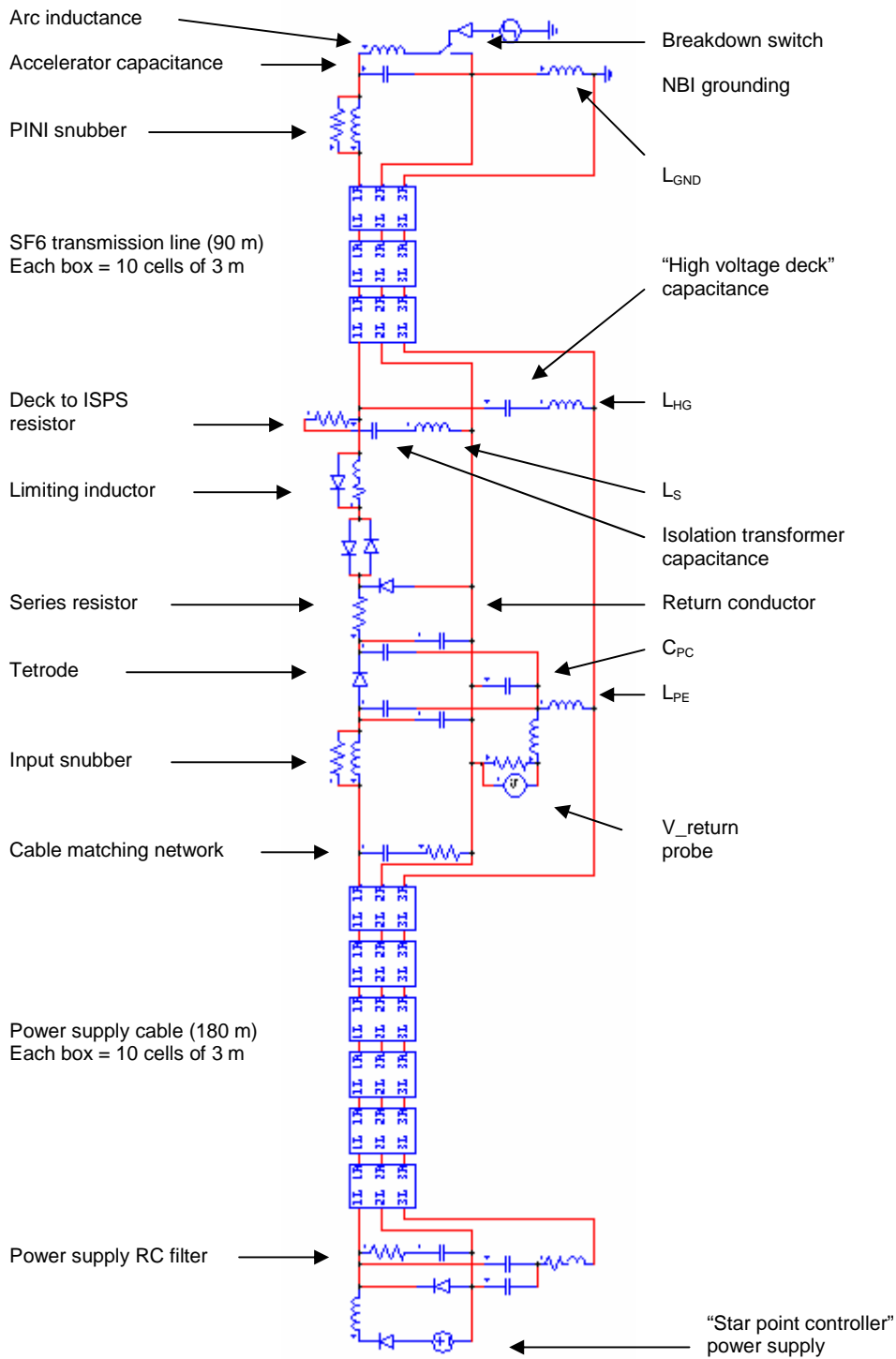probe

"Star point controller"
power supply

FIG 5.22 – PSIM CIRCUIT MODEL FOR JET BREAKDOWN SIMULATION WITH GROUND IMPEDANCE

5.2.4 Simulation with ground impedance and comparison to the experiment

In the previous paragraph the circuit model and parameters have been presented for simulation of a breakdown on JET NBI. A first simulation has been performed using the value of 1.5 nF for the capacitance of the high voltage deck, as reported by Claesen and Mondino [18]. The resulting return conductor voltage at the protection cabinet has the shape shown in fig. 5.23, which differs rather dramatically in peak value from the experimental waveforms shown above.
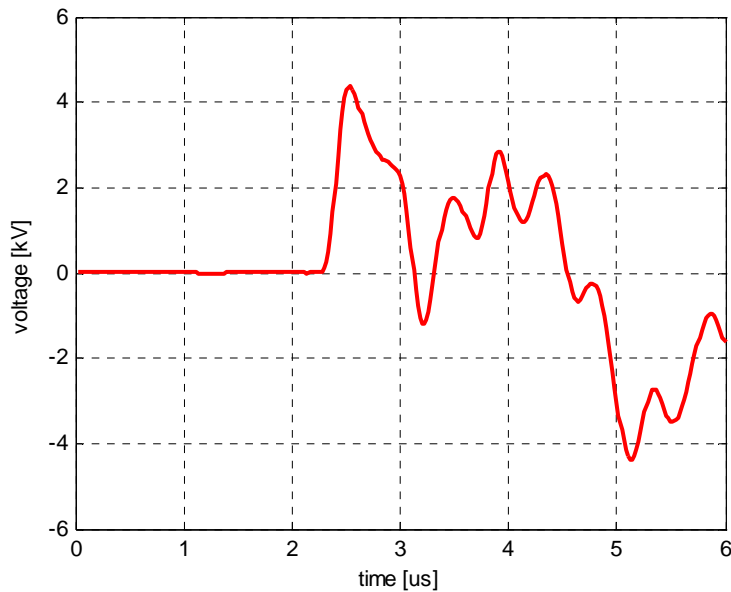
FIG. 5.23 – SIMULATED RETURN CONDUCTOR VOLTAGE IN A BREAKDOWN FOR 1.5 nF DECK CAP. (20 NS TIME STEP)

This discrepancy has led to review critically the simulation and the parameters employed, including the ones found in literature. At a closer look, the value of 1.5 nF for the capacitance of the high voltage deck appears exaggerated. Basile et al. [58] state that "The HV deck is a metallic box of 3.65 x 2.4 x 2 metres, sitting on four porcelain post insulators…". A back of the envelope estimate of the capacitance of the high voltage deck can be carried out considering a parallel plate capacitor of area (3.65 m × 2.4 m) and distance between the electrodes 1.3 m:

$$C_{EST} = \left(8.85 \cdot 10^{-12}\,F/m\right)\frac{3.65m \cdot 2.4m}{1.3m} \cong 60\,pF \qquad\qquad (5.12)$$

The above estimate is much smaller than the figure of Claesen and Mondino, which is dropped from future simulations. A round figure of 100 pF will be used for the high voltage deck capacitance, corresponding to estimate (5.12) with some additional margin.

A breakdown simulation run with the new parameter provides the return conductor voltage of fig. 5.24. Now the agreement with the waveform captured by the oscilloscope appears much improved. The values of the first voltage peaks following the breakdown (+800 V, ±500 V) match well the experimental findings, where on two occasions several peaks were clipped by the 500 V end of scale (see fig. 5.15 and fig. 5.20). A comparison has been performed also in the frequency domain. The Fourier spectrum of the simulated waveform of fig. 5.24 (from which the initial two microseconds before the breakdown have been excluded) is shown in fig. 5.25. This should be compared with fig. 5.21, where the corresponding Fourier spectrum of an experimental waveform is shown (# 70499). Both spectra place most of the harmonic content in the hundreds of kilohertz range, however there are discrepancies on the frequency corresponding to the maximum (253 kHz for the simulated waveform, as opposed to 749 kHz of the experimental one) and on the content at frequencies greater than 1 MHz (virtually absent from the experimental trace).

At this stage some conclusions can be drawn on the elaborated process that was intended to benchmark the ground impedance model with experiment and simulation on JET. An extremely positive result is the capacity to predict with good accuracy the peaks of the return conductor voltage upon a breakdown. From a strict engineering point of view, this is the quantity that matters most, e.g. for the design of the insulation. This success was not obvious, considering the absence in literature of previous measurements or simulations. On the other hand, the frequencies of oscillation are not predicted as accurately and an improvement is necessary in this area. Certainly the practical constraints of the experimental activity on JET played a major role, as mentioned in describing the unfortunate circumstances that frustrated the original schedule of measurements. There are probably three main aspects of the experimental side requiring more attention:

- The case of the high voltage deck capacitance has shown how critical the dependence of the simulation is on some circuit stray parameters. In table 5.5 a number of quantities have been identified that dedicated measurements could estimate with more accuracy

- Digital signals should be added, clearly defining the sequence of the fault (instant of breakdown, instant of tetrode intervention…)

- Enhancement of the instrumentation, in particular of the bandwidth of the voltage transducer. The impact of this aspect can be appreciated in fig. 5.26, showing a simulation of the return conductor voltage run with a time step of 1 ns, similarly to the ITER breakdown simulations. With respect to the 20 ns time step, adopted above to match the oscilloscope sampling frequency, the first peaks have increased by about 50%.
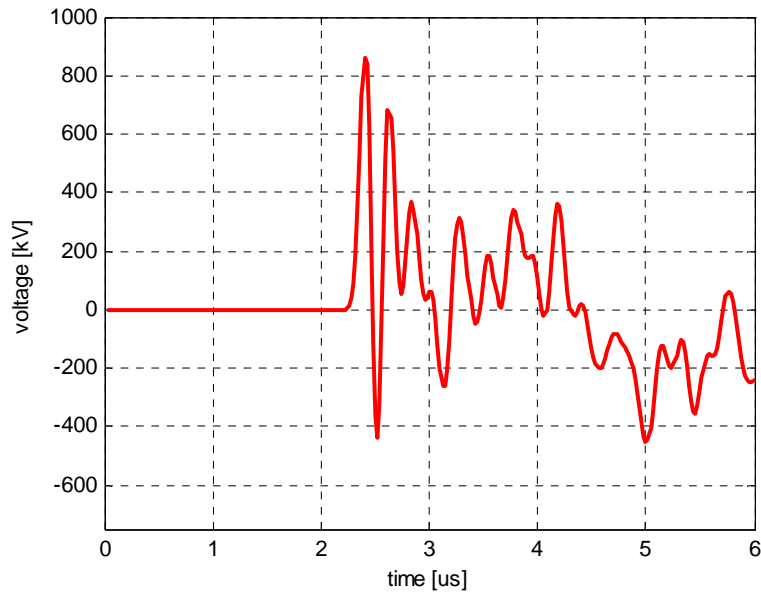

FIG. 5.24 – SIMULATED RETURN CONDUCTOR VOLTAGE IN A BREAKDOWN FOR 100 PF DECK CAP. (20 NS TIME STEP)
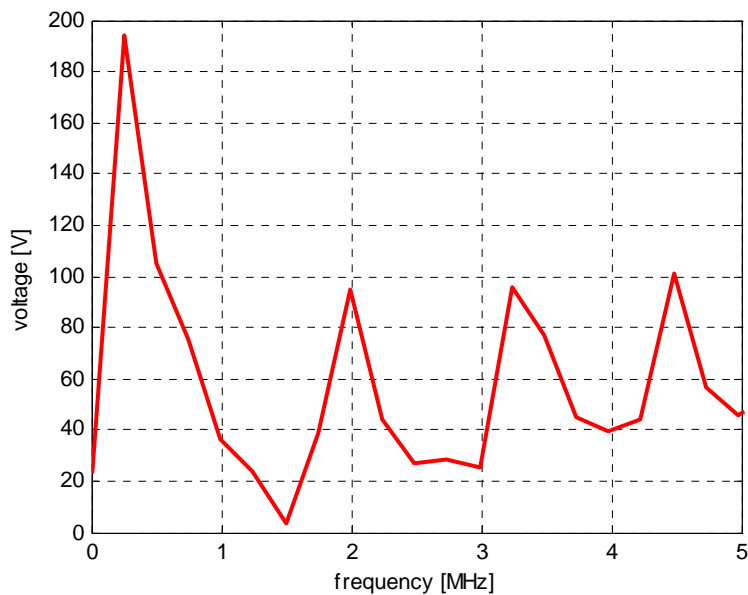

FIG. 5.25 – FFT OF THE SIMULATED RETURN CONDUCTOR VOLTAGE IN A BREAKDOWN (20 NS TIME STEP)
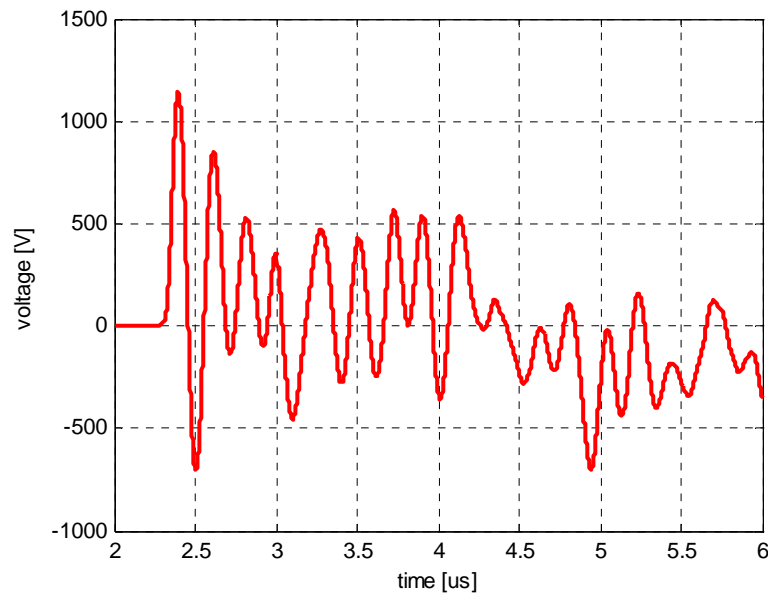
FIG. 5.26 – JET RETURN CONDUCTOR VOLTAGE IN A BREAKDOWN, SIMULATED WITH 1 NS TIME STEP

Altogether, the outcome of the work on JET has increased confidence in the model of transmission line cell with inductive and capacitive couplings to ground (§5.1). In the next section this will be applied to ITER, knowing that the underlying scheme has successfully passed the test of real waveforms and voltages.

5.3 ITER simulation with ground impedance

In the light of the positive performance on JET, the model of the transmission line cell with ground inductance and capacitance (§5.1) has been applied to the ITER breakdown model of chapter 4. The resulting PSIM model is shown in fig. 5.27.

As a first test of the enhanced model against the previous one of fig 4.25, the voltage rise of the return conductor with respect to local ground and upstream of the series resistance has been simulated (fig. 5.28). The comparison with fig. 4.29 shows that the ground model has made a difference: the peak value of the voltage has increased by 31 kV, from 211 kV to 242 kV. One might argue that in percent the gap between the two figures is not dramatic (about 15%), however the implications of the enhanced model go beyond a simulation with specific circuit parameters. There exist a variety of scenarios in the design of the NBI circuit where the new analysis tool could be employed. As an example and further test, let us consider the alternative value of 6.8 Ω proposed by Bigi, Toigo and Zanotto [43] for the series resistance (until this point, in all simulations the reference value of 50 Ω has been used). The effect of this change on the voltage of the return conductor is significant (fig. 5.29), with a new peak value of 91.4 kV. If the same simulation is run on the old circuit model without ground impedance, the resulting peak is 43.4 kV – under the new value of series resistance the difference between the two models is more than 100%! Table 5.6 lists the values found in the various cases. From an engineering prospective, the issue of the voltage rise to local ground during a breakdown is of practical importance, because the design of the insulation of all parts of the circuit connected to the return conductor is based on some prediction of values and waveforms in operation. The potential impact of these simulations can be appreciated considering that the present preliminary design of ITER NBI foresees a peak of the return conductor voltage at the HVPS of 25 kV, for 50 Ω series resistance…

TABLE 5.6 – SUMMARY OF THE RETURN CONDUCTOR PEAK VOLTAGES OBTAINED IN THE VARIOUS SIMULATIONS

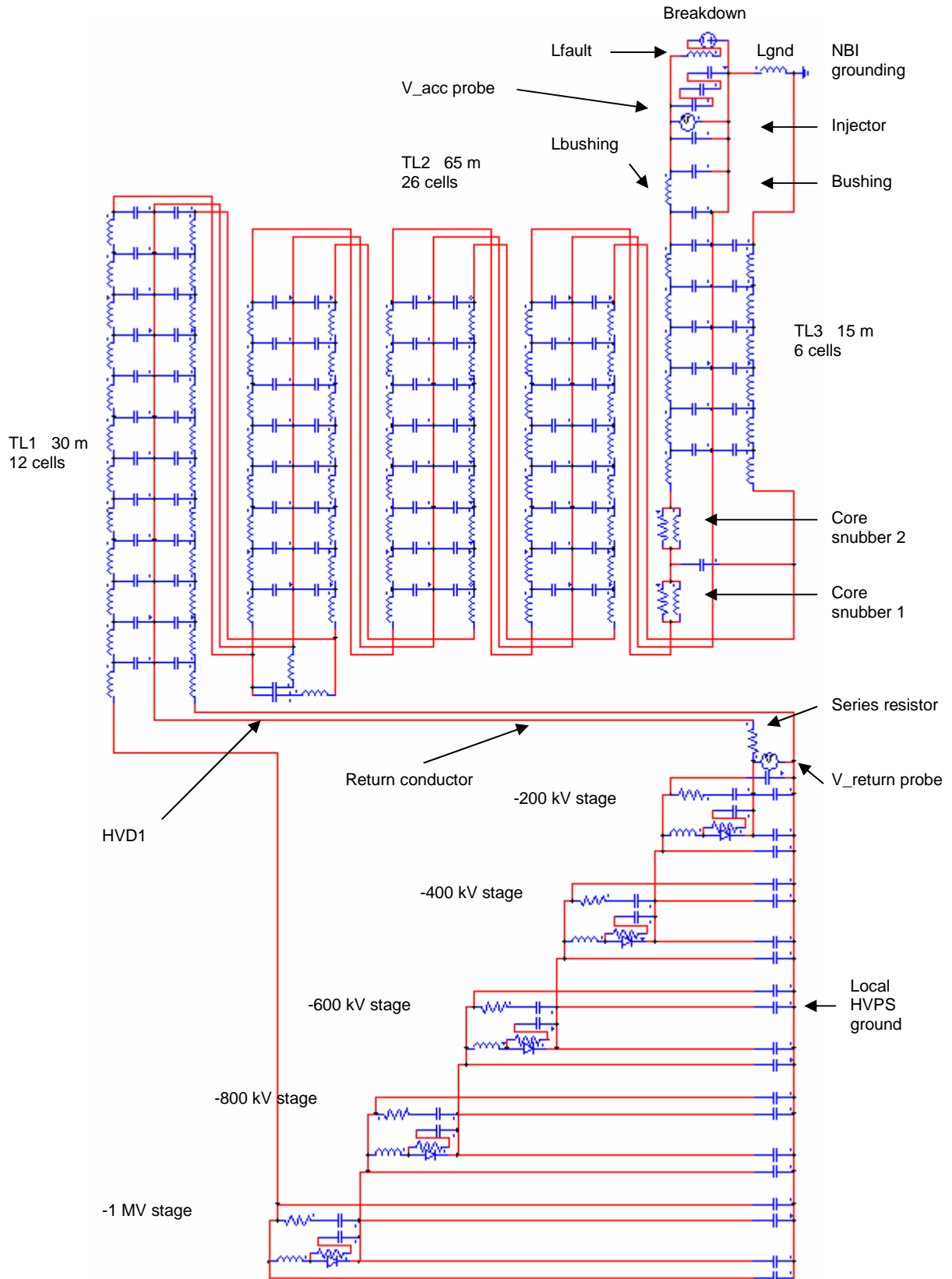|	*50 Ω series resistance*	*6.8 Ω series resistance*
Model without ground impedance (fig. 4.25)	211 kV	43.4 kV
Model with ground impedance (fig. 5.27)	242 kV	91.4 kV

FIG. 5.27 – PSIM MODEL FOR ITER BREAKDOWN SIMULATIONS WITH GROUND IMPEDANCE EFFECTS
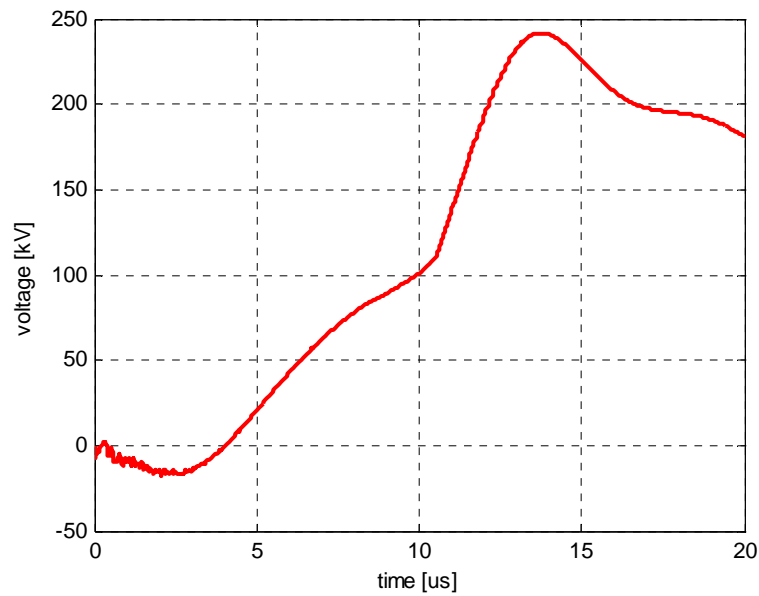
F*IG.* 5.28 – ITER *RETURN CONDUCTOR VOLTAGE TO LOCAL GROUND IN A BREAKDOWN, OBTAINED WITH THE ENHANCED CIRCUIT MODEL AND* 50 Ω *SERIES RESISTANCE*
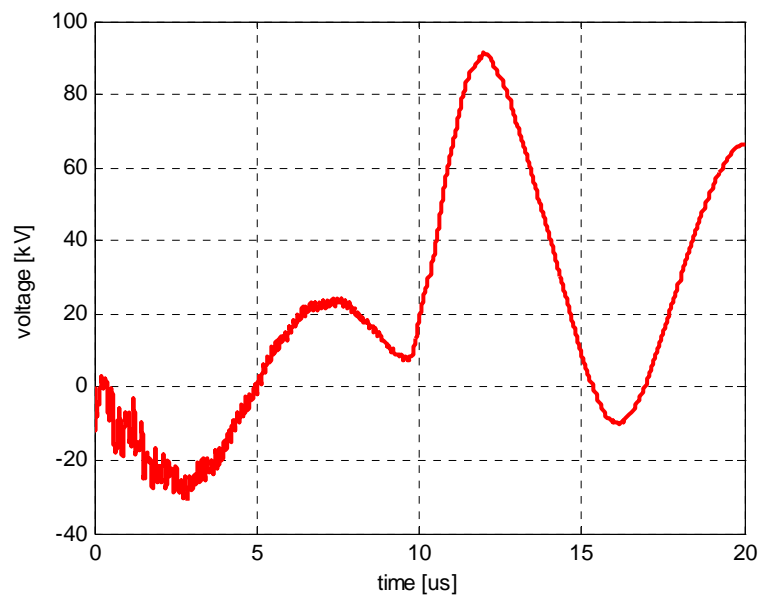

F*IG.* 5.29 – ITER *RETURN CONDUCTOR VOLTAGE TO LOCAL GROUND IN A BREAKDOWN, OBTAINED WITH THE ENHANCED CIRCUIT MODEL AND* 6.8 Ω *SERIES RESISTANCE*
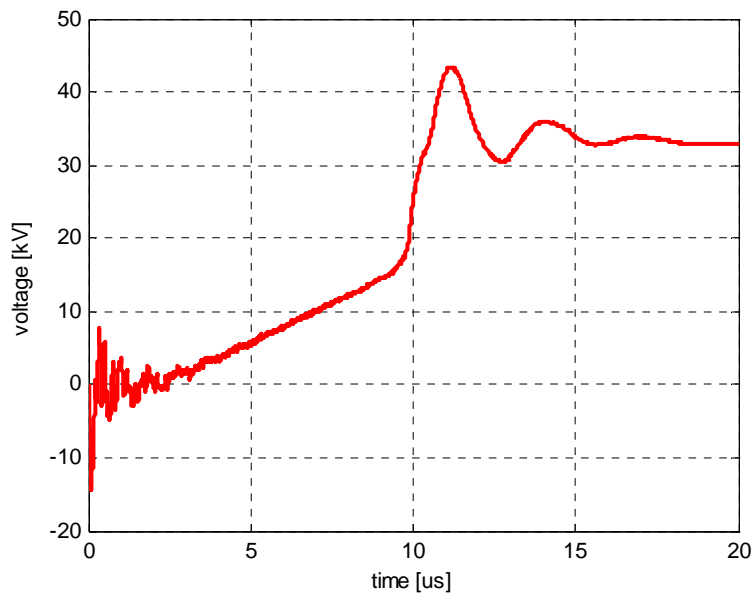
FIG. 5.30 – ITER RETURN CONDUCTOR VOLTAGE TO LOCAL GROUND IN A BREAKDOWN, OBTAINED WITH THE OLD CIRCUIT MODEL AND 6.8 Ω SERIES RESISTANCE

Another noticeable example of how information vital to the design of the individual components can only be obtained from simulations at system level is represented by the case of the voltage across accelerator (and attached bushing) following a breakdown. An issue critical to the performance of dc insulation is the amount of voltage reversal [54] experienced in service. This aspect has an importance even greater for ITER NBI because the breakdown, far from being a once in a lifetime event, will form part of the operational routine. A reliable prediction of the voltage reversal at the breakdown is crucial, e.g. to the design of a challenging component like the –1 MV bushing [36,37].

Employing the circuit model with ground impedance and reference parameters for series resistance (50 Ω) and core snubbers (1000 Ω, 500 μH), the voltage across the accelerator following a breakdown has been simulated (fig. 5.31). From the initial -1 MV, a voltage reversal of almost two thirds results, with a positive peak voltage of 639 kV. Let us consider an alternative set of protection parameters (table 3.6), as proposed by Bigi, Toigo and Zanotto [43]. The accelerator voltage simulation is repeated, with 6.8 Ω series resistance and 100 Ω 140 μH, 100 Ω 95 μH core snubbers.
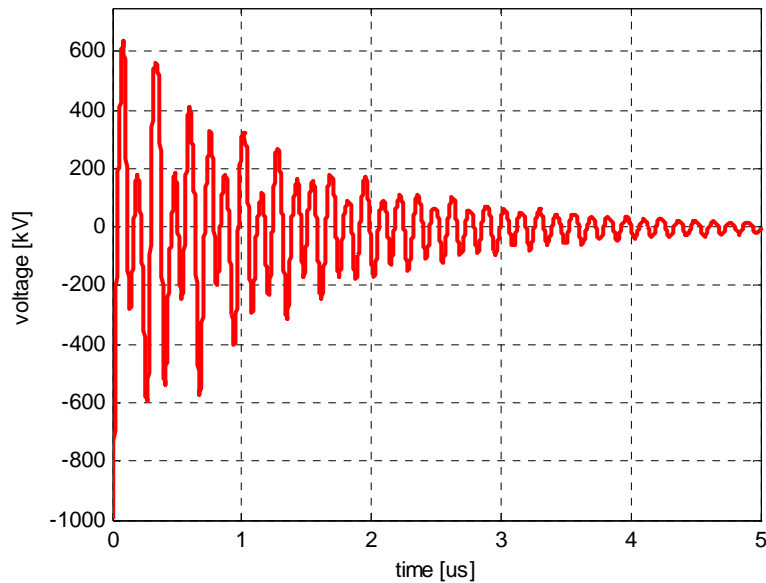
FIG. 5.31 – ITER *ACCELERATOR VOLTAGE IN A BREAKDOWN, OBTAINED WITH THE ENHANCED CIRCUIT MODEL AND REFERENCE PROTECTIONS (50 Ω SERIES RESISTANCE, 1000 Ω 500 μH CORE SNUBBERS*
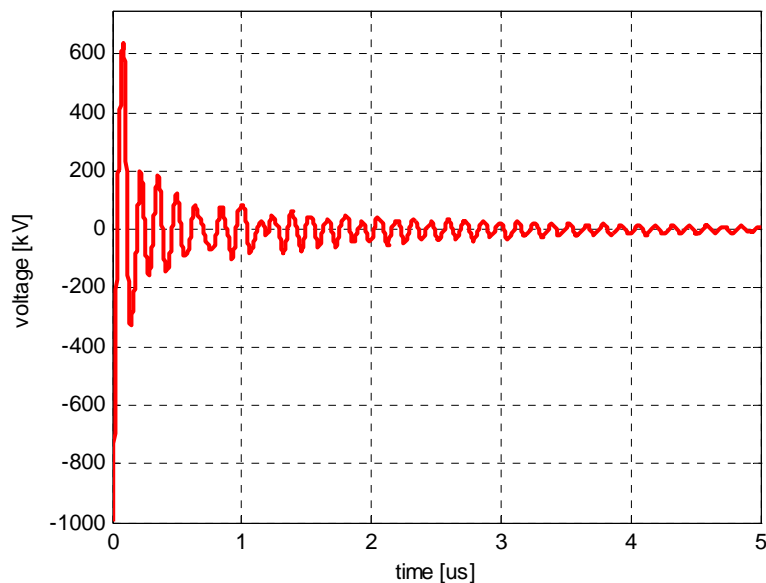

FIG. 5.32 – ITER *ACCELERATOR VOLTAGE IN A BREAKDOWN, OBTAINED WITH THE ENHANCED CIRCUIT MODEL AND ALTERNATIVE PROTECTIONS (6.8 Ω SERIES RESISTANCE, 100 Ω 140 μH, 100 Ω 95 μH CORE SNUBBERS*

The new simulation (fig. 5.32) shows exactly the same voltage inversion (+639 kV) as with the reference protections, however the oscillations of the accelerator voltage decay much faster. Part of the explanation could lie in the inductance of the reference core snubbers, as much as four times greater than the alternative ones. At this point a partial comparison between the two different protection designs can be attempted, based on the simulated waveforms of return conductor voltage and accelerator voltage. Surprisingly, in both respects the scenario with "lighter" protections appears more favourable. Here the core snubber is viewed

simply in terms of circuit parameters; however the underlying device is of complex design and large size [39]. In particular, core snubber length and weight are proportional to the required inductance. Hence the value of a circuit simulation tool for optimising the parameters of core snubbers and other protection devices.

The few sample cases discussed above have tried to give a flavour of the many possible uses of the ITER breakdown model. Refinements will certainly be necessary as the overall design of the system progresses, however the objective of the exercise is to prove the capabilities of the proposed novel approach to modelling of the ground. Also thanks to the validation work carried out on JET, its results appear even more credible than the ones of a more traditional tool.

CONCLUSIONS

In this work circuit analyses for neutral beam systems have been reviewed critically and steps forward proposed, in the direction dictated by the unprecedented requirements of the -1 MV injector for the ITER project.

The weakness has been exposed of the modelling approach found in literature, if applied to the ITER context where propagation of fast phenomena and stray capacitance play an important role. Building on careful consideration of these aspects, newly developed models have been applied to the investigation of two aspects in particular: the ripple of the high voltage power supply for electrostatic acceleration of the ion beam and the transients caused by a breakdown within the injector.

The influence has been shown of transformer capacitance on the Fourier spectrum of the ripple, leading to a distributed circuit model that has enabled the optimisation of the performance of the high voltage power supply. A value in contrast to low voltage converter theory has been proposed for the switching delay among series connected rectifiers bridges, in an area ignored by publications on dc energy transmission.

A first simulation of the breakdown condition on ITER has been developed, paying special attention to distributed modelling of transmission lines and cables and to the assessment of stray capacitance attached to each component of the system. The results thus obtained have shown limits related to modelling of the ground conductor, not treatable as at constant voltage during fast transients. Having identified the need to keep into account capacitive and inductive couplings of the ground with the conductors of the circuit, a novel scheme has been proposed in this respect, under the assumption of perfectly conducting ground.

The new approach has been validated against experimental data before applying it to the ITER breakdown model. The arguments have been presented for adopting as a benchmark the voltage rise of the grounded conductor with respect to local ground, measured during breakdowns at some distance from the single grounding point of the circuit. The collection of data on the JET tokamak was successful, although complicated by faults of the plant. The development of a breakdown simulation for JET has then been described, including capacitive and inductive couplings of the ground conductor. The last step of the validation has been a comparison of simulated waveforms for the voltage rise of the grounded conductor against the traces captured with the oscilloscope. This process, also implying a critical review of JET circuit parameters found in literature, has given positive results for the prediction of the peak values. The agreement, though still reasonable, is not as good in terms of Fourier spectra. The circuit model has proven sensible to the values of few stray circuit parameters difficult to assess, like for instance the inductance to be associated to grounding paths. To improve further the JET circuit model, more experimental work is probably necessary, with a systematic check of the circuit parameters quoted in literature.

The modelling technique for ground inductive and capacitive couplings, successfully tested on JET, has been extended to ITER leading to a new breakdown circuit model. Simulations have been illustrated of the grounded conductor voltage rise during breakdowns, reaching peaks as high as 240 kV. The contrast is sharp with figures of few tens of kilovolts quoted in ITER preliminary design documents. The value of the ground circuit model has been shown by comparing its results with those obtained under the traditional assumption of ground at constant voltage throughout the circuit. The potential of the newly developed tool in assessing different schemes for protection of the injector has also been demonstrated.

The extension of the circuit model to a multiple gap configuration of the ITER accelerator represents a natural prosecution of this work. The availability of reliable simulations will be crucial to the refinement of the design of ITER neutral beam injector, in particular to the definition of suitable passive protection components and to the prediction of transient voltage waveforms the insulation will experience in operation.

REFERENCE

1. Wesson J., **Tokamaks**, Clarendon Press, 2004
2. Ongena J. and Van Oost G., "Energy for future centuries", *Transactions for fusion science and technology*, Vol. 49, no. 2T, 2006.
3. Noterdaeme J.M., "Controlled fusion, from basic plasma physics to nuclear engineering", *12th International Conference on Emerging Nuclear Energy Systems*, Brussels, Belgium, 21-26 August 2005.
4. Faulconer D.W., "Current drive", *Transactions for fusion science and technology*, Vol. 49, no. 2T, 2006.
5. Rebut P.H., Keen B.E., "The JET experiment: evolution, present status and prospects", *Fusion technology*, Vol. 11, no. 1, 1987, pp. 13-42.
6. Jacquinot, J. and the JET team, "Deuterium-tritium operation in magnetic confinement experiments: results and underlying physics", *Plasma Physics and Controlled Fusion*, Vol. 41, no. 3A, 1999.
7. Holtkamp N. and the ITER project team, "An overview of the ITER project", *Fusion Engineering and Design*, Vol. 82, no. 5-14, 2007, pp. 427-434.
8. www.iter.org
9. Koch R., "Plasma heating by neutral beam injection", *Transactions for fusion science and technology*, Vol. 49, no. 2T, 2006, pp. 167-176.
10. Kraus W. et al., "Large-area radio frequency plasma sources for fusion applications", *Review of Scientific Instruments*, Vol. 69, no. 2, 1998, pp. 956-958.
11. Goede A.P.H., Green T.S., "Operation limits of multiple ion sources", *Physics of Fluids*, Vol. 25, no. 10, 1982, pp. 1797-1810.
12. Roth J.R., **Industrial plasma engineering vol.1**, Institute of Physics Publishing, 1995.
13. Vollmer O. et al., "Commissioning and performance of the new ASDEX Upgrade neutral beam injector", Proceedings of the 20th Symposium on Fusion Technology, Marseille, France, 7-11 September 1998, Vol. 1, pp. 449-452.
14. Duesing G. et al., "JET additional heating systems – Neutral beam injection system", *Fusion technology*, vol. 11, no. 1, 1987, pp. 163-202.
15. Kuriyama M. et al., "Operation and development of the 500-keV negative-ion-based Neutral Beam Injection system for JT-60U", *Fusion Science and Technology*, Vol. 42, no. 2-3, 2002, pp. 410-423.
16. Coupland J.R., Green T.S., Hammond D.P., Riviere A.C., "A study of the ion beam intensity and divergence obtained from a single aperture three electrode extraction system", *Review of Scientific Instruments*, Vol. 44, no. 9, 1973, pp. 1258-1270.
17. Fink J.H., Baker W.R., Owren H.M., "Analysis and application of a transformer core that acts as an arc snubber", *IEEE Transactions on Plasma Science*, Vol. PS-8, no. 1, 1980, pp. 33-38.
18. Claesen R., Mondino P.L., "JET additional heating systems – Neutral beam injection and radio-frequency power supplies", *Fusion technology*, vol. 11, no. 1, 1987, pp. 141-162.
19. Owren H.M., Baker W.R., Berkner K.H., Hopkins D.B., Massoletti D.J., "The effect of capacitive stored energy on neutral beam accelerator performance", Proceedings of the 12th Symposium on Fusion Technology, Jűlich, Germany, 13-17 September 1982, Vol. 1, pp. 455-460.
20. Hrabal D., Kunze R.C., Weigland W., "HV power supply for neutral injection experiments Wendelstein VII and ASDEX", Proceedings of the 8th Symposium on engineering problems of fusion research, San Francisco, USA, 13-16 November 1979, Vol. 2, pp. 1005-1009.
21. Mizuno M. et al., "Inverter type high voltage dc power supply for negative-ion-based neutral beam injectors", Proceedings of the 13th Symposium on Fusion Engineering, Knoxville, USA, 2-6 October 1989, Vol. 1, pp. 284-287.
22. Jensen F., Claesen R., McBryan H., Mills J., Ŏstrŏm R., Vadgama A.P., "Upgrading of the neutral beam power supplies from 80kV/60A to 140kV/60A", Proceedings of the 19th Symposium on Fusion Technology, Lisbon, Portugal, 16-20 September 1996, Vol. 1, pp. 665-668.
23. Ganuza D. et al., "130 kV 130 A High voltage switching mode power supply for neutral beam plasma heating: design issues", *Fusion Engineering and Design*, Vol. 66-68, 2003, pp. 615-620.
24. ITER physics basis editors et al., "Chapter 1: overview and summary", *Nuclear Fusion*, Vol. 39, no. 12, 1999, pp. 2137-2174.
25. Inoue T. et al., "Design of neutral beam system for ITER-FEAT", *Fusion Engineering and Design*, Vol. 56-57, 2001, pp. 517-521.
26. de Esch H.P.L., Hemsworth R.S., Massmann P., "SINGAP: the European concept for negative ion acceleration in the ITER neutral injectors", *Review of Scientific Instruments*, Vol. 73, no. 2, pp. 1045-1047.
27. Watanabe K. et al., "Development of a dc 1 MV power supply technology for NB injectors", *Nuclear Fusion*, Vol. 46, no. 6, 2006, pp. S332-S339.

28. Nabae A., Takahashi I., Hirofumi A., "A new neutral-point-clamped PWM inverter", *IEEE Transactions on Industry Applications*, Vol. 1A-17, no. 5, 1981, pp. 518-523.

29. Åström U., Westman B., Lescale V., Asplund G., "Power transmission with HVDC at voltages above 600kV", Proceedings of the IEEE PES conference, Durban, South Africa, 11-15 July 2005, pp. 44-50.

30. Perrier C., Beroual A., Bessede J.-L., "Improvement of power transformers by using mixtures of mineral oil with synthetic esters", *IEEE Transactions on Dielectrics and Electric Insulation*, Vol. 13, no. 5, 2006, pp. 556-564.

31. Greenwood A, **Electrical transients in power systems**, Second edition, John Wiley & Sons, 1991.

32. Rizk F.A.M., Kamel S.I., "Modelling of HVDC wall bushing flashover in nonuniform rain", *IEEE Transactions on Power Delivery*, Vol. 6, no. 4, 1991, pp. 1650-1662.

33. Gaio E., Toigo V., De Lorenzi A., Piovan R., Zanotto L., "The alternative design concept for the ion source power supply of the ITER neutral beam injector", *Fusion Engineering and Design*, Vol. 83, no. 1, 2008, pp. 21-29.

34. Gaio E. et al., "Studies on the radio frequency power supply system for the ITER NB injector ion source", *Fusion Engineering and Design*, Vol. 82, no. 5-14, 2007, pp. 912-919.

35. De Lorenzi A et al., "The insulation structure of the 1 MV transmission line for the ITER neutral beam injector", *Fusion Engineering and Design*, Vol. 82, 2007, pp. 836-844.

36. Masiello A., "Adaptation of the 1MV bushing to the SINGAP concept for the ITET NB injector test bed", *Nuclear Fusion*, Vol. 46, no. 6, 2006, pp. S340-S351.

37. Inoue T. et al., "Development of beam source and bushing for ITER NB system", *Fusion Engineering and Design*, Vol. 82, no. 5-14, 2007, pp. 813-818.

38. Antoni V, "The ITER neutral beam system: status of the project and review of the main technological issues", Invited presentation at the 24th Symposium on Fusion Technology, Warsaw, Poland, 11-15 September 2006.

39. Watanabe K., Mizuno M., Nakajima S., Iimura T., "Development of a high performance core snubber for high power neutral beam injectors", *Review of Scientific Instruments*, Vol. 69, no. 12, 1998, pp. 4136.

40. http://www.matweb.com

41. Edwards D.C., Bigi M., Brown D.P.D., Ganuza D., Garcia F., Hudson Z. et al., "Commissioning and operation of 130kV/130A switched-mode HV power supplies with the upgraded JET neutral beam injectors", *Fusion Engineering and Design*, Vol. 75, no. 75-79, 2005, pp. 41-47.

42. Watanabe K, Ohara Y., Okumura Y., Ono Y., Tanaka M., Kawashima S. et al., "Design of NBI power supplies", JAERI final report of ITER task N42TD02FJ, 1997.

43. Bigi M., Toigo V., Zanotto L., "Protections against grid breakdowns in the ITER neutral beam injector power supplies", *Fusion Engineering and Design*, Vol. 82, no. 5-14, 2007, pp. 905-911.

44. Eckard R.D., Van Ness H.W., "The sustaining neutral beam power supply system for the mirror fusion test facility", Proceedings of the 8th Symposium on engineering problems of fusion research, San Francisco, USA, 13-16 November 1979, Vol. 1, pp. 337-340.

45. Ficklin B.P., Tallmadge G.E., Williams M.F, "Computer modeling with ASTAP of the sustaining neutral-beam power supply system of the MFTF", Proceedings of the 8th Symposium on engineering problems of fusion research, San Francisco, USA, 13-16 November 1979, Vol. 1, pp. 341-346.

46. Mihalka A.M., "A digital simulation of the MFTF power supply system using EMTP", Proceedings of the 8th Symposium on engineering problems of fusion research, San Francisco, USA, 13-16 November 1979, Vol. 1, pp. 347-351.

47. D'Amore M., Sarto M.S., "Simulation models of a dissipative transmission line above a lossy ground for a wide-frequency range – Part I: single conductor configuration", *IEEE Transactions on Electromagnetic Compatibility*, Vol. 38, no. 2, pp. 127-138.

48. Ganuza D., Garcia F., Zulaika M., Perez A., Jones T.T.C., "130kV 130A high voltage switching mode power supply for neutral beam injectors-Control issues and algorithms", *Fusion Engineering and Design*, Vol. 75, no. 75-79, 2005, pp. 253-258.

49. Mohan N., Undeland T.M., Robbins W.P., **Power electronics – Converters, applications and design**, 2nd edition, John Wiley & Sons, 1995.

50. Larsen E.V., Sublich M., Kapoor S.C., "Impact of stray capacitance on HVDC harmonics", *IEEE Transactions on Power Delivery*, Vol. 4, no. 1, 1989, pp. 637-645.

51. Rittiger J, Kulickle B., "Calculation of HVDC-converter harmonics in frequency domain with regard to asymmetries and comparison with time domain simulations", *IEEE Transactions on Power Delivery*, Vol. 10, no. 4, 1995, pp. 1944-1949.

52. Perkins B.K., Iravani M.R., "Novel calculation of HVDC converter harmonics by linearization in the time domain", *IEEE Transactions on Power Delivery*, Vol. 10, no. 2, 1997, pp. 867-873.

53. Riedel P., "Harmonic voltage and current transfer, and AC- and DC-side impedances of HVDC converters", *IEEE Transactions on Power Delivery*, Vol. 30, no. 3, 2005, pp. 2095-2099.
54. Montanari G.C., Mazzanti G., Simoni L., "Progress in electrothermal life modeling of electrical insulation during the last decades", *IEEE Transactions on Dielectrics and Electrical Insulation*, Vol. 9, no. 5, 2002, pp. 730-745.
55. http://www.powersimtech.com
56. Righetto L., "Integration of the 1MV bushing in the alternative design for ITER neutral beam injector", M.Sc. thesis, Department of electrical engineering of the University of Padua, 2005.
57. Aslin H. et al., "The power supply and protection system for the extraction grid of the JET neutral injectors", Proceedings of the 12th Symposium on Fusion Technology, Jűlich, Germany, 13-17 September 1982, Vol. 1, pp. 391-397.
58. Basile G.L., Ciscato D., Dobbing J.A., Mondino P.L., "The neutral injector auxiliary power supply system in JET: design, manufacture and tests", Proceedings of the 13th Symposium on Fusion Technology, Varese, Italy, 24-28 September 1984, Vol. 2, pp. 835-842.
59. http://www.tek.com
60. http://www.yokogawa.com

ACKNOWLEDGMENTS